UNIVERSITY OF HELSINKI REPORT SERIES IN ASTRONOMY

No. 19

Stellar Magnetism in Theory and Observation

Elizabeth Melanie Cole

ACADEMIC DISSERTATION

Department of Physics
Faculty of Science
University of Helsinki
Helsinki, Finland

To be presented, with the permission of the Faculty of Science of the University of Helsinki, for public criticism in auditorium E204 at Physicum on Kumpula campus (Gustaf Hällströmin katu 2) on January 5th, 2017 at 12 o'clock noon.

Helsinki 2016

Supervisors: Docent Thomas Hackman
Department of Physics
University of Helsinki

Docent Maarit J. Käpylä
Department of Information and Computer Science
Aalto University

Docent Petri J. Käpylä
Department of Information and Computer Science
Aalto University

Pre-examiners: Prof. Ansgar Reiners
Institut für Astrophysik
Georg-August Universität

Prof. Michel Rieutord
Institut de Recherche en Astrophysique et Planétologie
Observatoire Midi-Pyrénées

Opponent: Prof. Sydney Barnes
Leibniz-Institut für Astrophysik Potsdam (AIP)

Custos: Prof. Karri Muinonen
Department of Physics
University of Helsinki

Cover picture: Mollweide projection of the azimuthal magnetic field near the surface of a numerical simulation in spherical coordinates using the Pencil Code.

ISSN 1799-3024 (print version)
ISBN 978-951-51-2762-4 (print version)
Helsinki 2016
Helsinki University Print (Unigrafia)

ISSN 1799-3032 (pdf version)
ISBN 978-951-51-2763-1 (pdf version)
ISSN-L 1799-3024
http://ethesis.helsinki.fi/
Helsinki 2016
Electronic Publications @ University of Helsinki
(Helsingin yliopiston verkkojulkaisut)

Elizabeth Melanie Cole: **Stellar Magnetism in Theory and Observation**, University of Helsinki, 2016, 113 p. + appendices, University of Helsinki Report Series in Astronomy, No. 19, ISSN 1799-3024 (print version), ISBN 978-951-51-2762-4 (print version), ISSN 1799-3032 (pdf version), ISBN 978-951-51-2763-1 (pdf version), ISSN-L 1799-3024

Keywords: stellar activity, star spots, direct numerical simulations, time series analysis, inverse methods, mean-field theory, dynamo theory

Abstract

The universe is populated with magnetically active stars. This magnetic activity is thought to be generated by dynamos operating in turbulent stellar convection zones, a process by which kinetic energy is converted into magnetic energy. The solar dynamo is but one dynamo type possible for stars. Rapidly rotating late-type stars are observed to have large spots, activity cycles, flip-flops, and active longitudes, all indicating a different dynamo mechanism may be responsible. Numerical simulations provide a tool for better understanding some of the mechanisms responsible for these dynamos.

In this thesis, direct numerical simulations in spherical wedges are used to study dynamo mechanisms in the stellar convection zone. These spherical wedges are used to investigate the dependence of the resulting magnetic field on input parameters such as the density stratification and rotation rate. Mean-field models are used to evaluate the assumption that the wedges can be used to approximate full spheres.

As rotation increases, differential rotation decreases in the models, in agreement with observations where more rapidly rotating stars have smaller estimates for differential rotation. As density stratification approaches more realistic values, a latitudinal dynamo wave with equatorward propagation is found. The impact of the domain size in the azimuthal direction on the results is explored. When the domain size is increased to 2π in the azimuthal direction, a non-axisymmetric $m = 1$ mode is excited. This non-axisymmetry is reminiscent of the field configurations of rapidly rotating late-type stars. The azimuthal dynamo wave rotates nearly independently of latitude and depth, and its rotation rate is slower than that of the mean rotation of the model. This azimuthal dynamo can provide a possible explanation for the observed rotational difference of spots from the mean rotation observed on stars.

The wedges use the perfect conductor boundary conditions at the latitudinal boundary to compensate for the omission of polar regions due to the time step becoming prohibitively small there. Simple mean-field models with only a latitudinal

extent and perfectly conducting boundaries do not oscillate when the model is extended to the poles. Thus oscillations near the polar region may be an artifact of the boundary condition. However, when the α effect from mean-field dynamo theory and magnetic diffusivity are concentrated towards lower latitudes, oscillatory solutions with equatorward migration are found. When sufficient shear is added, oscillatory solutions are again found, and the Parker-Yoshimura rule for latitudinal dynamo wave propagation is obeyed. It is concluded that numerical simulations where the α effect and diffusivity are found to be stronger at lower latitudes and simulations with sufficient shear are considered good approximations of full spheres.

These numerical simulations are put into context with stellar observations. Two young solar analogs are selected, V352 Canis Majoris and LQ Hydrae. V352 CMa is considered an active star, while LQ Hya is classified as a super-active star. The continuous period search method is applied to the low-amplitude light curves of V352 CMa. Stable active longitudes with rotation periods of 7.157 days are found. This is faster than the mean rotation of 7.24 days. Such active longitudes may be due to the underlying magnetic structure with azimuthal dynamo waves competing with differential rotation.

LQ Hya rotates even more rapidly with a rotation period of only 1.600 days. A carrier period is selected of 1.605 days using the D^2 statistical analysis. Primary and secondary light curve minima are found with the carrier fit analysis. No stable active longitudes are found, instead, there is only a short period spanning a few years where an active longitude may exist, but the rotation period is poorly defined. Several possible flip-flop events are identified. The azimuthal dynamo waves in numerical simulations with comparable rotation rates have a similar chaotic nature.

The Doppler Imaging technique is applied to LQ Hya to examine the latitudinal spot structure. Spots at high and low latitudes are in agreement with the bimodal structure of the D^2 statistic used in the carrier fit analysis. Temperature maps of LQ Hya spanning four years show an increase and a decrease in spot coverage, but no cycle can be found. Because LQ Hya is a rapidly rotating star, differential rotation is estimated to be very small. The azimuthal dynamo wave presents a new possible explanation for the jumps and trends of the spots in observations of this star.

Acknowledgements

First and foremost, I thank my trio of exemplary advisors, Petri Käpylä, Maarit Käpylä, and Thomas Hackman, because this thesis would not be possible without them. I was first introduced to MHD by Maarit, moving from the interstellar medium to stars themselves. Petri was my instructor in the Pencil Code, showing me the ropes of creating a numerical convection zone. Thomas helped with observational insight, giving me the chance to make maps of stellar surfaces, something quite incredible to think about. This team of advisors helped me learn about the connections between observational astronomy and theoretical astrophysics and were tireless advocates for helping me find funding and resources for finishing this work.

I thank the Nordic Institute for Theoretical Physics (Nordita), which kindly hosted me once in April 2013 and again in October 2013 where I had the pleasure of collaborating with Axel Brandenburg on a project using the Pencil Code. Sweden became a second home, and it truly was a pleasure to live in Stockholm for a few months. I also thank the Väisälä Foundation, without which this work would not have been possible. I am also grateful to the pre-examiners for their insightful comments and constructive criticism to help improve this thesis.

I would like to thank my Finnish family, the Munnes, who have always been there when I needed a break and some Finnish wisdom and cooking. I'd like to thank the Schoeman and Brandão families for helping me get through the dark winter months. Good food, great friends, singing, and the laughter of children are the best medicine for stress. I would also like to thank all my colleagues and friends. I cannot name them all here, but they know who they are, and I hope they had their fill of cake. I am also thankful to my friends in the USA who found time in their busy schedules to see me those rare times I managed to visit, and those who came out to visit me in this wonderful country.

I also owe a debt to my own parents, John and Karen Cole, for indulging my crazy plan to move to Finland and study astrophysics. I am thankful for every care package sent, every Skype message answered no matter the hour. My sister Patricia has my gratitude for every gadget and puzzle she sent, and my sister Laura has my gratitude for all her help with proofreading and answering my odd grammar questions.

And finally, I would like to thank my fiancé Tim for continuing to provide support, encouragement, and love even when we were oceans apart. Our adventures together always made up for it. It is my turn now to provide the encouragement, support, and chocolate cake as he works hard to finish his own thesis.

List of publications

Paper I: Käpylä, P. J., Käpylä, M. J., **Cole, E.**, Warnecke, J., and Brandenburg, A., 2013, "Effects of Enhanced Stratifcation on Equatorward Dynamo Wave Propagation." The Astrophysical Journal, 778, 41

Paper II: Cole, E., Käpylä, P. J., Käpylä, M. J., and Brandenburg, A., 2014, "An Azimuthal Dynamo Wave in Spherical Shell Convection." The Astrophysical Journal Letters, 780, L22

Paper III: Cole, E., Brandenburg, A., Käpylä, P. J., and Käpylä, M. J., 2016, "Robustness of oscillatory α^2 dynamos in spherical wedges." Astronomy & Astrophysics, 593, A134

Paper IV: Kajatkari, P., Jetsu, L., **Cole, E.**, Hackman, T., Henry, G. W., Joutsiniemi, S.L., Lehtinen, J., Mäkelä, V., Porceddu, S., Ryynänen, K., and Şolea, V., 2015, "Periodicity in some light curves of the solar analogue V352 Canis Majoris." Astronomy & Astrophysics, 577, A84

Paper V: Olspert, N., Käpylä, M. J., Pelt, J., **Cole, E. M.**, Hackman, T., Lehtinen, J., and Henry, G. W., 2015, "Multiperiodicity, modulations, and flip-flops in variable star light curves. III. Carrier fit analysis of LQ Hydrae photometry for 1982-2014." Astronomy & Astrophysics, 577, A120

Paper VI: Cole, E. M., Hackman, T., Käpylä, M. J., Ilyin, I., Kochukhov, O., and Piskunov, N., 2015, "Doppler imaging of LQ Hydrae for 1998-2002." Astronomy & Astrophysics, 581, A69

List of Abbreviations

CF	Carrier Fit
CPS	Continuous Period Search
DI	Doppler Imaging
DNS	Direct Numerical Simulation
EMF	Electromotive Force
LES	Large Eddy Simulation
MHD	Magnetohydrodynamics
ZDI	Zeeman Doppler Imaging

Contents

1 Introduction

The Sun is the best studied star in the universe and yet there is still much to learn about the star which is the basis of human life. Its proximity and importance make it an object of great interest to humanity. Modern observation techniques have advanced over the centuries from naked-eye observations of the larger sunspots, to methods of projecting the solar disk to observe the surface, to using techniques to probe the interior through helioseismology and making direct observations from space-based observatories. However, the Sun itself is billions of years old, granting humanity only the briefest of glimpses as to how the Sun evolves over time.

The Sun is magnetically active, with a field thought to be generated in the convection zone and extending out through the corona and beyond to Earth, where it interacts with the terrestrial magnetic field to create auroras and magnetic storms, among other phenomena. The solar cycle is fascinatingly complex, but certain trends are observable and predictability of the solar magnetic cycle is an important goal towards protecting space-based instrumentation and Earth-bound power grids from disturbances caused by magnetic activity. There is approximately an 11-year cycle of solar activity during which magnetic activity increases and decreases, at each polarity, making a total approximate 22-year cycle for the Sun to return to the same polarity. At the beginning of the 11-year cycle, spots tend form at higher latitudes and as the cycle progresses, spot activity moves towards the equator. This is evidence of an underlying mechanism that continually generates a magnetic field. One such mechanism of maintaining or amplifying a magnetic field is called the dynamo, by which kinetic energy is converted into magnetic energy. The Sun can be considered to be a rotating sphere containing electrically conductive fluid, a strong toroidal magnetic field, and a weaker poloidal field. The poloidal field is converted into a toroidal field as differential rotation winds up the magnetic field lines in the azimuthal direction. Mean-field theory closes the cycle by proposing smaller-scale helical fluctuations, quantified by the α tensor in the electromotive force, that can in turn regenerate the poloidal field via the α effect.

Numerical simulations present a way of testing dynamo theory, mean-field theory

and exploring possible mechanisms to explain observed phenomena. While dynamos can be created and observed in a laboratory, these experiments have limited length and time scales that cause very different behavior than that present in the solar convection zone. Although full modeling with the parameters of the Sun and details to the level of observations is still beyond modern computational limits, numerical simulations can provide invaluable insight into details of the dynamo processes. The convection zone, with differential rotation and turbulence, is of particular interest to investigate via numerical simulations to find specific regimes where dynamos exhibit solar-like behavior, such as cycles on the order of decades and equatorward propagation of the magnetic field. It is also worth investigating assumptions about the models used for numerical simulations, as there exists computational limitations of resolution and input parameters. Often, numerical simulations must use special techniques to circumvent these limitations, such as limiting a latitudinal extent of a spherical model to avoid singularities at the pole, and the effect of these choices must be examined to determine the impact such changes have on the final results.

In addition to computer simulations, the universe itself offers a rich laboratory of sample stars similar to the Sun but at varying ages, thus allowing observations of the possible past and future of the Sun. Of particular interest to this thesis are magnetically active stars, specifically focusing on the long term cycles and spot structures (and therefore possible underlying magnetic fields) of two young solar analogs. By observing the light curve photometry, statistical methods such as the Continuous Period Search method and the Carrier Fit method can be used to analyze both short and long term cycle periods, as well as the fluctuations and changes of rotation and cycle periods. Inverse methods such as Doppler Imaging use spectroscopy to create temperature maps of stellar surfaces, providing information about spot latitudes, longitudes, and the temperature deviations from the average temperature. The activity of the selected young solar analogs suggests that the Sun itself was once far more active than observed today.

This thesis combines both theory and observation. Certain predicted phenomena of dynamo theory and mean-field theory are explored through numerical simulations, with promising results that have a strong toroidal field with equatorward drift, similar to that of the Sun's magnetic field. By relaxing the wedge assumption in the azimuthal direction and extending parameters to rapidly rotating stars, an azimuthal dynamo wave predicted by mean-field theory is observed. While this stands alone as an interesting result, if combined with observations the azimuthal dynamo wave provides alternative mechanisms to explain certain aspects of observed behavior of stellar objects, such as the drift of preferred longitudes of spot formation with respect to the rotation period.

2 Magnetically Active Stars

Of all the magnetically active stars in the universe, the Sun, as the closest star, was the first to be observed to have a magnetic field. As observing techniques progressed, magnetic fields were also detected in stars, galaxies, and other astronomical objects. These magnetic fields behave very differently in many respects from the solar magnetic field, but some basic underlying principles are thought to be shared, including the mechanism that theoretically regenerates and amplifies the observed magnetic fields in stars.

2.1 Solar Activity

The Sun is located approximately $149 \cdot 10^6$ km away, making some details of the solar surface discernible with the human eye. Advanced techniques such as helioseismology, solar neutrino measurements, and observed elemental abundances combined with theoretical models are used to probe the interior of the Sun, and improved terrestrial and space-based observatories continually monitor the Sun in greater detail. Certain phenomena such as sunspots and solar storms have been used to understand the activity cycle of the Sun and the underlying mechanisms.

Sunspots, or cooler regions on the solar surface that appear darker than the surrounding plasma, have been observed as early as 364 BCE by Chinese astronomer Shi Shen (Vaquero and Vázquez, 2009). Beginning in 1610, Galileo Galilei started making regular observations of spots on the solar surface (Galilei, 1613). His student Benedetto Castelli developed a method of using a telescope to project the solar disk, allowing Galileo to sketch sunspots in detail over time. Certain observations were made as a result of this time series of observations: the spots took approximately 11 days to cross the solar disk, the spots appeared and disappeared in clusters, and the speed with which spots crossed the disk varied for different clusters.

This documented behavior is better understood today, but there is much still to learn about the solar cycle and its manifestation in sunspots. Schwabe (1843) observed sunspots for over 17 years and reconstructed an 11-year cycle based on

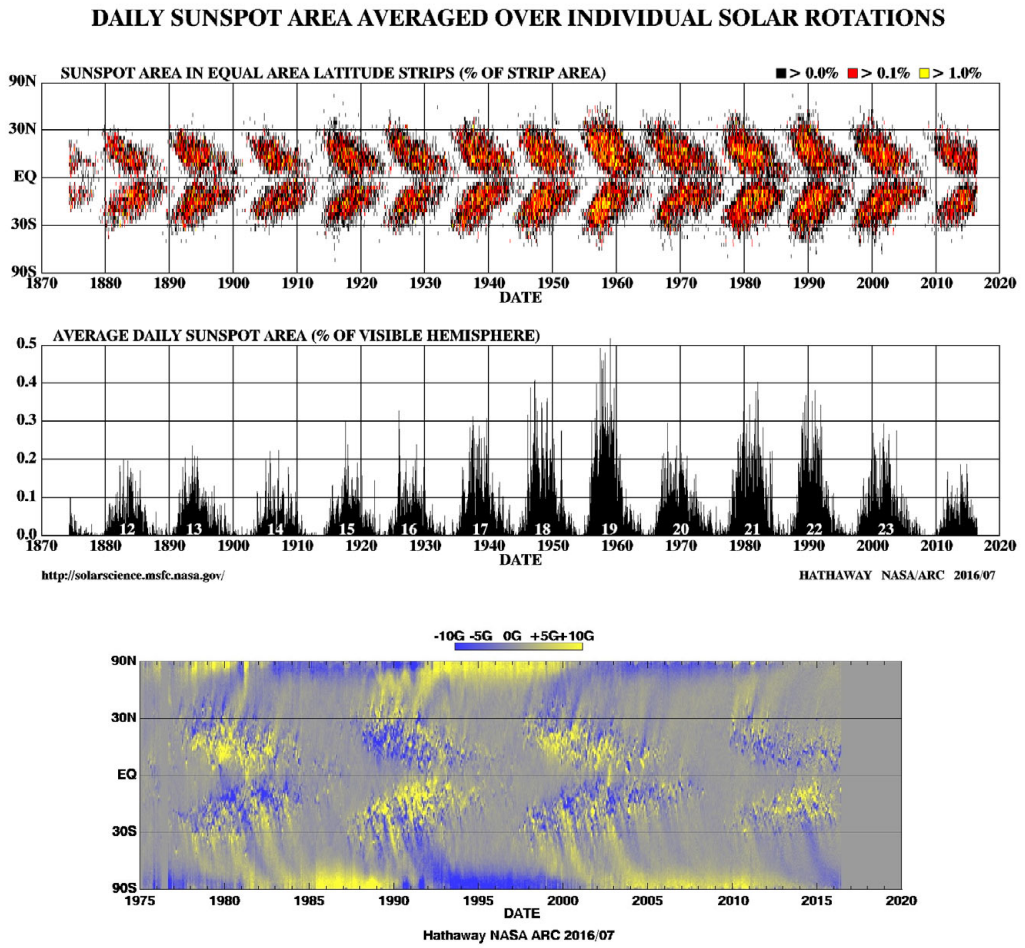

Figure 2.1: *Top:* Sunspot area in a butterfly diagram. Data is from the Royal Greenwich Observatory and updated monthly at http://solarscience.msfc.nasa.gov. *Middle:* Total sunspot area with solar cycle. *Bottom:* Butterfly diagram of the longitudinally averaged solar radial magnetic field, based on measurements from the Kitt Peak National Observatory and Solar and Heliospheric Observatory (Hathaway, 2010).

the number of observed sunspots. Rudolph Wolf combined these observations with historical sunspot observations such as those by Galileo, and in 1848 he introduced the relative sunspot number,

$$R = k(10g + s). \tag{2.1}$$

Here s is the number of individual spots, g is the number of groups of spots, and k is a so-called "observatory factor" dependent on location and instrumentation. Carrington (1858) observed that the latitude of spots changed during a cycle, moving from intermediate ($\sim \pm 35°$) to low latitudes and then forming anew at intermediate latitudes to repeat the cycle. The difference in motion of spots based on latitude was attributed to differential rotation, where the rotational velocity at the equator differs from that at high latitudes. Details of this cycle were later refined by Spörer (1890), who noted that the appearance of high latitude spots towards the end of a cycle indicated the beginning of a new cycle. The visualization technique of the change of these spot latitudes is called a "butterfly diagram", created by Maunder (1904) as a means to represent both spot latitude changes and spot density over the course of a solar cycle. The sum or average over one latitude of a value such as solar sunspots or magnetic field strength, when plotted over time, resembles the wings of a butterfly, hence the name, shown in Figure 2.1 (top).

Hale (1908) examined the magnetic fields within spots, based on the work of Zeeman (1897), who observed the splitting of spectral lines when under the influence of magnetic forces. Hale theorized that a magnetic field within a spot would similarly create observably different spectral lines than the surrounding gas due to the Zeeman effect, and confirmed this with a series of observations made at the Mount Wilson telescope. Further studies by Hale (1913) found that spots typically occur in pairs and that these pairs are bi-polar. Observations in 1919 revealed leading spots with opposite polarity from the 1913 observations, indicating a switch in polarity after each 11-year cycle. Lines drawn between the spots in such pairs had similar angles relative to the equator. This phenomenon was defined by Hale et al. (1919) as Joy's Law, after astronomer and co-author of the 1919 paper Alfred Harrison Joy. Joy's Law dictates that with bipolar spot structure, the leading spot usually is closer to the equator and leading spots usually have the same polarity in the one hemisphere, and the opposite polarity in the other hemisphere. The Sun's change in polarity was confirmed by Hale and Nicholson (1925), who concluded that combining two 11.5 year cycles of each polarity make a complete magnetic solar cycle of about 23 years. This cycle is evidence that the magnetic field is not created by the spots themselves, but rather indicative of much larger and more complex magnetic structures within the Sun itself.

Babcock and Babcock (1955) studied the entire solar disk in detail, focusing on the general magnetic field. A general field strength of about 1 G was measured near the poles. The bulk of the strong field was observed at higher latitudes (greater than $\pm 55°$), although fluctuations of over 2 G were also observed around spotted or active regions. If the magnetic field lines were frozen in (see Section 3.1, Equation 3.7 for an explanation of frozen-in field lines), then differential rotation near the surface of the Sun would wind up the poloidal field and amplify the solar toroidal magnetic field. A rough calculation based on the observed differential rotation of the Sun shows that magnetic field lines would be wound up over 5 turns in 3 years, significantly amplifying the toroidal field (Babcock, 1961). If the magnetic field is envisioned as ropes of magnetic flux, these would rise to the surface in loops, creating bipolar structures on the surface and providing a possible explanation for the bipolarity of sunspot pairs. Over time, this bipolar structure would drift towards the equator and poles, expand, and become neutralized. The reconnection and expulsion of these flux ropes would eventually reverse the polarity of the solar magnetic field every 11.5 years. The poleward component of the magnetic field is evident at higher latitudes in Figure 2.1, bottom. Leighton (1969) performed a quantitative analysis of this cycle using a simple kinematic model based on a closed series of magnetohydrodynamical equations and found that the model that agreed best with observations required radial variation for rotation and a strong concentration of shear near the equator. Leighton (1969) noted that the presence of flux ropes was not crucial to the model. The resulting field is never purely poloidal and the equatorward drift was noted as not due to differential rotation, but rather the propagation of the magnetic field itself. This is now termed the Babcock-Leighton mechanism.

Conventional thought until the 1970's was that the electromagnetic radiation of the Sun was constant. However, increasingly detailed measurements of the solar magnetic field implied an underlying process that would theoretically impact the solar irradiance (the outward radiant flux detected over a defined surface area) over the solar cycle. Missions such as the Solar Maximum Mission were launched to measure solar irradiance and compare results to other activity indicators, such as sunspots. Willson and Hudson (1991) used 9.75 years of flux measurements and found a correlation between luminosity and the photospheric changes that suggested that an underlying mechanism beyond thermal diffusion is responsible for the variations in irradiance. After over 30 years of such missions, Fröhlich (2012) examined the solar cycle with respect to irradiance and other factors and observed a correlation between changes in the radial component of the solar magnetic field and total solar irradiance, where the maximum (minimum) irradiance corresponded with the maximum (minimum) magnetic activity levels. This change is about 0.1% based on observations

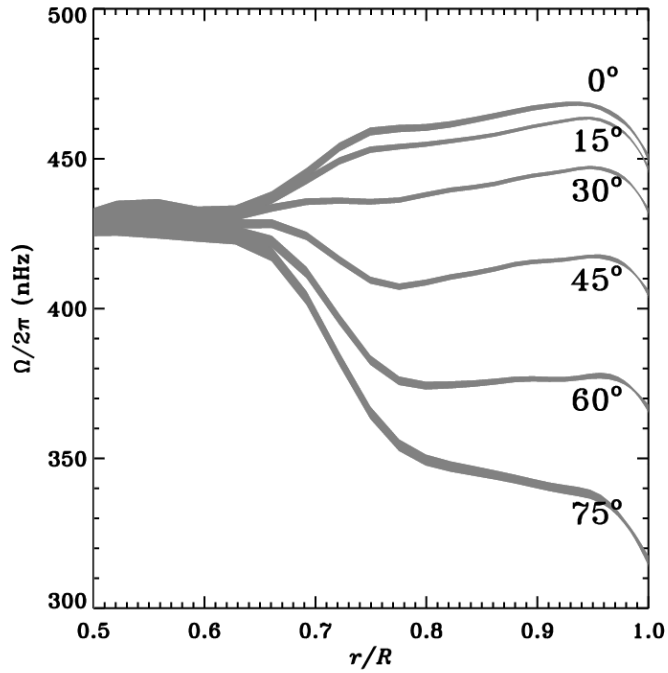

Figure 2.2: Rotation profile of the solar interior from helioseismology. Image credit: GONG/NSO/AURA/NSF.

beginning in 1978, and proxies such as sunspot number are needed to reconstruct solar irradiance from earlier time periods (Krivova et al., 2007). The higher irradiance corresponds to the higher magnetic activity level of the Sun, because although spots themselves are cooler and contribute negatively to the irradience, they cover a very small fraction of the surface as compared to the brighter phenomena, such as faculae produced by strong concentrations of magnetic field lines that contribute positively to the irradience.

Returning to Carrington's observations of the sunspot angular velcity dependence on latitude, it was observed that in general spots near the equator rotated faster than spots at higher latitudes. A formula was calculated from observations of these spots of $\omega(\text{degrees/day}) \propto \cos^{7/4}\theta$, where ω is the angular rotation rate and θ is the angle between the latitude and the pole (co-latitude). Observations of sunspots by Faye

(1883) found a relationship based on co-latitude where $\omega(\text{degrees/day}) \propto \cos^2\theta$. This more closely resembles the modern accepted form based on measurements of Doppler features of the solar surface by Snodgrass and Ulrich (1990),

$$\omega(\text{degrees/day}) = \text{A} + \text{B}\cos^2\theta + \text{C}\cos^4\theta, \tag{2.2}$$

where $A = 14.71$, $B = -2.39$, and $C = -1.78$. However, differential rotation in the Sun also depends on depth, and using tracers such as spots, supergranules, or the magnetic field requires knowledge of the depth at which such features are anchored. Helioseismology uses the high-frequency pressure modes to measure the differential rotation within the Sun at all depths shown in Figure 2.2 (e.g., Scherrer et al., 2012). The radiative zone of the Sun has largely uniform rotation, although the deepest interior regions are difficult to observe and may behave differently. This radiative zone extends until it reaches the bottom of the convection zone at $r \approx 0.7R_\odot$. This transition from the radiative zone to the convection zone occurs in a shear layer called the tachocline. The bulk of the convection zone then has differential rotation that has contours along cylinders 25° from the rotation axis. At $r \approx 0.95_\odot$, the near-surface shear layer begins, where the rotational velocity decreases outwards at all latitudes (Howe, 2009; Barekat et al., 2014, 2016, and references therein).

The tendency of spots to form along certain longitudes was noted by Ayyar (1932) and later by Losh (1939), who both found a tendency for the spot groups to form along certain longitudinal bands for the duration of a solar cycle, a phenomenon labeled an "active longitude". Vitinskij (1969) used a longer time series of sunspots and concluded that although active longitudes were a regular feature of solar cycles, they rarely lasted for more than one or two cycles. Balthasar and Schuessler (1983) noted that active longitudes with a 27-day period might be tied to the underlying magnetic structure and not the differential rotation in the convection zone. Berdyugina and Usoskin (2003) studied over a century of sunspot data and found active longitudes 180° apart with primary and secondary longitudes that switch approximately every 3.8 years, dubbed a "flip-flop", and that by accounting for differential rotation, conclude that the active longitudes persist for over 120 years. However, Pelt et al. (2006) find that the 120-year persistence is a likely artifact of the data analysis method and not physically real, and that active longitudes persist at most for about one cycle. Pelt et al. (2010) used a nonparametric statistical approach to analyze sunspot data and the underlying spot-generating mechanism and found that the underlying mechanism was affected by differential rotation. The spot-generating structure remained cohesive only up to 10–15 Carrington rotations. Furthermore, the northern and southern hemispheres were found to have slightly varying mean rotation rates with a difference of about 0.004 degrees/day.

2.1.1 Solar Activity Summary

The solar magnetic field can be characterized with the following elements:

- The Sun has a high number of spots at the height of solar activity and is virtually unspotted during periods of low activity. These spots cover a tiny fraction ($\approx 0.5\%$) of the solar surface, and solar irradiance increases with the number of spots due to the higher activity level of the Sun. This cycle repeats every 7–15 years.
- The polarity of the Sun is reversed every cycle, making the complete cycle to return to the same polarity at a given pole every 14–30 years. With regards to solar cycles tracked since 1755, the range is actually smaller, with cycles of only 20–25 years.
- The solar magnetic field is antisymmetric about the equator.
- Spots at the beginning of a cycle form at intermediate latitudes and drift towards lower latitudes. As the cycle progresses, new spots form at the intermediate latitudes. This tendency is referred to as the equatorward drift of the magnetic field.
- Active longitudes, or longitudes where sunspots tend to form, are influenced by differential rotation, known as the phase-mixing effect, and last typically only a year, although some may persist for a full cycle.
- The Sun has differential rotation, where the equator rotates faster than the poles. Thus it takes the equator about 27 days to rotate once, whereas the polar regions take 35 days to rotate once.

2.2 Magnetic Activity

It was surmised as early as 1915 by George Ellery Hale that if the Sun was magnetically active, then it was likely that so too were other stars if one was to consider the Sun as not particularly unique. However, methods to study these fields and extensive observations spanning decades would be needed to detect anything resembling the Sun's 22-year magnetic cycle. New techniques were needed in general to observe magnetic fields on stars based on contemporary knowledge of how the magnetic field manifests in the Sun.

Starspots were first theorized by Kron (1947) to explain the light curve observed for the binary system AR Lacertae. Deviations in the light curve from the expected

values for an eclipsing binary were postulated to be caused by large, cool patches on the surface of AR Lacertae B. Photometric observations of the K6V star HD 234677 revealed variability not adequately explained by flares (Chugainov, 1966). Starspots with temperatures a few hundred or more K lower than the surrounding gas were theorized to be the source of the slight but consistent changes in the light curves, as large, cool spots rotating into the line of sight would decrease the observed magnitudes of stars.

Wilson and Vainu Bappu (1957) measured the CaII H and K chromospheric emission lines for 185 stars. A discrepancy was observed between the intensity of H&K emission lines for stars belonging to open clusters as opposed to field stars, implying an inverse relationship between stellar age and emission intensity, assuming field stars are generally older than open cluster members. A tentative explanation was put forth by Wilson (1963) that if these H&K emission lines are akin to the ones observed in the Sun connected to the magnetic field and sunspots, then these lines in stellar spectra corresponded in a similar way to starspots. In March of 1966, a long-term project was undertaken to measure the H&K emission of 91 stars (Baliunas et al., 1995). This group of aptly named *Mt. Wilson stars* was later enlarged to include more targets and over 100,000 observations of stars of spectral type F2–M2, monitored for 25 years at Mt. Wilson, California. The observed variability of the H&K emission with time is used as an indicator of magnetic cycle of a star. Baliunas et al. (1995) classified these magnetic star cycles as cyclic, flat, variable, irregular, or some combination thereof. These classifications are not rigid, for example, stars classified as variable might be cyclic but with periods longer than the decades of observations, and other stars that are flat may be going through a Maunder minimum-like period of low activity.

The line emission of the Ca II H and K can be expressed as a non-dimensional quantity S to describe activity level so that

$$S = \frac{F_{\mathrm{H}} + F_{\mathrm{K}}}{F_{\mathrm{R}} + F_{\mathrm{V}}}, \tag{2.3}$$

where F_{H} and F_{K} are counts in the Ca II passbands and F_{R} and F_{V} are counts in the violet and red continuous bands, respectively. When this activity indicator is plotted against the color index of F and G stars, a gap is observed where there is an abrupt change in activity level from active to inactive stars (Vaughan and Preston, 1980). This gap containing few stars is the Vaughan-Preston gap, where chromospheric activity was observed to rapidly decline around an estimated stellar age of 10^9 years. Saar and Baliunas (1992) examined possible correlations between certain parameters, such as rotation rate, activity, and age, and found two distinct branches, one with

rapidly rotating young, active stars and another with older, slower inactive stars.

One possible parameter that can correlate with activity is the inverse Rossby number $\mathrm{Ro}^{-1} = 4\pi\tau_c/P_{\mathrm{rot}}$, where τ_c is the estimated convective turnover time based on, among other factors, the depth of the convection zone, and P_{rot} is the rotation period (Noyes et al., 1984). Brandenburg et al. (1998) found relationships between Ro^{-1}, the fractional chromospheric radiative loss R'_{HK}, and $P_{\mathrm{rot}}/P_{\mathrm{cyc}}$ where P_{cyc} is the dynamo cycle period. Stars were found to be active when $\log\langle R'_{\mathrm{HK}}\rangle > -4.75$. Saar and Brandenburg (1999) expanded the sample to include photometric variable stars and found a superactive branch at lower $\omega_{\mathrm{cyc}}/\Omega$, where $\omega_{\mathrm{cyc}} = 2\pi P_{\mathrm{cyc}}$ and Ω is the mean angular velocity of the star. This branch decreased with increasing Ro^{-1} populated by close binaries. Additionally, RS CVn stars were found in a transition region between the active and superactive branches for Rossby numbers in the range $2.0 \leq \log \mathrm{Ro}^{-1} \leq 2.4$. Lehtinen et al. (2016) used a larger sampling of stars including those from Brandenburg et al. (1998) and found a peak value for $P_{\mathrm{rot}}/P_{\mathrm{cyc}}$ at $\mathrm{Ro}^{-1} = 1.42$, indicating a change from active to inactive branches. The activity of a star is correlated with the depth of the convection zone and rotation rates; stars with too shallow of a convection zone or rotating slowly, such as older stars, showed little to no activity. Furthermore, a division was found at $\log R'_{\mathrm{HK}} = -4.46$ between less active stars with no observable active longitudes and active stars with long-term active longitudes.

If the Ro, and by extension, rotation, is examined in terms of X-ray luminosity following the assumption that X-rays are generated in super-hot plasmas of the coronas of magnetically active stars, then a relation is found where $R_{\mathrm{X}} \equiv \mathcal{L}_{\mathrm{X}}/\mathcal{L}_{\mathrm{bol}} \propto \mathrm{Ro}^{\beta}$ where $\mathcal{L}_{\mathrm{X}}$ is the X-ray luminosity, $\mathcal{L}_{\mathrm{bol}}$ is the bolometric luminosity, and β may range from -1.9 (Noyes et al., 1984) to -2.7 (Wright et al., 2011), based on the star sample and fitting method used. This relation holds only for the unsaturated regime. As Ro increases to ≈ 0.13, R_{X} saturates at about -3.13 (Wright et al., 2011). This relationship holds regardless of spectral type, and the implication seems to be that two different dynamo types operate in the saturated and unsaturated regimes.

Long-term monitoring of active stars continued using various other observation methods, and properties of the magnetic fields can be observed both directly and indirectly. Time series of photometric data can be used for light curve modeling, where starspots cause variations in the light curve based on the phase of the spots, and longer term activity cycles can be calculated using various statistical methods such as those used in Papers IV (Kajatkari et al., 2015) and V (Olspert et al., 2015) as well as others (e.g., Bopp and Evans, 1973; Vogt, 1981; Strassmeier, 1988; Jetsu and Pelt, 1996). There are numerous Automatic Photometric Telescope projects at observatories such as SpectraBot, Fairborn, SAAO, among others (see e.g., Berdyug-

ina, 2005), that provide data by observing photometric target stars repeatedly over long periods of time. Data spanning decades is necessary for observing stellar cycles of the order of years. Another approach is to seek periodicities from irregularly sampled time series utilizing special statistical methods. This thesis uses two different methods of this type, namely the Continuous Period Search method (Lehtinen et al., 2011) and the Carrier Fit method (Pelt et al., 2011), described in more detail in Sections 5.1.2 and 5.1.3. Spectroscopy can also be used to measure the Ca II H&K lines by examining only certain molecular lines that appear in the cooler, spotted regions of stars with a high effective temperature (Vogt, 1979). Zeeman line splitting in the presence of a magnetic field and rapid rotation displaces metal absorption lines and can be measured using polarimetry (Babcock, 1947). High-resolution spectropolarimetry can be used to derive magnetic field vectors of magnetically active stars from the Stokes I, Q, U, & V parameters (e.g., Semel, 1989). Asteroseismology is the use of the oscillation modes from gravity and pressure waves observed in the frequency spectrum of stars to reconstruct the interior, akin to helioseismology albeit with a much lower resolution (e.g., Brown and Gilliland, 1994; Cantiello et al., 2016).

Certain techniques such as inverse methods can use these observations to reconstruct magnetic field and activity cycles as well. The assumption that stellar spots are analogous to sunspots is usually made, in other words, spots are caused by strong magnetic field lines inhibiting convection thus creating cool spots that then cause deviations in observations from what could be expected of a uniform surface. In the inversion method of Doppler Imaging, the Doppler effect of stellar rotation is used to reconstruct stellar surface maps from small fluctuations in spectral lines over an observing season. This method is discussed in more detail in Section 6, and is used for determining spot latitudes as well as longitudes in Paper VI (Cole et al., 2016) of the thesis. Inverse techniques can also be applied to to photometric data to recreate surface maps, but latitudes and shapes of recovered spots is largely unknown and only the longitudes can be recovered with accuracy (Berdyugina et al., 2002).

Stars that show particularly high levels of magnetic activity are categorized in several groups usually named after a prototype star. These groups include red dwarfs and BY Draconis stars, T Tauri stars, RS CVn stars, FK Comae stars, W UMa stars, and Algol stars. Red dwarfs and BY Draconis stars are late-type stars of spectral class G, K, or M that display luminosity variability due to chromospheric activity and large spots. BY Draconis stars are covered in more detail in Section 2.3.1. T Tauri stars are pre-main sequence single stars of spectral type F5–G5 that are more luminous than main-sequence stars and the initial 11 targets comprising this group have an observed light curve variability of about three magnitudes (Joy, 1945). The observed erratic three-magnitude changes are not due to starspots but instead

are caused by other mechanisms. RS CVn stars, named after the prototype star RS Canum Venaticorum studied by Hall (1972), are rapidly rotating binaries consisting of a G–K giant or subgiant and G–M subgiant or dwarf, with observed variability in the chromospheric emission in the CaII H&K lines, and variability of up to 0.6 magnitudes in the V-band (Hall, 1976). FK Comae stars, with the prototype star FK Comae, are very rapidly rotating late-type giants of spectral class G or K that have a 0.1–0.2 magnitude variability in the V-band caused by asymmetrical cool spots and very strong chromospheric emission (Bopp and Stencel, 1981). W UMa stars, prototype W Ursae Majoris, are solar-type eclipsing binary systems that share a common envelope, are of spectral type A5–K9, and have orbital periods of less than a day (Selam, 2004). Algols are rapidly rotating eclipsing binaries with a main sequence primary star of spectral type B–F, and a secondary subgiant star of spectral class G or K with a deep convective envelope (e.g., Chen et al., 2006). Other types include cataclysmic variables, some rapidly rotating giants, and other main sequence single stars with indicators of magnetic activity.

Stellar spots can be described in terms of temperature, spot filling factor, latitude, longitude, and activity cycles. The temperature of spots on a stellar surface can be as much as 1500 K cooler than the unspotted surface (e.g., Hackman et al., 2011). The spot filling factor describes how much of the total surface area is covered in spots. The method of calculating the spot filling factor varies based on the observational technique, and results have stellar spots covering a significant percentage of the stellar surface for the more active stars. Spots have been observed to appear at any latitude ranging from the equator to the pole. There is some controversy regarding whether the central spectral line filling is due to polar spots or chromospheric effects concentrated near the poles, however, Bruls et al. (1998) found that the spectral lines are not as sensitive to chromospheric effects as they are to spots. Additionally, methods such as interferometry can be used to confirm polar spots observed by other methods (Korhonen et al., 2010). For some stars, spots have been observed to occur at the same longitude over long periods of time. These active longitudes can be observed both in photometry and Doppler Imaging, provided there are enough observing seasons to establish the longitudinal distribution of spots with time. One of the earliest stars with observed active longitudes is FK Com, where the term "flip-flop" was used to describe behavior where one longitude where spots developed would suddenly cease to be active and a longitude approximately 180° from it would take over (Korhonen et al., 2002; Hackman et al., 2013). Some caution must be exercised when interpreting active longitudes and spots, as certain methods may introduce a bias, such as fitting light curves to two spot models (Zeilik et al., 1988; Henry et al., 1995). Some binary RS CVns such as II Peg are of interest because the binary

system makes the period well-known, and the active longitudes observed rotate with a different period than the star (Lindborg et al., 2013). Lehtinen et al. (2016) found that active longitudes calculated from photometric light curves appear on the more active stars, but the coherence time and rotation rate of these active longitudes may vary. In general, active longitudes rotate at a faster rate than the star itself.

Long term cycles can be calculated from a time series of activity indicators such as the previously mentioned CaII H and K emission lines, mean brightness, light curve amplitude, among others. Calculations of these cycles, however, are limited by the length of time of observing programs that include these stars as targets. Stars have indications of cycles as short as a few years and so more than one cycle period may be observed. For example, calculated cycle periods for LQ Hydrae range from 3.2 years (Messina and Guinan, 2003) up to 12.4 years (Oláh et al., 2009). Longer cycles are probable, and as pointed out by Baliunas et al. (1995), there exists an artificial upper limit to observed cycles due to the limited span of years of observing programs so that stars appearing to have irregular or variable activity might instead just have cycles of longer than 25 years. There is also the possibility that some otherwise cyclic stars may be experiencing a Maunder-minimum phase in their activity cycle and thus appear to have a flat light curve.

2.2.1 Differential Rotation

Differential rotation is usually listed in terms of the rotational shear relative to the equatorial rotation, or as the relative differential rotation coefficient

$$k = \frac{\Delta\Omega}{\Omega_{\rm eq}}, \tag{2.4}$$

where $\Omega_{\rm eq}$ is the equatorial rotational velocity and $\Delta\Omega$ is the difference between the equatorial rotation and polar rotation. Assuming a solar-like differential rotation profile, an equation for fitting $\Omega(\theta)$ would be

$$\Omega(\theta) = A + B\sin^2\theta \tag{2.5}$$

where θ is the latitude, and A and B are parameters obtained usually by a best fit. Variations in photometric light curves may be due to spots at various latitudes experiencing differential rotation. Relative differential rotation can be estimated from period fluctuations observed in photometry, written as

$$Z = \frac{6\Delta P_{\rm w}}{P_{\rm w}}, \tag{2.6}$$

where $P_{\rm w}$ is the observed weighted period of rotation, $\Delta P_{\rm w}$ is the standard deviation, and the factor 6 accounts for the $\pm 3\sigma$ variation, and $Z \approx |k|$ (Jetsu, 1993; Lehtinen et al., 2012). Another way to quantify differential rotation for stars is to use the method by Henry et al. (1995) where $k = (P_{\rm max} - P_{\rm min})/P_{\rm avg}$, in other words, using the longest period $P_{\rm max}$, the shortest period $P_{\rm min}$, and the average period $P_{\rm avg}$. The solar value is $k \sim 0.2$, but stellar values tend to be much smaller. For example, estimates for k for LQ Hya is of the order 0.02 (Jetsu, 1993; You, 2007; Lehtinen et al., 2012), with a rotational period of approximately 1.6 days.

There are several ways of determining a star's relative differential rotation. Inverse methods can be used to fit spots to photometric light curve variations (Hall, 1972). Period fluctuations can be calculated from the Lomb-Scargle periodogram or a χ^2 fitting method of either photometric or CaII H&K emission (e.g., Jetsu, 1993; Henry et al., 1995; Donahue et al., 1996; Messina and Guinan, 2003; Reinhold and Reiners, 2013). Some stars may exhibit anti-solar differential rotation, where the equator rotates slower than the poles, in which case k should be negative (Reinhold and Arlt, 2015). However, their method of determining k only gives the amplitude of the difference in rotation, and if these fluctuations are due to two or more spots of unknown latitudes, then the calculated k may actually be less than the actual differential rotation if the spots do not occur at both high and low latitudes at the same time. Differential rotation can also be estimated from deviations in the rotation period of the chromospheric emission or photometry by using a Fourier analysis (Lanza et al., 1993). Another way of determining differential rotation in the Sun is from tracing spots and magnetic features, and similar methods can be applied to calculating stellar differential rotation. By cross-correlating latitudinal slices of maps of either spot structures or magnetic structures using Doppler Imaging or Zeeman Doppler Imaging respectively, an upper limit to the relative differential rotation can be calculated from the changes in longitude of observed structures (e.g., Donati and Collier Cameron, 1997; Petit et al., 2002). The spectral lines themselves may also be used to estimate differential rotation by using a Fourier transform and accounting for such effects as limb darkening, the inclination angle, and starspots (Reiners and Schmitt, 2002). A Fourier transform can also be applied to differential interferometry (Domiciano de Souza et al., 2004). Another method for determining differential rotation is to use asteroseismology, where the splitting of the modes of pressure and gravity wave oscillations provide information regarding surface differential rotation (Gizon and Solanki, 2004; Lund et al., 2014).

All these methods of calculating the relative differential rotation are limits only, as the rotation velocity of some latitudinal regions may differ even more but contain no tracer of differential rotation. Direct tracing of the starspots does not account

for the spot anchorage depth, and it is possible that the magnetic structure, spot regions, and stellar matter are not always connected to each other (Donati et al., 2003a). The relation between the differential rotation period ΔP and the rotation period $P_{\rm rot}$ can be formulated as

$$\Delta P \propto P_{\rm rot}^{n}, \tag{2.7}$$

where n varies based on spectral type and method of determining differential rotation. Donahue et al. (1996) found a relation of $n = 1.3$ for F, K, and G stars, while Messina and Guinan (2003) found a relation of $n = 1.42$ from a sample of 6 type G stars. Henry et al. (1995) and Barnes et al. (2005) found steeper values of $n = 1.76$ and 1.85 respectively. These values are somewhat close to the theoretical values calculated from numerical simulations by Rüdiger et al. (1998) where $n = 1.15 \ldots 1.30$. Lehtinen et al. (2016) found a relation of $n = 2.36$ of F–K stars of single and multiple star systems. This last value is the closest to the theoretical value $n = 2.6$ found by Kitchatinov and Rüdiger (1995) using numerical models with rotation rates around solar values. Küker and Rüdiger (1999) hypothesized that stars without a tachocline such as that in the Sun may have a different dynamo mechanism and it was found that as rotation increases, an axisymmetric field switches to a non-axisymmetric field while differential rotation becomes weaker with increasing rotation.

2.2.2 Stellar Activity Summary

Observations have revealed the following characteristics of magnetically active stars:

- Stellar spots for active stars may be much larger than solar spots, covering over 30% of the stellar surface, as seen in Figure 2.3 The irradiance is therefore anti-correlated with the magnetic activity level, unlike for the Sun. Due to resolution limits, it is not known if these starspots are either one large spot or groups of smaller spots.

- Observations of stellar magnetic activity are made via methods such as photometry, spectroscopy, asteroseismology, Zeeman Doppler Imaging, and Doppler Imaging. Unlike the Sun, these observations only span decades at best instead of centuries, which places limits on the observed cycle periods.

- Spots may form at any latitude, including near the pole.

- Similarly to the Sun, spots may exhibit the tendency to appear at certain longitudes, and this tendency is stronger with the more rapid rotating stars.

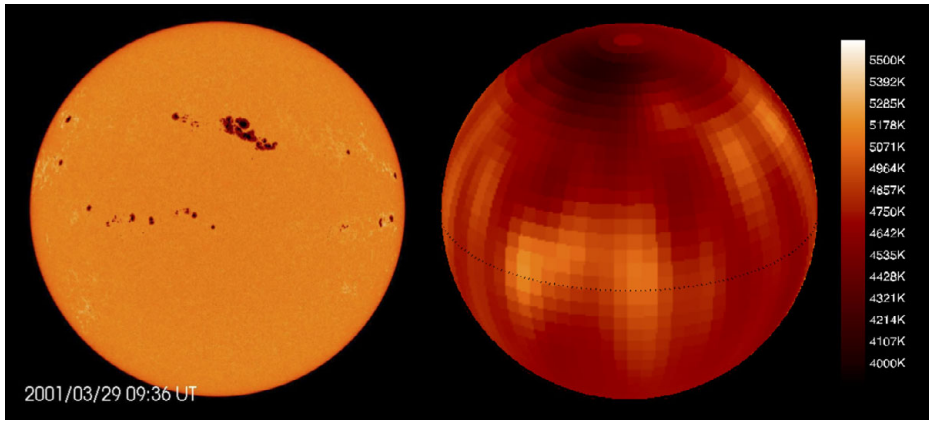

Figure 2.3: *Left:* Large sunpot group, data from SOHO/MDI. (Image credit: ESA and NASA) *Right:* LQ Hya during May–June, 1999. Modified from from Paper VI, Figure 3.

These active longitudes may persist for several years, and the primary and secondary minima may also periodically switch (flip-flop).

- The relative differential rotation of active stars may be much weaker than that of the Sun, and so the spot-generating mechanisms behave differently, particularly in fully convective stars. Additionally, differential rotation may be anti-solar, in other words, faster rotation at the poles than the equator.

2.3 Solar Analogues

Stars with properties that resemble the Sun are classified as solar-type stars, solar analogues, and solar twins (Cayrel de Strobel, 1996). These are of particular interest for studying as their properties resemble that of the Sun. The criteria for solar-type star is the least rigid. For a star to qualify as a solar-type star, it must be of types F8V – K2V, with corresponding B–V color indexes between 0.50 and 1.00. As these stars have significant convective envelopes, they are also chromospherically active. Solar analogues are a sub-group of solar-type stars, and typically Population I single stars. Metallicity, effective temperature, and kinematic properties should not drastically vary from solar values and these stars should be in the same evolutionary phase, in other words, on the main sequence, although they may be much younger than the

Sun. Solar twins are a subgroup of solar analogues which have properties nearly identical to that of the Sun, including age, magnetic activity, luminosity, rotation profile, and metallicity. Because of this, solar twins are quite rare, and it is primarily solar analogues that are studied with respect to magnetic fields and starspots.

2.3.1 BY Draconis-type Stars

BY Draconis-type stars are late-type stars that exhibit variability as a result of starspots or chromospheric activity. The stellar prototype is the namesake, BY Draconis, a class K4V + K7.5V variable binary star (Popper, 1953). These stars are of spectral type G–M. The variability is usually less than half a magnitude, and the time-scale for periodicity found in the light curves is similar to that of mean rotational velocity of the star, typically 1–10 days for rapid rotators. Activity cycles calculated from changes in the light curves of these stars are typically of the order of months or years. Two such BY Draconis-type stars are studied here in detail: LQ Hydrae (HD 81228, HIP 46816) and V352 Canis Majoris (HD 42162, HIP 29568). Both stars are rapidly-rotating young solar analogues exhibiting strong levels of activity.

V352 Canis Majoris

V352 CMa is one the nearby young solar analogues with rapid rotation and an active chromosphere. It has a spectral class G6.5 (Gray et al., 2006), and an estimated age of $40-800$ Myrs (Gaidos et al., 2000). The star is the parent member of a multiple star system which includes HD 43162a and HD 43162b (Mason et al., 2001). The nearly constant $v_{\rm rad} = 21.7$ (Gaidos et al., 2000) indicates orbital planes of the companions nearly perpendicular to the line of sight. Although the star has been identified as having a debris disk, there are no known planets (Kóspál et al., 2009). V352 CMa has low-amplitude light curves, so while not a candidate for Doppler Imaging, it is a candidate for testing the reliability of photometric methods and refining the rotational period. This star is studied in Paper IV of the thesis.

LQ Hydrae

LQ Hydrae (HD 82558, HIP 46816, GL 355) is a young solar analogue located approximately 18.3pc away. It is of spectral type K2V (Cutispoto, 1991), and classified as a BY Draconis-type star (Fekel et al., 1986). The age of LQ Hya is approximately 51.9 ± 17.5 Myr (Tetzlaff et al., 2011), as compared to the solar age of 4.57 Gyr, placing it among the zero age main sequence stars. The mass of LQ Hya is estimated to be $0.8 \pm 0.1 M_{\odot}$ It has an estimated rotation period of 1.601136 ± 0.000013 days

Table 2.1: Chosen stellar parameters for V352 Canis Majoris. References are as follows: (1) Cutispoto et al. (1999), (2) Gaidos et al. (2000), and (3) Santos et al. (2004).

Parameter	Value	Reference
Age	$70 - 800$ Myrs	2
Temperature	$T_{\rm eff} = 5480$K	2
Gravity	$\log g = 4.48$	3
Rotation velocity	$v \sin i = 5.7$ km/s	2
Rotation period	$P = 7\overset{\rm d}{.}2$	1
Metallicity	$\log[Fe/H] = -0.01$	3

Table 2.2: Chosen stellar parameters for LQ Hya. References are as follows: (1) Jetsu (1993), (2) Rice and Strassmeier (1998), (3) Donati (1999), and (4) Kovári et al. (2004).

Parameter	Value	Reference
Temperature	$T_{\rm eff} = 5000$K	3
Gravity	$\log g = 4.0$	2
Inclination	$i = 65°$	2
Rotation velocity	$v \sin i = 26.5$ km/s	3
Rotation period	$P = 1\overset{\rm d}{.}6001136$	1
Metallicity	$\log[M/H] = 0$	4
Macroturbulence	$\zeta_{\rm t} = 1.5$ km/s	2
Microturbulence	$\xi_{\rm t} = 0.5$ km/s	2

(Jetsu, 1993). The estimates of the metallicity of LQ Hya range from [Fe/H]$= -0.74$ (Zakhozhaj and Shaparenko, 1996) to [Fe/H]$= +0.60$ (Haywood, 2001). Based on the range of parameters, the radius estimates of LQ Hya range from $0.79 - 1.0 R_\odot$ (Alekseev, 2003; Strassmeier, 2002).

LQ Hya is a rapid rotator with low differential rotation. Lehtinen et al. (2016) estimates a value based on the deviation of measured periods from the mean period of $Z = 0.017$ (Eq. 2.6). Even lower estimates were obtained from Zeeman Doppler Imaging by Donati et al. (2003a) of $k = 0.002$ (Eq. 2.4). Activity cycles have been estimated to be between 3.4 years (Messina and Guinan, 2003) and 12.4 years (Oláh et al., 2009). This star is studied in Papers V and VI of this thesis.

3 Dynamo Theory

If the prestellar cloud that eventually formed into the Sun had a fossil field of 1 nT, and collapsed without any loss of the magnetic field, as a result the Sun would have had a field of 10^6 T. This magnetic field would then decay through diffusion, but the timescale of this process is of the order of 10^{10} years, or more than double the age of the Sun.

But astrophysical objects are not such simple systems and instead are often turbulent, which significantly influences the magnetic field. A plasma flow is considered turbulent when the inertial forces are sufficiently stronger than the viscous forces. This is characterized by the Reynolds number,

$$\mathrm{Re} = \frac{U_{\mathrm{rms}} L}{\nu}, \tag{3.1}$$

where ν is the kinematic viscosity. $\mathrm{Re} \gg 1$ indicates turbulent flow while $\mathrm{Re} < 1$ indicates laminar flow. In the case of the Sun, the convection zone has typical velocities (top to bottom) $U_{\mathrm{rms}=}10^5 \ldots 10^3\,\mathrm{cm\,s^{-1}}$, kinematic viscosity $\nu = 10 \ldots 1\,\mathrm{cm\,s^{-1}}$, and a characteristic length scale based on mixing length theory $L = 10^8 \ldots 10^{10}\,\mathrm{cm}$. The corresponding range of Reynolds numbers would be $\mathrm{Re} \sim 10^{12} \ldots 10^{13}$. Flows are considered turbulent when Re exceeds 10^3 or so, a condition certainly met in the solar convection zone. In stars, convection can be observed through the phenomenon of microturbulence, where convective velocities broaden spectral lines (see e.g., Hundt, 1973). An estimate of turbulent diffusion in the Sun is of the order of $10^{13}\,\mathrm{cm^2\,s^{-1}}$, based on the characteristic length scales and velocities, and therefore this mechanism would more rapidly diffuse away any fossil field than molecular diffusion alone. Hence, a mechanism for generating the magnetic field is required.

Additionally, the complexity of the solar magnetic field, the latitudinal drift of sunspots, and the amplified magnetic fields in sunspots cannot be adequately explained by processes limited to dissipation, reconnection, or the cascade of energy from larger to smaller scales due to turbulence. Some other mechanism that regenerates the magnetic field is needed. Dynamo theory postulates a mechanism whereby the kinetic energy of a conducting fluid or plasma is converted into magnetic energy

via electromagnetic induction. Therefore the Sun or any other star with sufficient turbulence and a seed magnetic field may generate a self-maintaining general magnetic field under the premise of dynamo theory.

3.1 Magnetohydrodynamics

Magnetohydrodynamics (MHD) examines the electrical and magnetic properties of moving conducting fluids, derived from Maxwell's equations and the conservation equations of mass, momentum, and energy. A plasma can be treated as a fluid when the particles are sufficiently coupled by collisions and the relevant length scales are greater than the Debye length. The MHD description is then valid for a plasma (Boyd and Sanderson, 2003, e.g.,).

The basic quantities are the electric field $\boldsymbol{E}$, the magnetic field $\boldsymbol{B}$, the magnetic permeability μ, the electrical permittivity ϵ, the current density $\boldsymbol{J}$, the electrical conductivity σ, the fluid velocity $\boldsymbol{U}$, the charge density ρ_q, and the time t. The Maxwell equations that relate these quantities are Gauss's Law for electric fields,

$$\boldsymbol{\nabla} \cdot \boldsymbol{E} = \frac{\rho_q}{\epsilon}, \tag{3.2}$$

the Mawell-Faraday equation,

$$\boldsymbol{\nabla} \times \boldsymbol{E} = -\frac{\partial \boldsymbol{B}}{\partial t}, \tag{3.3}$$

Ampere's Law,

$$\boldsymbol{\nabla} \times \boldsymbol{B} = \mu \boldsymbol{J}, \tag{3.4}$$

Gauss's Law for magnetism,

$$\boldsymbol{\nabla} \cdot \boldsymbol{B} = 0, \tag{3.5}$$

and Ohm's Law modified with the Lorentz force,

$$\boldsymbol{J} = \sigma(\boldsymbol{E} + \boldsymbol{U} \times \boldsymbol{B}). \tag{3.6}$$

These are combined to derive the induction equation,

$$\frac{\partial \boldsymbol{B}}{\partial t} = \boldsymbol{\nabla} \times (\boldsymbol{U} \times \boldsymbol{B}) - \boldsymbol{\nabla} \times \eta(\boldsymbol{\nabla} \times \boldsymbol{B}). \tag{3.7}$$

The magnetic diffusivity η is related to the magnetic permeability and electric diffusivity by $\eta = 1/\sigma\mu_0$. If η is constant and Gauss's law is used, then sometimes last term on the right hand side is written as $\boldsymbol{\nabla} \times \eta(\boldsymbol{\nabla} \times \boldsymbol{B}) = \eta \boldsymbol{\nabla}^2 \boldsymbol{B}$.

Table 3.1: Notation for field symmetry based on parity $\mathcal{P}$ and measure of axisymmetry $\mathcal{M}$

	$\mathcal{M}=0$	$\mathcal{M}=1$
$\mathcal{P}=+1$	$\mathcal{S}0$	$\mathcal{S}1$
$\mathcal{P}=-1$	$\mathcal{A}0$	$\mathcal{A}1$

Equations 3.7 and 3.5 describe the evolution of the magnetic field $\boldsymbol{B}$ over time and the forces that act back upon that field. The ratio of the terms on the right hand side of Equation 3.7 determines how conductive versus diffusive the fluid is:

$$\frac{\boldsymbol{\nabla}\times(\boldsymbol{U}\times\boldsymbol{B})}{\boldsymbol{\nabla}\times(\eta\boldsymbol{\nabla}\times\boldsymbol{B})}\approx\frac{U_{\rm rms}L}{\eta}\equiv\mathrm{Rm}. \tag{3.8}$$

Rm is the magnetic Reynolds number, $U_{\rm rms}$ is the characteristic velocity, and L is the length scale of the eddies. If η is very small due to a high electrical conductivity, the denominator vanishes and the plasma or fluid is considered ideal. The magnetic field lines are then considered "frozen in" to the flow, where any distortions to magnetic field lines are a result of the flow and not other dissipative effects. If η is large enough, then the magnetic field dissipates faster than it is regenerated. Some local diffusion is required for effects such as magnetic reconnection to occur.

Symmetry

The final configuration of the magnetic field in a spherical dynamo may be symmetric or asymmetric or some combination thereof, quantified by the parity,

$$\mathcal{P}=\frac{E^{(\mathrm{S})}-E^{(\mathrm{A})}}{E^{(\mathrm{S})}+E^{(\mathrm{A})}}, \tag{3.9}$$

where $E^{(\mathrm{S})}$ and $E^{(\mathrm{A})}$ are respectively the energies of the symmetric and antisymmetric parts of the magnetic field with respect to the equator (e.g., Moss et al., 1995). A parity of $+1$ indicates a purely equatorially symmetric field, and -1 denotes a purely equatorially antisymmetric field.

If Laplace's spherical harmonics Y_l^m are used to describe a magnetic field, then the $m=0$ mode corresponds to axisymmetry, and $l-m$ corresponds to a symmetric (antisymmetric) field about the equator if even (odd). A diagnostic for the axisymmetry of a field configuration is

$$\mathcal{M}=1-\frac{E^{(0)}}{E}. \tag{3.10}$$

Here, $E^{(0)}$ is the energy of the $m = 0$ mode and $E = E^{(\mathrm{S})} + E^{(\mathrm{A})}$ is the total energy of the field. A completely axisymmetric field will have $\mathcal{M} = 0$ and a completely non-axisymmetric field will have $\mathcal{M} = 1$. The field symmetry is often referred to in terms of symmetry and dominant mode m, so that a symmetric field is denoted by $\mathcal{S}m$ and an antisymmetric field by $\mathcal{A}m$. Table 3.1 shows the conversion from $\mathcal{M}, \mathcal{P}$ to $\mathcal{A}m$ and $\mathcal{S}m$ notation. $\mathcal{S}1$ and $\mathcal{A}1$ actually denote a combination of $\mathcal{S}1, \mathcal{S}3, \mathcal{S}5, \ldots$ modes and $\mathcal{A}1, \mathcal{A}3, \mathcal{A}5, \ldots$ modes, respectively.

The Sun is an example of a star that is mostly axisymmetric. The strong differential rotation winds up the field to a toroidal configuration. Axisymmetry is broken by starspots, flares, and other chaotic phenomena, but the dominant mode is $\mathcal{M} \sim 0$. The toroidal magnetic field is antisymmetric about the equator, but the poloidal field is more interesting. For most of a regular solar cycle, the poloidal field is antisymmetric about the equator, so that $\mathcal{P} \sim -1$. However, this dipolar field switches with the solar cycle, and at solar maximum takes on a quadrupolar structure that is symmetric about the equator, giving $\mathcal{P} \sim +1$. So the Sun favours a cycle of $\mathcal{A}0$ and $\mathcal{S}0$ with its activity cycle (e.g., Dikpati and Gilman, 2001a,b). However, there are historically long periods when the Sun remained at low activity level, for example, the Maunder Minimum dating 1645–1715, and the modes appear to have been more mixed, as estimated from records of sunspot cycles (e.g., Weiss and Tobias, 2016).

Stellar phenomena such as active longitudes and flip-flops found on stars with deeper convection zones and faster rotation seem to be indicative of non-axisymmetric fields, implying $\mathcal{M} \sim 1$. Symmetry can be estimated from stellar observations but limitations exist in how much of the star is visible based on inclination angle and method of observation. Photometry can only provide information of longitudes and lifetimes of large spots, while Doppler Imaging can provide latitudinal information about spots (e.g., Piskunov et al., 1990; Jennings et al., 1990). Additionally, the temperature maps and magnetic fields are not necessarily correlated (e.g., Kochukhov et al., 2013). The degree of axisymmetry of the magnetic field can be observed via Zeeman Doppler imaging, and stars such as II Peg are observed to have non-axisymmetric fields that are stronger when the star is more active, and the observed possible minimum had more of a dipolar, and hence axisymmetric structure (e.g., Skelly et al., 2010; Donati, 2011; Hackman et al., 2016). This behavior is typically found in stars above the Vaughan-Preston gap. More complex dynamo systems are needed to explain this observed difference (Tuominen et al., 2002).

3.1.1 Mean-field Theory

Mean-field theory approaches the problem of handling both large and small scales by decomposing any given field into the overall average behavior and the fluctuations. For the purpose of this thesis, only the mean-field decomposition of the magnetic field is relevant so that only the induction equation (Eq. 3.7) is considered. Although not officially formulated as such at the time, this idea of breaking down a general field into smaller components was initially presented by Parker (1955), where rotation acting upon convection eddies in a stratified convection zone was shown to be able to regenerate the poloidal field, which in turn can regenerate the toroidal field through differential rotation. Cowling's antidynamo theorem postulated that an axially symmetric magnetic field does not induce the currents necessary to regenerate itself (Cowling, 1933). Parker's theorem provides the missing link by introducing complexity in the form of non-axisymmetric helical turbulence. However, it was Steenbeck et al. (1966) who quantified this into mathematical form with the help of the mean-field approximation (Moffatt, 1978; Krause and Rädler, 1980).

Reynolds Decomposition

According to mean-field theory, any field can be broken down into an average, in other words, the expected value of an ensemble, and a fluctuating part. The method of representing this is the Reynolds decomposition. The following notation is used: the total is denoted in capital letters, for example, a generic field $\boldsymbol{F}$, the mean component of $\boldsymbol{F}$ is indicated by an overbar, $\overline{\boldsymbol{F}}$, and the fluctuating portion is denoted by a lowercase letter, $\boldsymbol{f}$. This fluctuating part is the difference between the total field and the mean field, so that

$$\boldsymbol{F} = \overline{\boldsymbol{F}} + \boldsymbol{f} \tag{3.11}$$

If $\boldsymbol{G}$ is another fluctuating field, then the Reynolds rules can be used to relate the mean and fluctuations of these two fields as follows:

$$\overline{\overline{\boldsymbol{F}}} = \overline{\boldsymbol{F}}, \tag{3.12}$$

$$\overline{\boldsymbol{f}} = 0, \tag{3.13}$$

$$\overline{\boldsymbol{F} + \boldsymbol{G}} = \overline{\boldsymbol{F}} + \overline{\boldsymbol{G}}, \tag{3.14}$$

$$\overline{\overline{\boldsymbol{F}}\,\overline{\boldsymbol{G}}} = \overline{\boldsymbol{F}}\,\overline{\boldsymbol{G}}, \tag{3.15}$$

$$\overline{\overline{\boldsymbol{F}}\boldsymbol{g}} = 0. \tag{3.16}$$

Additionally, with respect to derivatives in time or space, the following are also approximately true for horizontal or spatial averages:

$$\overline{\frac{\partial \boldsymbol{F}}{\partial x}} = \frac{\partial}{\partial x}\overline{\boldsymbol{F}}, \tag{3.17}$$

$$\overline{\frac{\partial \boldsymbol{F}}{\partial t}} = \frac{\partial}{\partial t}\overline{\boldsymbol{F}}, \tag{3.18}$$

where x denotes any spatial coordinate.

The Reynolds decomposition (Eq. 3.11) can be applied then to the induction equation. The magnetic field $\boldsymbol{B}$ and velocity $\boldsymbol{U}$ from Eq. 3.7 are decomposed into their mean and fluctuating parts, so that $\boldsymbol{B} = \overline{\boldsymbol{B}} + \boldsymbol{b}$ and $\boldsymbol{U} = \overline{\boldsymbol{U}} + \boldsymbol{u}$. Taking first the mean component and applying the averaging rules from Equations 3.11–3.16, Equations 3.7 and 3.5 respectively become

$$\frac{\partial \overline{\boldsymbol{B}}}{\partial t} = \boldsymbol{\nabla} \times (\overline{\boldsymbol{U}} \times \overline{\boldsymbol{B}} + \overline{\boldsymbol{\mathcal{E}}}) - \boldsymbol{\nabla} \times \eta(\boldsymbol{\nabla} \times \overline{\boldsymbol{B}}), \tag{3.19}$$

$$\boldsymbol{\nabla} \cdot \overline{\boldsymbol{B}} = 0, \tag{3.20}$$

where $\overline{\boldsymbol{\mathcal{E}}} = \overline{\boldsymbol{u} \times \boldsymbol{b}}$ is the mean electromotive force (EMF). The fluctuating part then becomes

$$\frac{\partial \boldsymbol{b}}{\partial t} = \boldsymbol{\nabla} \times (\overline{\boldsymbol{U}} \times \boldsymbol{b} + \boldsymbol{u} \times \overline{\boldsymbol{B}} + \boldsymbol{G}) - \boldsymbol{\nabla} \times (\eta \boldsymbol{\nabla} \times \boldsymbol{b}), \tag{3.21}$$

where $\boldsymbol{G} = \boldsymbol{u} \times \boldsymbol{b} - \overline{\boldsymbol{u} \times \boldsymbol{b}}$.

The Mean EMF

The mean-field decomposition for the mean field (Eq. 3.19) and the fluctions (Eq. 3.21) introduced two new terms, $\overline{\boldsymbol{\mathcal{E}}}$ and $\boldsymbol{G}$. The EMF is related to the velocity and magnetic field fluctuations, but it is useful to define it in terms of the mean field $\boldsymbol{B}$. The term $\boldsymbol{G}$ can be removed provided the length scales of $\boldsymbol{b}$ and $\boldsymbol{u}$ are much smaller than the length scales of $\overline{\boldsymbol{B}}$ and $\overline{\boldsymbol{U}}$, respectively, as the terms $\boldsymbol{u} \times \boldsymbol{b} - \overline{\boldsymbol{u} \times \boldsymbol{b}}$ will vanish relative to the $\boldsymbol{u} \times \overline{\boldsymbol{B}}$ and $\boldsymbol{U} \times \boldsymbol{b}$ terms in Equation 3.21. In essence, either the Rm should be small or the correlation time of the turbulence τ_c should be less than the eddy turnover time, defined as the Strouhal number,

$$\mathrm{St} = \frac{u_c \tau_c}{\lambda_c}. \tag{3.22}$$

Here, λ_c is the correlation length of the turbulence. This is usually referred to as the first order smoothing approximation (FOSA) or the second order correlation approximation (SOCA) (Krause and Rädler, 1980).

Equation 3.21 is then left with three terms on the right-hand side. A further simplification is made with $\overline{\boldsymbol{U}} = 0$ and the equation for the fluctuation becomes $\partial \boldsymbol{b}/\partial t = \boldsymbol{\nabla} \times (\boldsymbol{u} \times \overline{\boldsymbol{B}} - \eta \boldsymbol{\nabla} \times \boldsymbol{b})$. It becomes apparent from this form that without $\boldsymbol{B}$, $\boldsymbol{b}$ would decay away. Isolating just the induction term and approximating $\partial/\partial t \approx \tau^{-1}$, the fluctuations can be written as

$$\boldsymbol{b} \approx \tau \boldsymbol{\nabla} \times (\boldsymbol{u} \times \overline{\boldsymbol{B}}) = \tau(\overline{\boldsymbol{B}} \cdot \boldsymbol{\nabla})\boldsymbol{u} - \tau(\boldsymbol{u} \cdot \boldsymbol{\nabla})\overline{\boldsymbol{B}}. \tag{3.23}$$

Thus, a linear relationship between $\boldsymbol{b}$ and $\overline{\boldsymbol{B}}$ can be seen and the EMF can then be expressed as a series expansion:

$$\overline{\boldsymbol{\mathcal{E}}}_i = (\overline{\boldsymbol{u} \times \boldsymbol{b}})_i = a_{ij}\overline{B}_j + b_{ijk}\nabla_k \overline{B}_j + \ldots. \tag{3.24}$$

Here, a_{ij} and b_{ijk} are tensors determined solely by the flow, often referred to as turbulent transport coefficients.

The term $\nabla_k \overline{B}_j$ can then be split then into symmetric and antisymmetric parts (Rädler et al., 2003), so that $\boldsymbol{\nabla} \cdot \overline{\boldsymbol{B}} = 1/2[(\nabla_j \overline{B}_i + \nabla_i \overline{B}_j)] - 1/2[\epsilon_{ijk}(\boldsymbol{\nabla} \times \overline{\boldsymbol{B}})_k]$, where ϵ_{ijk} is the Levi-Civita symbol. An expansion of the EMF can then be written as

$$\overline{\boldsymbol{\mathcal{E}}} = -\boldsymbol{\alpha} \cdot \overline{\boldsymbol{B}} - \boldsymbol{\gamma} \times \overline{\boldsymbol{B}} - \boldsymbol{\beta} \cdot (\boldsymbol{\nabla} \times \overline{\boldsymbol{B}}) - \boldsymbol{\delta} \times (\boldsymbol{\nabla} \times \overline{\boldsymbol{B}}) - \boldsymbol{\kappa}(\boldsymbol{\nabla}\overline{\boldsymbol{B}}). \tag{3.25}$$

Here, $\boldsymbol{\alpha}$ is a second rank tensor that denotes the α effect. It is the symmetric portion of the a_{ij} term, so that $\alpha_{ij} = -1/2(a_{ij} + a_{ji)}$. The asymmetric portion of a_{ij} is the $\boldsymbol{\gamma}$ term, a vector quantity connected to the transport of the mean field through turbulent pumping, written as $\gamma_i = 1/2\epsilon_{ijk}a_{jk}$. $\boldsymbol{\beta}$ is a second rank tensor that is the symmetric part of b_{ijk}, tied into the mean field conductivity or diffusivity, written as $\beta_{ij} = 1/4(\epsilon_{ikl}b_{jkl} + \epsilon_{jkl}b_{ikl})$. The $\boldsymbol{\delta}$ term is the corresponding asymmetric portion of b_{ijk}. $\boldsymbol{\delta}$ is also referred to as the $\boldsymbol{\Omega} \times \boldsymbol{J}$ effect, or the Rädler effect (Rädler, 1969) and $\delta_i = 1/4(b_{jji} - b_{jij})$. $\boldsymbol{\kappa}$ is a third rank tensor that encapsulates other effects that are not well-known, and $\kappa_{ijk} = -1/2(b_{ijk} + b_{ikj})$.

If $\boldsymbol{u}$ corresponds to isotropic homogeneous turbulence, then by symmetry arguments $a_{ij} = \alpha\delta_{ij}$, and $b_{ijk} = \beta\epsilon_{ijk}$ where α and β are now scalars, and δ_{ij} is the Kronecker delta. The EMF is then written as

$$\overline{\boldsymbol{\mathcal{E}}} = \alpha\overline{\boldsymbol{B}} - \beta(\boldsymbol{\nabla} \times \overline{\boldsymbol{B}}). \tag{3.26}$$

The β term is the mean turbulent magnetic diffusivity, sometimes denoted by η_t. Inserting this EMF back into Equation 3.19 gives

$$\frac{\partial \overline{\boldsymbol{B}}}{\partial t} = \boldsymbol{\nabla} \times (\overline{\boldsymbol{U}} \times \overline{\boldsymbol{B}}) + (\boldsymbol{\nabla} \times \alpha\overline{\boldsymbol{B}}) - \boldsymbol{\nabla} \times ((\eta + \beta)(\boldsymbol{\nabla} \times \overline{\boldsymbol{B}})). \tag{3.27}$$

The first term on the right hand side of the equation is the information about the large-scale velocity field including differential rotation, the second term is the α effect, and the third term is the diffusion of the magnetic field.

3.1.2 The Poloidal and Toroidal Decomposition

The magnetic field can be decomposed into its poloidal and toroidal components. Using the notation from Chandrasekhar (1961), Appendix III, and following the method outlined in Moss et al. (1991), the magnetic field is decomposed so that $\overline{\boldsymbol{B}} = \boldsymbol{B}_T + \boldsymbol{B}_P$, where T and P denote the toroidal and poloidal parts, respectively. The poloidal field can be written as a function of the magnetic vector potential $\boldsymbol{A}$:

$$\boldsymbol{B}_P = \boldsymbol{\nabla} \times (0, 0, A(r, \theta, t)) = \boldsymbol{\nabla} \times A_\phi, \tag{3.28}$$

and the toroidal field as

$$\boldsymbol{B}_T = (0, 0, B(r, \theta, t)) = B_\phi. \tag{3.29}$$

The mean velocity for a rotating sphere is written as

$$\overline{\boldsymbol{U}} = (0, 0, U_\phi(r, \theta, t)) = \Omega\, r \sin\theta \hat{\boldsymbol{\phi}}, \tag{3.30}$$

where Ω is the angular velocity.

To get the poloidal portion of Equation 3.27, the vector potential is uncurled so that

$$\frac{\partial A_\phi}{\partial t} = \alpha B_\phi - (\eta + \beta)\left(\boldsymbol{\nabla}^2 - \frac{1}{r^2 \sin^2\theta}\right) A_\phi. \tag{3.31}$$

Because the ϕ-component of $\boldsymbol{U} \times (\boldsymbol{\nabla} \times \boldsymbol{A})$ is 0, it can be seen that the Ω effect does not contribute to the regeneration of the poloidal field. The inductive contribution due to the α effect must be larger than the diffusion term for the poloidal field to grow with time. The equation for the toroidal field is

$$\begin{aligned}\frac{\partial B_\phi}{\partial t} = {} & \frac{\partial \Omega}{\partial r}\frac{\partial}{\partial \theta}(A_\phi \sin\theta) - \frac{1}{r}\frac{\partial \Omega}{\partial \theta}(r A_\phi \sin\theta) - \frac{1}{r}\frac{\partial}{\partial r}\left(\alpha \frac{\partial}{\partial r}(r A_\phi)\right) \\ & - \frac{1}{r^2}\frac{\partial}{\partial \theta}\left(\frac{\alpha}{\sin\theta}\frac{\partial}{\partial \theta}(A_\phi \sin\theta)\right) + (\eta + \beta)\left(\boldsymbol{\nabla}^2 - \frac{1}{r^2 \sin^2\theta}\right) B_\phi. \end{aligned} \tag{3.32}$$

Having a gradient to the velocity introduces shear, and the effects can be seen from the above equation where the terms $\partial\Omega/\partial r$ and $\partial\Omega/\partial\theta$ are the radial and latitudinal shear, respectively. For example, a rotation law similar to that of the

Sun could be written as $\Omega = \Omega_0(1 - S\cos^2\theta)$, where S is the normalized shear. The largest source of shear in the Sun is the radial differential rotation present at the base of the convection zone at the tachocline. If a magnetic field has a sufficiently high Rm and there is shear, then a poloidal field will eventually be wound into a toroidal field. The Sun's system is also more complex in that there is a poloidal flow, so the velocity can be decomposed in a similar way as the for the magnetic field so that $\overline{\boldsymbol{U}} = \boldsymbol{U}_P + \boldsymbol{U}_T$. Then

$$\boldsymbol{U}_P = \boldsymbol{\nabla} \times (0, 0, \Psi(r, \theta, t)) = \boldsymbol{\nabla} \times \Psi_\phi, \tag{3.33}$$

and

$$\boldsymbol{U}_T = (0, 0, U(r, \theta, t)) = U_\phi = \Omega\, r \sin\theta \hat{\boldsymbol{\phi}}. \tag{3.34}$$

Here, Ψ_ϕ is the vector potential of the velocity, representing the poloidal flow. An example of a poloidal flow would be the meridional circulation in the Sun, believed to be a contributing factor to the equatorward migration of sunspot belts (e.g., Rädler, 1986; Moss et al., 1995)

The α Effect

Helicity is a factor that quantifies the twisting a flow undergoes, quantifying the amount of twisting and knottedness of flow lines. Kinetic helicity is

$$\mathcal{H}_{\text{kin}} = \overline{\boldsymbol{u} \cdot \boldsymbol{\omega}}, \tag{3.35}$$

where $\boldsymbol{\omega} = \boldsymbol{\nabla} \times \boldsymbol{u}$ is the vorticity. If $\text{Rm} \gg 1$, then the diffusive effects are considered small and the $\boldsymbol{\nabla} \times (\eta \boldsymbol{\nabla} \times \boldsymbol{b})$ term is neglected from Equation 3.21 along with $\boldsymbol{G}$. This leaves $\partial \boldsymbol{b}/\partial t = \boldsymbol{\nabla} \times (\boldsymbol{u} \times \overline{\boldsymbol{B}})$. Then the EMF (Eq 3.26) can be written in terms of the integral of $\partial \boldsymbol{b}/\partial t$ so that

$$\overline{\boldsymbol{\mathcal{E}}} = \overline{\boldsymbol{u} \times \int_0^t \boldsymbol{\nabla} \times (\boldsymbol{u} \times \overline{\boldsymbol{B}}) dt'} \tag{3.36}$$

This integral of the α term becomes (e.g., Moffatt, 1978)

$$\alpha = -\frac{\tau_c}{3} \overline{\boldsymbol{u} \cdot \boldsymbol{\omega}}, \tag{3.37}$$

where τ_c is the correlation time from approximating the integral. Thus α is directly proportional to the kinetic helicity in the simplified isotropic case. The β term is

$$\beta = \frac{\tau_c}{3} \overline{u^2}, \tag{3.38}$$

and is only due to turbulent velocities. A dynamo number C_α is obtained by taking the ratio of the induction term to the diffusivity term in Equation 3.27:

$$C_\alpha = \frac{\boldsymbol{\nabla} \times \alpha \overline{\boldsymbol{B}}}{\boldsymbol{\nabla} \times (\eta + \beta) \boldsymbol{\nabla} \times \overline{\boldsymbol{B}}} \approx \frac{\alpha R}{\eta + \beta}. \tag{3.39}$$

There exists a threshold C_α above which the dynamo field will grow.

The Ω Effect

Stars are rotating objects and as such, the Coriolis force has some impact upon the system. The importance of rotation relative to convection is quantified by the Coriolis number,

$$\mathrm{Co} = \frac{2\Omega_0 L}{U}, \tag{3.40}$$

where Ω_0 is the mean rotation rate. Co is the inverse of the Rossby number discussed in Section 2.2, and both correlate with the observed activity of rotating stars. However, a fast rotation alone does not create the Ω effect, in fact, the opposite effect seems to be observed where differential rotation $\Delta\Omega/\Omega$ decreases as absolute rotation Ω increases in stars (e.g., Henry et al., 1995; Donati et al., 2003a; Barnes et al., 2005; Lehtinen et al., 2016). The rotational effect can be quantified similarly to the α effect as the ratio of the advection term to the diffusion term in Equation 3.27:

$$C_\Omega = \frac{\boldsymbol{\nabla} \times (\overline{\boldsymbol{U}} \times \overline{\boldsymbol{B}})}{\boldsymbol{\nabla} \times (\eta + \beta) \boldsymbol{\nabla} \times \overline{\boldsymbol{B}}} \approx \frac{\Delta\Omega R^3}{\eta + \beta}. \tag{3.41}$$

Here, $\Delta\Omega$ is the shear from differential rotation.

Dynamo Type

From Equations 3.31 and 3.32, it can be seen that the α effect is sufficient to maintain a dynamo on its own. If $\overline{\boldsymbol{U}} = 0$ and $\beta \gg \eta$, then Equation 3.27 reduces to

$$\frac{\partial \overline{\boldsymbol{B}}}{\partial t} = \alpha(\boldsymbol{\nabla} \times \overline{\boldsymbol{B}}) + \beta \boldsymbol{\nabla}^2 \overline{\boldsymbol{B}}. \tag{3.42}$$

Using the Beltrami property, so that $\boldsymbol{\nabla} \times \overline{\boldsymbol{B}} = N\overline{\boldsymbol{B}}$ and $\boldsymbol{\nabla}^2 \overline{\boldsymbol{B}} = -N^2 \overline{\boldsymbol{B}}$, the induction equation becomes

$$\frac{1}{\overline{\boldsymbol{B}}} \frac{\partial \overline{\boldsymbol{B}}}{\partial t} = (\alpha N - \beta N^2). \tag{3.43}$$

Integrating both sides in time gives $\overline{\boldsymbol{B}}(\boldsymbol{r},t) = \overline{\boldsymbol{B}}(\boldsymbol{r},0)\exp[(\alpha N - \beta N^2)t]$. If N is considered to be an approximation of R^{-1}, then the condition for a growing α^2 dynamo is $\alpha > \beta/R$, or $C_\alpha > 1$. Dynamo growth is only possible if the length scale is large and the diffusion small relative to the α effect. The poloidal and toroidal fields are generally the same order of magnitude in α^2 dynamos (Rädler, 1986).

There are conditions whereby a spherical α^2 dynamo may oscillate in the linear case, but only under certain conditions where $\boldsymbol{\alpha}$ changes sign (e.g., Rädler and Braeuer, 1987; Baryshnikova and Shukurov, 1987). An α^2 dynamo may oscillate when the α effect is highly anisotropic, concentrated towards equatorial regions, and/or restricted to thin shells (Rüdiger et al., 2003). The non-linear case is even more complicated, and the non-linear α^2 dynamo is believed to be the predominant dynamo mechanism in rapidly rotating stars with deep convection zones or those that are fully convective, where differential rotation is small and the bottom shear layer is also small or non-existent (Küker and Rüdiger, 1999).

Under certain conditions with the presence of shear, where $C_\Omega \gg C_\alpha$ and $C_\Omega > 1$, the Ω effect and hence rotational shear regenerates the toroidal field at a rate stronger than the α effect can regenerate the poloidal field. This dynamo type is an $\alpha\Omega$ dynamo (Rädler, 1980), the dynamo type thought to operate in the Sun. In such a dynamo, the most easily excitable mode is the $\mathcal{A}0$ configuration. Any values $m > 0$ are found to be the result of a thin shell subsection of the rotating sphere where the α effect dominates over shear locally (Rädler, 1986). Such dynamos typically can oscillate within certain regimes, but non-oscillatory $\alpha\Omega$ dynamos also are possible (e.g., Käpylä et al., 2013a). A dynamo is considered purely $\alpha\Omega$ if the generation of the toroidal field is exclusively due to the Ω effect. The stronger this Ω effect, the more likely an axisymmetric field is preferred. There are also $\alpha^2\Omega$ dynamos, where $C_\alpha \sim C_\Omega$ so that both the shear and the α effect generate a magnetic field.

Here, only the α^2, $\alpha^2\Omega$, and $\alpha\Omega$ dynamos are dealt with. The additional terms of Equation 3.25 may also maintain dynamos under certain conditions. $\boldsymbol{\delta}$ and $\boldsymbol{\beta}$ can maintain a dynamo in conjunction with the Ω effect so that $\delta\Omega$ and $\beta\Omega$ dynamos are also possible (e.g., Rädler, 1980, 1986). These additional terms have many very interesting results for magnetic field symmetry and oscillation, but are outside the scope of this thesis.

3.2 Dynamo Waves

Latitudinal dynamo waves are predicted to propagate along isorotation surfaces of differentially rotating objects such as the Sun or other $\alpha\Omega$ and $\alpha^2\Omega$ dynamos. The direction of propagation is determined by the sign of the shear and α effect (Parker, 1955; Yoshimura, 1975). This is referred to as the Parker-Yoshimura sign rule,

$$\boldsymbol{s} = \alpha \Delta\Omega \times \hat{\boldsymbol{e}}_\phi, \tag{3.44}$$

where α is the alpha effect, $\Delta\Omega$ is the gradient of Ω, and $\hat{\boldsymbol{e}}_\phi$ is the unit vector in the azimuthal direction. This rule can be used to determine whether a dynamo propagates equator-ward (negative value) or pole-ward (positive value). This has been seen in simulations of convection driven $\alpha\Omega$ dynamos (e.g., Warnecke et al., 2014). However, if this rule is applied to the solar rotation law and the observed equator-ward motion of the sunspot belt, a problem develops (Parker, 1987, and references therein). Conventional thought prior to helioseismic observations of the solar rotation profile was that angular momentum conservation and meridional circulation led to a rotation profile that increased downward ($\partial\Omega/\partial r < 0$). Additionally, the α effect was believed to be positive in the northern hemisphere because a convective cell would experience retrograde rotation as it rose and prograde rotation as it sunk, relative to the ambient plasma in the solar convection zone. However, helioseismology finds that the rotation rate actually decreases downward ($\partial\Omega/\partial r > 0$), which means that the Parker-Yoshimura law would require poleward migration of sunspots. Theoretical solutions include using the horizontal gradient of $\partial\Omega/\partial\theta$, limiting dynamo generation to layers where the α effect changes sign, or re-examining the assumptions made when determining the the value of α itself (Leighton, 1969; Parker, 1987).

An azimuthal dynamo wave is also possible (Krause and Rädler, 1980; Rädler, 1986). If the field is decomposed into modes of complex field $\hat{\boldsymbol{B}}$, then these modes can take the form

$$\hat{\boldsymbol{B}} = \mathbf{C} e^{(im\phi + (\lambda - i\Omega_B)\tau)}, \tag{3.45}$$

where $\mathbf{C}$ is a complex axisymmetric steady field that is either symmetric or antisymmetric about the equatorial plane, λ and Ω_B are dimensionless real constants representing the growth rate and angular velocity respectively, and m is the spherical harmonic mode corresponding to the m-term of the real Laplace spherical harmonics Y_l^m. The non-axisymmetric mode rotates like a rigid body with an angular velocity of Ω/m, independent of depth and latitude. Solutions are denoted as critical when $\lambda = 0$, in other words, the dynamo is neither growing nor decaying. Ω_B then is either positive or negative, indicating the direction of the traveling wave as eastward

or westward, respectively. In the case of an α^2 dynamo, the $m = 1$ and $m = 0$ modes were found to have similar marginal values for the critical α to excite the dynamo, and so are almost equally likely to appear (Rädler, 1986), with a preference for $\mathcal{S}1$ and $\mathcal{A}1$ modes within certain regimes. Oscillatory solutions with a tendency towards non-axisymmetry have been found in numerical simulations (e.g., Rüdiger et al., 2003).

3.3 Nonlinearity

The treatment of dynamos outlined here has so far been confined to the linear and kinematic case in the sense that the magnetic field is linearly related to the velocity field only, and the magnetic field changing under its own induction effects is not considered. Non-linearities occure when the the magnetic field reacts back upon the flow and in doing so, affects the rotation gradient and the α effect (Brandenburg and Subramanian, 2005). These can limit the growth so that it saturates. One mechanism is called Ω quenching, where nonlinear effects due to magnetic tension can oppose differential rotation. The current helicity can cause a backreaction on the α effect of a dynamo, and is defined as

$$\mathcal{H}_{\rm curr} = \frac{1}{\mu_0 \rho} \overline{\boldsymbol{j} \cdot \boldsymbol{b}}, \tag{3.46}$$

where μ_0 is the magnetic permeability and $\boldsymbol{j} = \boldsymbol{\nabla} \times \boldsymbol{b}$. The current helicity when combined with the kinetic helicity is

$$\alpha = -\frac{\tau_c}{3} \left(\mathcal{H}_{\rm kin} - \mathcal{H}_{\rm curr} \right), \tag{3.47}$$

(Pouquet et al., 1976). This nonlinear dynamical α quenching is difficult to quantify, and so a simplified way of quantifying α quenching is often presented in mean-field dynamo models as the algebraic formula

$$\alpha = \frac{\alpha_0}{1 + \overline{\boldsymbol{B}}/B_{\rm eq}}. \tag{3.48}$$

Here α_0 is the kinematic value, and $B_{\rm eq} = \sqrt{\mu_0 \rho \overline{\boldsymbol{u}^2}}$ is the equipartition magnetic field. Magnetic buoyancy acts back upon the field so that magnetic flux rises up and out of magnetically active regions, and is therefore removed from the system. Such a mechanism would compete with the γ effect or turbulent pumping, and the ratio with which these two effects work against each other is very difficult to evaluate

in the nonlinear regime (e.g., Rogachevskii and Kleeorin, 2006). These nonlinear mechanisms are difficult, if not impossible to calculate analytically, and so other methods for studying these dynamos are needed.

4 Numerical Models

Numerical simulations are a valuable tool for solving turbulence, particularly in astrophysical objects. The conditions of the solar convection zone, for example, are impossible at the present to reproduce in a laboratory setting with the extreme Re, temperatures, densities, and pressures found in the Solar convection zone. Turbulence itself is also very complex, with eddies and cyclones forming and interacting on all scales in non-linear ways that make it impossible to treat analytically without major simplifications. Numerical simulations allow the study of turbulence and certain resulting phenomena, within computational limits.

4.1 Simulating Convective Turbulence

Modeling convection with simulations involves solving the Navier-Stokes equations numerically. One approach is called direct numerical simulation, or DNS. Because DNS resolves the turbulence directly instead of using a turbulence model, there exists a computational limit to the spatial and temporal scales. The spatial scale is the Kolmogorov scale (Kolmogorov, 1941a,b),

$$L_K = \left(\frac{\nu^3}{\epsilon}\right)^{1/4}, \tag{4.1}$$

where ν is the kinematic viscosity and ϵ is the energy dissipation rate. The kinematic viscosity can be defined in terms of the Reynolds number, so that $\nu = U_{\rm rms}L/{\rm Re}$. The energy dissipation can be approximated as the ratio of kinetic energy over the timescales, so that $\epsilon \approx U_{\rm rms}^2/(L/U_{\rm rms}) = U_{\rm rms}^3/L$. From Equation 4.1, it can be seen that the minimum length scale L relative to the Kolmogorov scale is related to the Reynolds number by a power law,

$$\frac{L}{L_K} \propto {\rm Re}^{3/4}. \tag{4.2}$$

Thus the larger Re, the larger the number of gridpoints needed in a 3D simulation, which would scale as $N^3 = ({\rm Re}^{3/4})^3$.

The temporal scale is limited by the discrete time increment Δt, determined by the Courant number,

$$C < \frac{U_{\rm rms}\Delta t}{\Delta x}. \tag{4.3}$$

Here, Δx is the discrete distance between the mesh points for the grid. The Courant number determines the stability of the numerical scheme and must be smaller than a certain number that depends on the system that is studied. Typically $C < 1$ but it can also be larger in some cases. The Courant criterion ensures that information has enough time to propagate a distance equal to the grid spacing within the length of the time step. Given that the simulation must encompass L, the total simulation size in one direction should be $N\Delta x > L$, where N is the number of mesh points in the selected direction.

A method that circumvents the higher computation requirements of DNS by averaging while retaining detailed information about the eddies on the scales of interest is called large eddy simulations, hereafter LES. This method utilizes low pass filtering of the continuity equation, the Navier-Stokes equation, and any other required equations to capture the phenomena of interest. This is a method initially proposed by Smagorinsky (1963). LES is useful when the information at the smallest scales is not relevant to the results and computational requirements are reduced by averaging over small portions of time and/or space. The large-scale eddies are directly solved only down to a selected scale, below which a turbulence model is used.

The choice in numerical modeling methods depends on the temporal and spatial scales of phenomena that are present in the simulated turbulent flow (e.g., Pope, 2004; Piomelli, 2014). When the range of scales is large with well-defined separation, the most computationally inexpensive method is to use the mean-field method. This approach solves only the for the evolution of large-scale quantities as the small-scale quantities are parameterized similarly to LES. The mean-field method is presented in Section 3.1.1, and it has been used in studies of solar dynamos, ranging from solving only the induction equation (e.g., Moss et al., 1991) to models involving the full thermodynamics (Brandenburg et al., 1992). This method is limited as unknown turbulent quantities may operate on a smaller-scale. Different parameter combinations create very different physical settings that may still show properties similar to the solar cycle (e.g., Kuzanyan et al., 2006; Guerrero and de Gouveia Dal Pino, 2009). Determining the transport coefficients requires the use of DNS or the test-field method where additional linear equations are used to describe the response of the system to prescribed test fields (e.g., Schrinner et al., 2005; Rheinhardt and Brandenburg, 2010). Relevant parameter combinations can then be used in the mean-field method. In some cases, such as the numerical models of this work, the

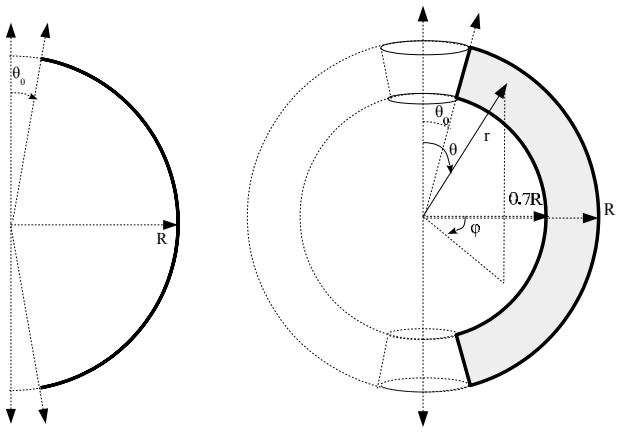

Figure 4.1: *Left:* Geometry of the 1D model used for mean-field models. *Right:* Geometry of the 3D spherical wedge used for DNS models.

numerical stability and/or physical feasibility of the model requires sub-grid scale effects to be included as a hybrid of LES and DNS.

4.2 The Models

One of the goals of this thesis is to understand turbulence in the context of convection zones of stars. Simulations are used to study the mechanisms that contribute to the growth of the dynamo in the solar or stellar convection zone. Numerical simulations allow the isolation of mechanisms of interest such as differential rotation, stratification, diffusivity, and helicity. Of particular interest is the details of the symmetry and oscillations of a resulting dynamo to make comparisons with observations of the Sun and stars.

4.2.1 1D Mean-field Dynamo Model

The model used in Paper III (Cole et al., 2016) is 1D, solving the equations in the latitudinal direction in spherical coordinates (r, θ, ϕ), with radius r, colatitude θ, and azimuth ϕ. The colatitude is used because the angle of interest is the angle from pole, so that $\tilde{\theta} = 90^\circ - \theta$ where $\tilde{\theta}$ is the latitude. Hence, the colatitude is 0° at the North pole and 180° at the South pole. The model is linear and the latitudinal

extent includes both hemispheres so that the resulting parity $\mathcal{P}$ of the dynamo can also be studied (Fig. 4.1, left). The model is axisymmetric, so higher m modes are not possible and $\mathcal{M} = 0$. Equations 3.19 and 3.20 are used, so that

$$\frac{\partial \overline{\boldsymbol{B}}}{\partial t} = \boldsymbol{\nabla} \times (\overline{\boldsymbol{U}} \times \overline{\boldsymbol{B}} \times \overline{\boldsymbol{\mathcal{E}}} - \eta \mu_0 \overline{\boldsymbol{J}}), \tag{4.4}$$

$$\boldsymbol{\nabla} \cdot \overline{\boldsymbol{B}} = 0, \tag{4.5}$$

where η is the non-turbulent diffusivity. A simple isotropic α effect and a scalar β are assumed, neglecting the $\boldsymbol{\delta}$, $\boldsymbol{\gamma}$, and $\boldsymbol{\kappa}$ terms from Equation 3.25. The EMF is then expressed as $\overline{\boldsymbol{\mathcal{E}}} = \alpha \overline{\boldsymbol{B}} - \eta_\mathrm{t} \mu_0 \overline{\boldsymbol{J}}$, where η_t is the turbulent magnetic diffusivity, previously denoted as β. The resulting mean magnetic field is only a function of t and θ, $\overline{\boldsymbol{B}} = \overline{\boldsymbol{B}}(\theta, t)$. The selected angular velocity profile is $\overline{\boldsymbol{U}} = r \sin\theta \Omega \hat{\phi}$, where Ω is the angular velocity, so that $\Omega(r, \theta) = rS(\theta)$, where S is the shear.

The induction equation (Eq. 4.4) is written in terms of the magnetic vector potential $\boldsymbol{A}$, related to the magnetic field via $\boldsymbol{B} = \boldsymbol{\nabla} \times \boldsymbol{A}$. To uncurl Equation 4.4, the advective gauge is used (e.g., Candelaresi et al., 2011), so that

$$\frac{\partial \overline{\boldsymbol{A}}}{\partial t} = -r \sin\theta \overline{A}_\phi \boldsymbol{\nabla}\Omega + \overline{\boldsymbol{\mathcal{E}}} - \eta \mu_0 \overline{\boldsymbol{J}}, \tag{4.6}$$

where $\boldsymbol{\nabla}\Omega = (S, \partial_\theta S, 0)$. The mean current $\overline{\boldsymbol{J}}$ is then

$$\overline{\boldsymbol{J}} = \frac{1}{\mu_0 R^2}(D_\theta \overline{\boldsymbol{A}}_\theta - D_\theta \partial_\theta \overline{\boldsymbol{A}}_r, \partial_\theta \overline{\boldsymbol{A}}_r, -\partial_\theta D_\theta \overline{\boldsymbol{A}}_\phi), \tag{4.7}$$

where D_θ is a modified derivative, $\cot\theta + \partial_\theta$. Without the shear term, the dynamo type is α^2. If there is a shear term, and shear is comparable to the α effect or dominates as the dynamo mechanism over the α effect, then the dynamo type is $\alpha^2\Omega$ or $\alpha\Omega$. The study of the dynamo type $\alpha^2\Omega$ requires an additional term to Equation 4.6 so that the radial derivatives are accounted for to include shear, introducing the Ω effect. If the radial derivatives are removed, an artifact occurs where the excited $\alpha\Omega$ dynamo is no longer oscillatory (Jennings et al., 1990). This artifact can be removed with the addition of a damping term $-\mu^2 \overline{\boldsymbol{A}}$, obtained from averaging the equations of magnetic mean-field generation in a thin convective shell with respect to r (Moss et al., 2004). Thus the two dynamo numbers relevant for quantifying the α effect and shear are, respectively,

$$C_\alpha = \alpha_0 R / \eta_{\mathrm{t}0}, \tag{4.8}$$

Table 4.1: Boundary conditions for the 1D dynamo model.

Type	Boundary Condition ($\theta = \pm\theta_0$)	Abbreviation
Regularity at the pole	$\partial_\theta \overline{A}_r = \overline{A}_\theta = \overline{A}_\phi = 0$	SAA
Perfect conductor	$\overline{A}_r = \partial_\theta \overline{A}_\theta = \overline{A}_\phi = 0$	ASA
Normal field	$\partial_\theta \overline{A}_r = \overline{A}_\theta = \partial_\theta \overline{A}_\phi = 0$	SAS

and

$$C_\Omega = S_0 R^2 / \eta_{\mathrm{t}0}. \tag{4.9}$$

Here, $\eta_{\mathrm{t}0}$ is the amplitude of magnetic diffusivity and $S_0 = S(\theta)$ is a constant. C_α and C_Ω are control parameters with α_0, $\eta_{\mathrm{t}0}$, and S_0 as inputs. The critical C_α, such that the dynamo is marginally excited and neither decays nor grows, is denoted as $C_\alpha^\star$. The parameters C_α and C_Ω dictate regimes where certain dynamo types are excited, of type $\mathcal{A}m$ or $\mathcal{S}m$ (see Table 3.1). The model explores both the $\mathcal{A}0$ and $\mathcal{S}0$ regimes both with $\theta_0 = 0^\circ$ and the SAA boundary condition, and $\theta_0 = 1^\circ$ with the ASA boundary condition to determine if the additional shear term results in artifacts.

The dynamo is seeded by a low-amplitude Gaussian noise magnetic field. The model is selected to test the α^2 and $\alpha^2\Omega$ dynamo types with respect to chosen boundary conditions to determine if the transition as $\theta_0 \to 0^\circ$ results in any significant changes in the resulting dynamo. The motivation for such an examination is based on previous results of convective wedges in spherical coordinates (e.g., Käpylä et al., 2011a, 2012, and Papers I and II of this thesis) where the boundary condition choice was thought to possibly have an impact on the final solutions. Thus it would be useful to determine the effect the boundary conditions have on the final symmetry and oscillations of solutions.

The different boundary condition possibilities are listed in Table 4.1. The abbreviations represent each component of $\overline{\boldsymbol{A}}$ as symmetric (S) or antisymmetric (A) with respect to the equator. If the component of $\overline{\boldsymbol{A}}$ is symmetric, the derivative ∂_θ of the component vanishes, and if the component is antisymmetric, then the component of $\overline{\boldsymbol{A}}$ vanishes. Two of these are of particular interest, the SAA and ASA boundary conditions. The ASA boundary condition is similar to the latitudinal boundary condition imposed on the models used in Papers I and II. Ideally, the simulation could be extended to the poles and the SAA boundary condition used instead, but Δx from Equation 4.3 would become prohibitively small in the azimuthal direction, preventing this simple approach.

The model allows the imposition of different α and η_t profiles to find possible parameter regimes where not extending to the poles has minimal effects on the resulting dynamo. In other words, an oscillatory field with equatorward migration should not be unique to the ASA boundary condition when $\theta > 0°$. Astrophysical bodies such as stars undergo rotation while having a global magnetic field, and so the η_t profile is motivated by the theoretical results of Kitchatinov et al. (1994), where the diffusivity is thought to be weaker in polar regions. A weak increase of η_t towards the equator was also observed in numerical simulations by Käpylä et al. (2009). Motivation for the α profile is both from direct observation of the concentration of the magnetic field at lower latitudes in the Sun, as well as results from numerical simulations where the α effect was found to decrease near the poles (Ossendrijver et al., 2002; Käpylä et al., 2006, 2009). The profiles are modified so that they are proportional to sinusoidal functions to the nth power that impose regularity at the poles, in agreement with the SAA boundary condition. The expansion is as follows for α and η_t respectively,

$$\alpha = \alpha_0 \cos\theta(a_0 + a_2 \sin^2\theta + \cdots + a_n \sin^n\theta), \tag{4.10}$$

and

$$\eta_t = \eta_{t0}(e_0 + e_2 \sin^2\theta + \cdots + e_n \sin^n\theta), \tag{4.11}$$

where a_i and e_i are 1 when $i = n$ and 0 otherwise. α and η_t are both scalar control parameters selected for the models varying only in the latitudinal direction, so that the regime is limited to linear dynamos, and thus the resulting parity can only be $\mathcal{P} = \pm 1$ (Brandenburg et al., 1989).

4.2.2 3D Semi-Global Wedge Models

The model used in Papers I (Käpylä et al., 2013b) and II (Cole et al., 2014) is a wedge in a 3D spherical coordinate system (r, θ, ϕ). This wedge (Fig. 4.1, right) is thought to represent the solar convection zone, and extends radially from $r_0 = 0.7R < r < R$ where R is the radius of the star. Due to limitations in 3D that prevent the full sphere from being modeled with the code, the simulation has a limited latitudinal extent in the θ-direction, so that $\pi/12 \leq \theta \leq 11\pi/12$, where θ is the colatitude. While this prevents the time step from becoming prohibitively small, any cross-polar effects are lost. The azimuthal extent ϕ can be varied as the boundary condition in this direction is periodic.

The Conservation Equations

In order to further describe the system, some additional conservation laws are required. The continuity equation is applied so that mass, momentum, and energy are

all conserved by the system. The advective derivate is used, so that

$$\frac{D}{Dt} \equiv \frac{\partial}{\partial t} + \boldsymbol{U} \cdot \boldsymbol{\nabla}. \tag{4.12}$$

The conservation of mass equation is

$$\frac{D \ln \rho}{Dt} = -\boldsymbol{\nabla} \cdot \boldsymbol{U}, \tag{4.13}$$

where ρ is the density and $\boldsymbol{U}$ is the flow velocity. Conservation of momentum is expressed as the Navier-Stokes equation, giving

$$\rho \left(\frac{D\boldsymbol{U}}{Dt} \right) = -\boldsymbol{\nabla} p + \boldsymbol{J} \times \boldsymbol{B} + \boldsymbol{F}_{\text{visc}} + \boldsymbol{f}, \tag{4.14}$$

where p is the pressure, $\boldsymbol{J} \times \boldsymbol{B}$ is the Lorentz force, $\boldsymbol{F}_{\text{visc}}$ is the viscous force, and $\boldsymbol{f}$ encapsulates all other forces. The conservation of energy can be written as

$$\rho T \frac{Ds}{Dt} = -\boldsymbol{\nabla} \cdot (\boldsymbol{F}^{\text{HF}}) + \mu_0 \eta \boldsymbol{J} + 2\rho\nu \mathbf{S}^2, \tag{4.15}$$

where T is the temperature, s is the specific entropy, $\boldsymbol{F}^{\text{HF}}$ is the heat flux, ν is kinematic viscosity, $\mu_0 \eta \boldsymbol{J}$ is the Ohmic heating, and $\mathbf{S}$ is the rate of strain tensor.

The model is a spherical rotating shell of thickness $0.3R$, therefore the $\boldsymbol{f}$ term in Equation 4.14 specifically encompasses the Coriolis force and gravitational force, so that $\boldsymbol{f} = -g\hat{\boldsymbol{r}} - 2\rho\boldsymbol{\Omega}_0 \times \boldsymbol{U}$, where $g = GM/r^2$ is the gravitational acceleration. G is the gravitational constant, M is the mass of the star below the convection zone, $\hat{\boldsymbol{r}}$ is the unit vector in the radial direction, r is the radius, and $\boldsymbol{\Omega}_0 = (\cos\theta, -\sin\theta, 0)\Omega_0$ is the rotation vector with respect to the time-independent rotation rate of the frame Ω_0. The viscous force is determined by the rate of strain, $\boldsymbol{F}_{\text{visc}} = \boldsymbol{\nabla} \cdot 2\nu\rho\mathbf{S}$. The rate of strain tensor $\mathbf{S}$ is the symmetric component of the gradient matrix of the flow. In a spherical coordinate system and following the transformation and notation of Mitra et al. (2009) (Appendix B), where a semi-colon denotes covarient differentiation, this tensor is written as

$$\mathbf{S}_{ij} = \frac{1}{2}\left(U_{i;j} + U_{j;i}\right) - \frac{1}{3}\delta_{ij}\boldsymbol{\nabla} \cdot \boldsymbol{U}. \tag{4.16}$$

Equation 4.15 contains a generic term for the heat flux, $\boldsymbol{F}^{\text{HF}}$, which encompasses the sub-grid scale heat flux $\boldsymbol{F}^{\text{SGS}}$ and the radiative heat flux $\boldsymbol{F}^{\text{rad}}$. Thus the model employs a hybrid of LES and DNS. The radiative heat flux portion can be written as $\boldsymbol{F}^{\text{rad}} = -K\boldsymbol{\nabla}T$, where K is the radiative heat conductivity. The SGS portion of

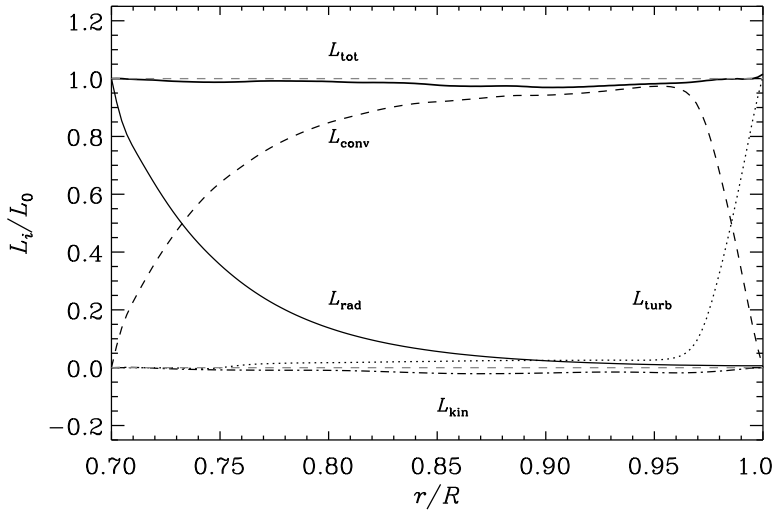

Figure 4.2: Contributions of the various fluxes in terms of luminosities as a function of radius. $L_{\rm tot}$ is the total luminosity, indicated by by a thick, solid line. $L_{\rm conv}$ is from the convective flux, $L_{\rm rad}$ is from the radiative flux, $L_{\rm turb}$ is from the unresolved turbulent heat flux, and $L_{\rm kin}$ is from the kinetic flux (Paper I).

the heat flux is written as $\boldsymbol{F}^{\rm SGS} = -\chi_{\rm SGS}\rho T\boldsymbol{\nabla} s$, where $\chi_{\rm SGS}$ is the turbulent heat conductivity. Through this term, an unresolved portion of the turbulent heat flux is added, which is strongest near the surface. This quantity is shown in Figure 4.2 in the form of luminosity, $L_{\rm turb}$, where luminosity is related to the fluxes by $L \propto r^2 F$. It is evident from the figure that this flux has a negligible contribution in the bulk of the convection zone, and becomes active only near the surface. Without this additional flux to compensate for the drop in convective flux, total luminosity out of the system would be much less than the total luminosity put into the system.

Boundary and Initial Conditions

Boundary conditions are imposed in r and θ so that the boundaries are impenetrable and stress-free, giving

$$U_r = 0, \quad \frac{\partial U_\theta}{\partial r} = \frac{U_\theta}{r}, \quad \frac{\partial U_\phi}{\partial r} = \frac{U_\phi}{r}, \quad (r = r_0, R) \tag{4.17}$$

and

$$\frac{\partial U_r}{\partial \theta} = 0, \quad U_\theta = 0, \quad \frac{\partial U_\phi}{\partial \theta} = U_\phi \cos\theta, \quad (\theta = \theta_0, \pi - \theta_0). \tag{4.18}$$

The lower radial boundary and the latitudinal boundaries are perfect conductors with respect to the magnetic field so that

$$\frac{\partial A_r}{\partial r} = A_\theta = A_\phi = 0, \quad (r = r_0), \tag{4.19}$$

and

$$A_r = \frac{\partial A_\theta}{\partial \theta} = A_\phi = 0, \quad (\theta = \theta_0, \pi - \theta_0), \tag{4.20}$$

where $\theta_0 = \pi/12$. The validity of the perfect conductor boundary condition and the effect on the resulting dynamo is discussed in Paper III. At the outer radial boundary,

$$A_r = 0, \quad \frac{\partial A_\theta}{\partial r} = -\frac{A_\theta}{r}, \quad \frac{\partial A_\phi}{\partial r} = -\frac{A_\phi}{r}, \quad (r = R). \tag{4.21}$$

The initial state of the system is isentropic. The hydrostatic temperature gradient is fixed at the lower boundary, and written as

$$\frac{\partial T}{\partial r} = -\frac{g}{c_V(\gamma - 1)(n_{\rm ad} + 1)}. \tag{4.22}$$

An ideal gas is assumed, so that ratio of specific heats is $\gamma = 5/3 = c_P/c_V$. The specific internal energy is $e = c_V T$ so that $p = (\gamma - 1)\rho e$. The polytropic index $n_{\rm ad} = 1.5$ is that of adiabatic stratification. The hydrostatic gradient is fixed at $r = r_0$, so that the system has an imposed flux of $\boldsymbol{F}_b = -K(\partial T/\partial r)|_{r=r_0}$. Thus the process that provides the heat flux at the bottom of the convection zone is radiative diffusion (Fig. 4.2). On the outer boundary, the blackbody condition is used, so that

$$\sigma T^4 = -K\frac{\partial T}{\partial r} - \rho T \chi_{\rm SGS}\frac{\partial s}{\partial r}. \tag{4.23}$$

Here, σ is the Stefen-Boltzmann constant, selected to be such that in the initial state the flux σT^4 carries the total luminosity through the surface.

The radiative heat conductivity has an imposed profile based on depth, so that $K = K_0(n + 1)$, where the polytropic index n varies radially so that $n = 2.5(r/r_0)^{-15} - 1$ where $n = n_{\rm ad}$ at $r = r_0$, and K is a small fraction of K_0 at the upper boundary. K_0 is

$$K_0 = \frac{\mathcal{L}}{4\pi} c_V(\gamma - 1)(n_{\rm ad} + 1)\rho_0\sqrt{GMR}, \tag{4.24}$$

where $\mathcal{L}$ is the luminosity parameter defined in the following subsection. The turbulent heat conductivity is an imposed piecewise profile, where $\overline{\chi}_{\rm SGS}$ is the value of $\chi_{\rm SGS}$ in the middle of the convection zone at $r_m = 0.85R$. This profile is made so that $\chi_{\rm SGS} \to 0$ where $r \leq 0.75R$, $\chi_{\rm SGS} = \overline{\chi}_{\rm SGS}$ where $0.75R < r < 0.98R$, and is $12.5\overline{\chi}_{\rm SGS}$ where $r \geq 0.98R$ (Fig. 4.2). To keep the effects small from $\chi_{\rm SGS}$ on the total entropy of the system, the smallest possible value is chosen that maintains numerical stability.

Non-dimensional Parameters

Much of the work in this thesis employs dimensionless parameters, a necessity due to the capacity of computers to store numbers but not units. Thus, a basis for for this non-dimensional unit system must be established. Papers I, II, and III employ a unit system as follows:

$$R = GM = \rho_0 = c_P = \mu_0 = 1, \tag{4.25}$$

where R is the total radius, G is the gravitational constant, M is the total mass of the system, ρ_0 is initial density, c_P is the specific heat at constant pressure, and μ_0 is the magnetic permeability of free space.

Quantities of interest can be transformed back into physical units using Equation 4.25. It is then possible to choose a normalization that works best. For this thesis, solar values are used because the setup is modeled after the Sun. This is, of course, not the only possible normalization choice for these non-dimensional parameters. Transforming back into units of length, time, velocity, density, entropy, and the magnetic field uses the following conversions:

$$\begin{aligned} [x] = R, \quad [t] = \sqrt{R^3/GM}, \quad [U] = \sqrt{GM/R}, \\ [\rho] = \rho_0, \quad [s] = c_P, \quad [B] = \sqrt{\rho_0 \mu_0 GM/R}. \end{aligned} \tag{4.26}$$

This system of units allows a more meaningful expression of results with time units in terms of convective turnover times (the time for one large eddy to completely circulate), and can convert easily into either SI or cgs units.

Certain dimensionless quantities are valuable for describing the properties of dynamos by conveying meaningful information with the ratios of certain parameters of interest. Control parameters include the initial angular velocity Ω_0, the viscous diffusivity ν, the thermal diffusivity χ, the magnetic diffusivity η, the constant luminosity L_0, and the initial density ρ_0. These are related to each other via non-dimensional parameters.

If discussing the strength of the rotating inertial forces relative to the viscous force, then the Taylor number is used:

$$\mathrm{Ta} = \left(\frac{2\Omega_0 R^2}{\nu}\right)^2. \tag{4.27}$$

The relation between viscous diffusivity and the thermal diffusivity is the Prandtl number,

$$\mathrm{Pr} = \frac{\nu}{\chi_\mathrm{m}}, \tag{4.28}$$

where $\chi_\mathrm{m} = K/c_P\rho_\mathrm{m}$ and the subscript 'm' denotes the value at $r = r_\mathrm{m}$. The Prandtl number can be used to quantify how much convection and conduction transfer energy relative to each other. The magnetic Prandtl number is

$$\mathrm{Pr}_M = \frac{\nu}{\eta}. \tag{4.29}$$

Pr_M is high when diffusion is largely through viscous forces and low when diffusion is through magnetic forces. Other important quantities relevant to astrophysics include the luminosity parameter mentioned in Equation 4.24,

$$\mathcal{L} = L_0 \frac{1}{\rho_0 (GM)^{3/2} R^{1/2}}, \tag{4.30}$$

where L_0 is the constant luminosity. Nondimensional viscosity is

$$\tilde{\nu} = \frac{\nu}{\sqrt{GMR}} \tag{4.31}$$

and the nondimensional Boltzman constant is

$$\tilde{\sigma} = \frac{\sigma R^2 T_0^4}{L_0}, \tag{4.32}$$

where T_0 is the temperature at the base of the convection zone.

Output parameters are measured when the dynamo saturates. One of the outputted quantities is the typical velocity, defined as

$$U_\mathrm{rms} = \sqrt{\frac{3}{2}\left\langle U_r^2 + U_\theta^2 \right\rangle_{r\theta\phi t}}. \tag{4.33}$$

The factor 3/2 accounts for neglecting the U_ϕ term, which is left out as the total velocity would otherwise be dominated by differential rotation. Specific to the model,

Re, Rm, and Co (Eqns. 3.1, 3.8, and 3.40) are defined in terms of $U_{\rm rms}$ and the estimated wavenumber of the largest eddies $k_f = 2\pi/\Delta r \approx 21R^{-1}$, where $\Delta r = 0.3R$ is the thickness of the convection zone. The Reynolds number with respect to these quantities becomes $\mathrm{Re} = U_{\rm rms}/\nu k_f$, the magnetic Reynolds number is $\mathrm{Rm} = U_{\rm rms}/\eta k_f$, and the Coriolis number is $\mathrm{Co} = 2\Omega_0/U_{\rm rms}k_f$. The wave number with respect to rotation is $k_\omega = \omega_{\rm rms}/U_{\rm rms}$, where $\omega_{\rm rms}$ is volume averaged root-mean-squared value of $\boldsymbol{\omega} = \boldsymbol{\nabla} \times \boldsymbol{U}$.

The normalized pressure scale height is

$$\xi = \frac{(\gamma - 1)c_V T_1}{GM/R}. \tag{4.34}$$

Hydrostatic equilibrium then defines the density stratification via

$$\Gamma_\rho \equiv \frac{\rho_{r_0}}{\rho_R}, \tag{4.35}$$

where ρ_{r_0} and ρ_R are the density at the bottom and top of the convection zone, respectively. The initial density stratification is a control parameter denoted as $\Gamma_\rho^{(0)}$, but as the dynamo saturates, the density stratification can change slightly from this initial value and so $\Gamma_\rho^{(0)}$ is an input parameter and Γ_ρ is an output diagnostic.

The number that quantifies whether a buoyancy-driven flow transfers heat through conduction or convection is the Rayleigh number,

$$\mathrm{Ra} = \frac{GM(\Delta r)^4}{\nu \overline{\chi}_{\rm SGS} R^2} \left(-\frac{1}{c_P}\frac{ds}{dr} \right)_{r_{\rm m}}. \tag{4.36}$$

If Ra is above some critical number, heat is primarily transferred through convection. Results for the magnetic field are usually normalized to the equipartition field,

$$B_{\rm eq} = \sqrt{\langle \mu_0 \rho \boldsymbol{U}^2 \rangle}_{\theta\phi t}. \tag{4.37}$$

This quantity is used to normalize quantities of interest of the magnetic field over time. For example, the changes in the azimuthal field $\overline{\boldsymbol{B}}_\phi$ over time versus latitude normalized with this value create a kind of butterfly diagrams analogous to those created for the Sun.

Comparison to the Sun

Because the simulation has a solar-sized convection zone, it is helpful to put the values in the context of solar values and compare where the simulation differs from

Table 4.2: Solar values for selected parameters.

Parameter	Value	CGS Units
$R_\odot$	$7.0 \cdot 10^{10}$	cm
$L_\odot$	$3.9 \cdot 10^{33}$	g cm^2 s^{-3}
$GM_\odot$	$1.34 \cdot 10^{26}$	cm^2 s^{-2}
$\Omega_{0\odot}$	$3 \cdot 10^{-6}$	s^{-1}
$M_{c\odot}$	$6 \cdot 10^{31}$	g
$\nu_{t\odot}$	$5 \cdot 10^{12}$	cm^2 s^{-1}
$\eta_{t\odot}$	$5 \cdot 10^{12}$	cm^2 s^{-1}
$\chi_{t\odot}$	$1.5 \cdot 10^{13}$	cm^2 s^{-1}

reality. Solar values for various parameters estimated by Brandenburg et al. (1992) are shown in Table 4.2, where $M_{c\odot}$ denotes the estimated mass of the solar convection zone.

The Ra possible for the numerical simulation is limited by the diffusivity, and thus the numbers possible in simulations are much smaller than in the Sun. There is a difference of typical values used in simulations of 10^6 to the real solar values of 10^{24}. Accordingly, the Mach numbers and and fluxes of the numerical simulations are higher than those found in the Sun. In order to have realistic Coriolis numbers in the simulations, the angular velocity Ω_0 must be increased by 1/3 of the power that the flux is increased. The centrifugal acceleration is omitted because it would be unrealistically large (Käpylä et al., 2011b). A realistic Co should not disrupt the hydrostatic balance from gravity and centrifugal forces.

Solar luminosity is not possible, as it requires a prohibitive time step constraint. The luminosity of the model can be written as $L = 4\pi r_0^2 F_0$, where F_0 is the total flux at $r = r_0$. The acoustic timescale is the only timescale that matches that of the Sun. The convective, thermal, resistive, and viscous timescales all depend on the pressure scale height $H_{\rm P0}$ at $r = r_0$. These timescales together are

$$\tau_{\rm ac} = \sqrt{R^2/GM}, \tag{4.38}$$

$$\tau_{\rm conv} = H_{\rm P0}/U_{\rm rms}^{\rm (ref)}, \tag{4.39}$$

$$\tau_{\rm th} = H_{\rm P0}^2/\chi_0, \tag{4.40}$$

$$\tau_{\rm res} = H_{\rm P0}^2/\eta, \tag{4.41}$$

$$\tau_{\rm visc} = H_{\rm P0}^2/\nu, \tag{4.42}$$

where $U_{\rm rms}^{\rm (ref)}$ is related to the luminosity by $U_{\rm rms}^{\rm (ref)} = (F_0/\rho_0)^{1/3}$. Thus, while $\tau_{\rm ac}$ can be identical to that of the Sun, the convective timescale should be made smaller by

a factor of 70–100, while the thermal and resistive timescales reduced by a factor of 10^7, and the viscous timescale even more so by a factor of 10^{14}. The higher $\mathcal{L}$ required corresponds to the aforementioned Ra $\sim 10^6$. The limits on $\tau_{\rm res}$ and $\tau_{\rm visc}$ result in correspondingly smaller Rm and Re than that found in the Sun. Pr and Pr_M are by similar arguments larger than in the Sun.

4.3 The Pencil Code

The Pencil Code is used for numerical simulations in Papers I, II, and III. Development for the Pencil Code [1] started at the Turbulence Summer School of the Helmholtz Institute in Potsdam in 2001. The code solves the compressible magnetohydrodynamic equations and is a sixth order in space and third order in time finite-difference code. The MHD equations were described previously in more detail in Section 3.1. The code allows for a high level of variation as to what physical processes are included in modeling a turbulent flow by the selection of modules to include, such as gravity, magnetic effects, mean-field approximations. The spherical coordinate system implemented in the code is that described by Mitra et al. (2009). Additionally, the code is open-source to allow user-end modifications and can be used both with single processor and multi-processor systems with message passing interface. The code is also independent of the unit system, as described in Section 4.2.2, so that results can be converted into any relevant unit system. The code is non-conservative which means that the conservation equations (Eqns. 4.13–4.15) are discretized on the numerical grid in a way that the conservation of them is not guaranteed up to the machine precision, but to the discretization error of the finite-difference scheme. This is why the time evolution of all quantities that should be conserved need to be monitored. The name of the code is derived from the cache-efficient solving of equations in the x-direction, called a "pencil". The Pencil Code employs the use of the magnetic vector potential $\boldsymbol{A}$ to keep the magnetic field intrinsically divergence-free.

[1] https://github.com/pencil-code/

5 Time Series Analysis

5.1 Observation Methods of Solar-Type Stars with Spot Activity

The following methods are specifically the ones used in Papers IV, V, and VI, but certainly do not encompass all methods of observing stellar spot activity.

5.1.1 The Three Stage Period Analysis Method

Long term variable activity of a star can be studied through time-series analysis of photometry. Information regarding short-term cycles, active longitudes, and longer cycles can be ascertained through statistical methods analyzing the light curve of the star over several decades. Long-term activity cycles, analogous to the 11-year cycle in the Sun, would be evident in changes over several years of the mean brightness and/or light curve amplitude. Spots may also exhibit a tendency to form at specific longitudes. The aim of using time-series analysis is to calculate the rotation period P, the mean of the light curve M, the amplitude A, and minimum epochs $t_{\min}$.

The Three Stage Period Analysis (hereafter TSPA) is a statistical method that seeks the best possible parameters in three steps. The pilot search gives an estimate of the non-linear parameters and searches discrete values of the frequency $f = 1/P$ where P is the rotation period. The grid search uses the frequency candidates from the pilot search and refines the parameters further by using a denser grid around these values for f_{pilot}. The final step is a refined search that computes parameters using a standard Marquardt iteration to high precision with f as a free parameter, using the grid search results as starting points. TSPA also includes the use of weights so that errors in the data set are accounted for in the final solution. This method is described in detail in Jetsu and Pelt (1999). Included here is the relevant information for understanding the Continuous Period Search method (hereafter CPS) used in Paper IV, described in Subsection 5.1.2.

Each observation y occurs at time t_i for a total of n observations. For each $y(t_i)$,

there is the corresponding error $\pm\sigma_i$. The model is some function $g(t, \bar{\beta})$, where $\bar{\beta}$ is the set of parameters. The solution seeks to minimize the residual sum squared (RSS):

$$\mathrm{RSS} = \sum_{\mathrm{i=1}}^{\mathrm{n}} (\mathrm{y(t_i)} - \mathrm{g(t, \bar{\beta})})^2. \tag{5.1}$$

The frequency f is a free non-linear parameter, so a model as a function of frequency could be

$$g(f) = \hat{\beta}_0(f) + \sum_{r=1}^{R} (\hat{B}_r(f) \cos(r2\pi f t_i) + \hat{C}_r(f) \sin(r2\pi f t_i)). \tag{5.2}$$

In terms of a Fourier series of K orders with $2K + 2$ free parameters $\bar{\beta} = (M, f, B_1, \ldots, B_k, C_1, \ldots, C_k)$, Eq. 5.2 becomes

$$g(t, \bar{\beta}) = M + \sum_{k=1}^{K} (B_k \cos(2k\pi f t) + C_k \sin(2k\pi f t)), \tag{5.3}$$

where the mean M and amplitudes B_k and C_k are free parameters. This model can be used used for the pilot search and grid search methods to obtain increasingly refined estimates for f.

The pilot search is the initial search to obtain candidate frequencies by computing a dispersion around an unknown curve. This usually takes the form of a non-parametric test statistic. This step is mostly skipped in the CPS method, described in the following section. The pilot search is described in more detail by Jetsu and Pelt (1999)

The grid search is the next step in TSPA and the first step in the CPS method. It uses a suitable number of crude frequencies f' found via the pilot search to be refined further. In the case of CPS, usually f corresponds to a selected literature value. The order K of the model, and hence τ, is fixed in the grid search so that the free parameters have unique solutions. The discrete tested frequency steps for the grid search, Δf_{grid} are smaller than $\Delta f_{\mathrm{pilot}}$, and an overfilling factor $G \geq 10$ is selected so that $\Delta f_{\mathrm{grid}} = (G\Delta T)^{-1}$, where $\Delta T = t_n - t_i$. The weight for each observation is $w_i = \sigma_i^{-2}$. Because f is fixed in each test, a least squares spectrum can be used, so that the grid search becomes a periodogram that minimizes the residuals,

$$\Theta_{\mathrm{grid}}(f) = 2 \frac{\sum_{i=1}^{n} w_i \epsilon_i}{\sum_{i=1}^{n} w_i}, \tag{5.4}$$

where $\epsilon_i = y(t_i) - g(t_i, \bar{\beta}_f)$ are the residuals, and the factor 2 adjusts $\Theta_{\rm grid}$ to same quantitative level as the pilot search.

The final step is the refined search. The grid search resulted in trial parameter solutions $\bar{\beta}_0$, and the refined uses these parameter values as starting points for a non-linear minimization. The Levenberg-Marquardt iteration can be used to compute $\bar{\beta}$,

$$\chi^2(\bar{\beta}_{\rm min}) = \sum_{i=1}^{n} w_i (y(t_i) - g(t_i, \bar{\beta}_{\rm min})^2, \tag{5.5}$$

where $\bar{\beta}_{\rm min}$ is the solution parameters that minimize χ^2. For significance estimates, χ^2 can be used as described by Jetsu and Pelt (1999). It should be noted that not all parameters that minimize χ^2 are significant, as the process might introduce spurious periods. Some spurious periods can be identified as unphysical, while others can be checked via numerical methods. The significance of the χ^2 results is checked by comparing a random sample of the residuals to a Gaussian distribution using the bootstrap method.

5.1.2 The Continuous Period Search Method

The CPS method is a statistical method described in Lehtinen et al. (2011) which improves upon the TSPA method by using overlapping datasets for higher resolution, calculating different models of order K from 0 to some limit $K_{\rm lim}$, and determining a timescale of change for the variable light curve T_c.

Observations at each point in time are $y_i = y(t_i)$, with the error σ_i. Each dataset contains points from t_1 through t_n, so that the length of each SET is $\Delta T_{\rm max} = t_n - t_1$. Selecting a $\Delta T_{\rm max}$ that is too short will result in too few data points to perform the analysis, and selecting a $\Delta T_{\rm max}$ that is too long will smooth over changes that occur on a timescale shorter than $\Delta T_{\rm max}$. Usually this value is of the order of a month, but will vary from star to star. Observation points for each SET are then contained within $t_1 \leq t_i \leq t_1 + \Delta T_{\rm max}$, and each $\rm SET_k$ cannot contain all points in overlapping $\rm SET_{k+1}$ and vice versa. The number of points n within each SET must be considerably greater than the number of free parameters. The datasets are combined into observing seasons, or segments, where there exists no gaps greater than $\Delta T_{\rm max}$.

The CPS uses the TSPA model,

$$\hat{y}(t_i) = \hat{y}(t_i, \bar{\beta}) = M + \sum_{k=1}^{K} [B_k \cos(k 2\pi f t_i) + C_k \sin(k 2\pi f t_i)], \tag{5.6}$$

where the model is of order K with $2K + 2$ free parameters $\bar{\beta} = [M, B_1, \ldots, B_K, C_1, \ldots, C_K, f]$. The period of the light curve $P = 1/f$ and mean magnitude come directly from the free parameters $\bar{\beta}$, while the amplitude A is the easiest to determine numerically. For all models where $K \geq 2$, the primary and secondary minima epochs $t_{\min,1}$ and $t_{\min,2}$ can also be determined numerically. These minima epoch are of particular interest with variable stars, as they can be used to estimate persistent active longitudes.

The frequency $f = 1/P$ can be searched within a period range of $(1 - q)P_0 \leq P \leq (1+q)P_0$. A standard selection for q is 0.15, and this takes into account possible variations (due to, for example, differential rotation) of 15% around P_0. $\bar{\beta}$ is found by using the grid and refined searches of the TSPA method. The highest order model is denoted by K', and is selected so that a good fit is achieved without overfitting. This can be done using a Bayesian information criterion,

$$R_{\mathrm{BIC}} = 2n \ln \lambda(\bar{y}, \bar{\beta}) + (5K + 1) \ln n \tag{5.7}$$

This criterion is selected based on the limits imposed by the penalty term, $(5K + 1) \ln n$, so that there exists an minimum value for R_{BIC} over all K that avoids overfitting.

Errors are estimated in a similar way to the TSPA method, where a certain number of bootstrap estimates (e.g., 200) are made. Additionally, resulting distributions are tested using the Kolmogorov-Smirnov test against the Gaussian hypothesis, where a random sampling of the residuals or free parameters is drawn from a Gaussian distribution. A significance threshold of $\gamma = 0.01$ is used for rejection.

Variable stars change over time, and this timescale of change, T_c, is of interest. T_c is the time within a segment that a model provides a reasonable fit. The mean of t_i within a dataset is τ. The residuals of the next dataset are computed using the model of the first dataset, and compared using a two-sided Kolmogorov-Smirnov test. If the test is passed, then the next dataset is compared, the residuals computed, and the process repeated until the test fails or the end of the segment is reached. In the former case, T_c is now the time difference between the τ of the first dataset and the τ of the last dataset that provided a reasonable fit to the model. Otherwise we conclude that the model was valid for the rest of the segment.

5.1.3 The Carrier Fit Method

The Carrier Fit method (hereafter CF) utilizes concepts from communication, where a single harmonic tone, or carrier frequency, is modulated by the signal. When applied to astronomy, the rotation period of a star is considered the carrier frequency

and any variations in the light curve parameters can be modeled by complex waveforms. An overview of the method is described here, and a more detailed explanation can be found in Pelt et al. (2011).

The waveform to describe the rotation frequency of a star can be described by

$$f(t) = a(t)\cos(2\pi t\nu_0) + b(t)\sin(2\pi t\nu_0), \tag{5.8}$$

where $a(t)$ and $b(t)$ are smooth, low frequency components, and ν_0 is the carrier frequency. For the stellar case, this frequency is $1/P_0$ where P_0 is the rotation period of the star, most commonly expressed in units of days for astronomical objects. The analytic complex form can be expressed as

$$f_a(t) = A(t)e^{2\pi j\varphi(t)}, \tag{5.9}$$

which allows for explicit tracking of the amplitude $A(t)$ and instantaneous frequency $\nu(t) = d\varphi(t)/dt$. Equation 5.8 uses the lowest harmonic $k = 1$. However, more harmonics are needed to describe the carrier waveform as multiple spots with slightly different rotation periods will modulate the signal. This variability in the signals of astronomical objects, particularly light curves, is best described by the truncated, slowly modulated harmonic decomposition waveform

$$f(t) = a_0(t) + \sum_{k=1}^{K}((a_k(t)\cos(2\pi tk\nu_0) + b_k(t)\sin(2\pi tk\nu_0)), \tag{5.10}$$

where $a_0(t)$ is the time-dependent mean value of the signal, and K is an adequately large integer for a good fit but not so large as to cause over-fitting.

The CF method is carried out in three steps. First, the carrier frequency ν_0 must be determined and improved. Next, models must be selected for $a(t)$ and $b(t)$. The final step would be selecting the model which best describes the observations, and retrieving and interpreting the relevant parameters of the model. The CF method allows for some visualization methods that lend themselves to easier inspection of final results.

The carrier frequency ν_0 is the inverse of the rotation period, P_0. The initial estimate of P_0 does not need to be precise, as it can be improved if there is an upward or downward trend in resulting phase plots. Estimates for P_0 can be obtained from literature, observations, or other methods. One possible method for determining the optimal frequency is outlined in Pelt et al. (2011), but this method may converge slowly. Instead the D^2 statistic from Pelt (1983) is used in Paper V to find a consistent average cycle period, P_0. This method has been used by, for example, Käpylä

et al. (2016a) to examine solar variations and by Lindborg et al. (2013) with the photometry of II Pegasi. The D^2 statistic as a function of the trial period P and coherence time Δt is written as

$$D^2(P, \Delta t) = \frac{\sum_{i=1}^{N} \sum_{j=i+1}^{N} g(t_i, t_j, P, \Delta t)[f(t_i) - f(t_j)]^2}{2\sigma^2 \sum_{i=1}^{N} \sum_{j=i+1}^{N} (g(t_i, t_j, P, \Delta t))}. \tag{5.11}$$

Here, $f(t_i)$, $i = 1, \ldots, N$ is the input time series, σ^2 is the variance, and $g(t_i, t_j, P, \Delta t)$ is a selection function that is only larger than zero when $t_i - t_j \approx kP$ with $k = \pm 1, \pm 2, \ldots$, or $|t_j - t_i| \lessapprox \Delta t$. Smaller values for Δt obtain a P_0 that may not be coherent for the entire time span. The D^2 spectrum approaches the result of a Fourier transform at large values for Δt close to the full time span. The value then for P_0 is selected based on the optimal Δt, where Δt is the longest coherence time possible for which the dispersion function is still a symmetric single peak.

Once a satisfactory value for P_0 is obtained, models can be selected for $a(t)$ and $b(t)$. A variety of approximations can be selected, but here only the trigometric approximation is described. When there are no sharp transients and a need to explicitly control the frequency domain, then the trigometric approach is ideal. To do this, a range of observation times is selected, $[t_{\min}, t_{\max}]$. There is then a period $D = C \cdot (t_{\max} - t_{\min})$, where C is some coverage factor, usually a value between 1.1 and 1.5. D must be much greater than P_0 in order for the change to be considered a slow process. The data frequency is then $\nu_d = 1/D$. The low frequency components are thus defined as

$$a(t) = c_0^a + \sum_{l=1}^{L} (c_l^a \cos(2\pi t l \nu_D) + s_l^a \sin(2\pi t \nu_D)), \tag{5.12}$$

and

$$b(t) = c_0^b + \sum_{l=1}^{L} (c_l^b \cos(2\pi t l \nu_D) + s_l^b \sin(2\pi t \nu_D)). \tag{5.13}$$

This model now has the form $\left\{ \begin{array}{c} \sin \\ \cos \end{array} \right\} (2\pi t(\nu_0 \pm l\nu_D))$, where $l = 0, \ldots, L$. A standard linear estimate procedure can be used to compute expansion coefficients for each term in the series for ν_0 and ν_D.

The simple form of the model, described by Eq. 5.8, uses the lowest harmonic $k = 1$, and should be expanded to the full case to include overtones of higher orders

of k, i.e., $k = 1, \ldots, K$. The trigonometric polynomial models the time dependence of $a_0(t)$. $a_k(t)$ and $b_k(t)$ are constructed representations for each overtone of the carrier frequency $k\nu_0$. If each of these polynomials has the same L and is independent of the harmonic index k, then the total number of parameters to solve for is $N = (2L + 1)(2K + 1)$. K is the number of tones and depends on the complexity of the phase curves, while L is constrained by the largest gaps in the time series. The Bayesian information criterion (Eq. 5.7) can similarly be applied here to impose limits on L and K.

The final step of the CF method is to select a model which best fits the observations and retrieve the informative parameters. A standard least-squares approximation procedure is used to calculate the parameters. The model is usually limited to the linear regime, although some fits might require a non-linear approach.

The advantage of the CF method is that with the parameters solved, the function $f(t)$ can be reconstructed for visualization purposes for a desired t-range, filling in gaps in observations. The visualization technique divides $f(t)$ into segments of length $P_0 = 1/\nu_0$, and normalizes each of these segments which are then stacked along the time axis. The resulting phase plots can be used to visually inspect trends as well as discern various activity events of interest, such as flip-flops or dynamo waves. Additionally, a power spectrum of $f(t)$ can reveal trends in the frequency structure.

6 Doppler Imaging

Doppler Imaging (hereafter DI) is an inverse method for analyzing spectral lines for "bumps" and reconstructing a temperature map of the stellar surface based on the position and depth of these bumps and changes over time. Starspots are cooler areas at the surface of the star that locally distort the photospheric absorption lines. As the star rotates these distortions move across the disk-integrated absorption lines. If the star rotates fast enough the spot latitude and longitude determine how much the bump is blue- or red-shifted from the center of a spectral line. With multiple observations, the latitude of the spot can then be calculated based on the radial velocity range of the bump traveling across the spectral line. Bumps that correspond to spots at high latitudes will remain near the central wavelength and bumps that correspond to equatorial spots will move all the way across the spectral line.

6.1 Doppler Imaging methods

The Doppler imaging problem can be formulated as a discrepancy function minimized over several iterations to recreate a surface map that matches observations. First, a parameter $X(M)$ is selected, where M is the location on a grid of the stellar surface. This parameter is temperature in the case of stars with cool spots the surface. The rotational velocity $v \sin i$ and the inclination angle i of the stellar object must be known. The number of phases observed is N_ϕ and the number of spectral lines used is N_λ. The discrepancy function is then

$$D(X) = \sum_{\phi,\lambda} \frac{w_{\phi,\lambda} \left[r_\phi^{\mathrm{obs}}(\lambda) - r_\phi^{\mathrm{calc}}(\lambda) \right]^2}{N_\phi N_\lambda}, \tag{6.1}$$

where $w_{\phi,\lambda} = 1/\sigma^2$ is the weights of the observations in relation to the error derived from the S/N, $r_\phi^{\mathrm{obs}}(\lambda)$ is the observed spectral line profiles at phase ϕ and wavelength λ, and $r_\phi^{\mathrm{calc}}(\lambda)$ is the calculated residual spectral line profile.

The most important part of the inversion is obtaining accurate values for $r_\phi^{\rm calc}$. Spot latitude, phase, and temperature are all determined based on deviations from the line profile of an unspotted surface, and so artifacts are potentially introduced if poorly calculated line profiles are used. While methods such as using a template star are possible, the method used here involves directly solving the radiation transfer equation using numerical stellar models and spectral parameters from a database, such as the Vienna Atomic Line Database (Piskunov et al., 1995). In addition, certain stellar parameters are needed: the microturbulence $v_{\rm micro}$, the macroturbulence $v_{\rm macro}$, the gravity $\log g$, the rotation velocity $v \sin i$, the inclination angle i, the rotation period $P_{\rm rot}$, the element abundance, and the differential rotation coefficient k. The differential rotation can usually be neglected with most rapidly-rotating late-type stars as the differential rotation tends to be small.

The calculated line profiles are a combination of the line flux and the continuum, so that

$$r^{\rm calc}(\lambda) = 1 - \frac{F_{\rm line}(\lambda)}{F_{\rm cont}(\lambda)} \tag{6.2}$$

where $F_{\rm line}$ is the disk integrated spectral line flux and $F_{\rm cont}$ is the disk integrated continuum flux. A precalculated table is created for local line profiles to interpolate the intensities $I(X, \lambda, \mu)$ where μ is the limb angle. The integrated flux is

$$F_\lambda = \iint I(X(M), \lambda + \Delta\lambda, \mu)\mu dS, \tag{6.3}$$

where $\Delta\lambda$ is the Doppler shift at point M, and dS denotes an integral over the visible stellar surface. The flux from F_λ can then be convoluted with the instrumental profile of observations and $v_{\rm macro}$ to obtain $F(\lambda)$.

A solution is sought which minimizes Eq. 6.1, in other words, the optimal $X(M)$ is that for which D converges to the level of the noise in the observations. Since the problem is ill-posed, further constraints are required to achieve a unique solution. The solution is to use a regularization function and constrain the solution to reasonable values by using a penalty function, so that

$$\Phi(X) = D(X) + \Lambda R(X) + \mathcal{F}_p(X). \tag{6.4}$$

Here, Λ is a Lagrange multiplier, $R(X)$ is a regularization function, and $\mathcal{F}_p$ is the additional penalty function.

The two most common selections for a regularization function is the maximum entropy method, and the Tikhonov method (Piskunov et al., 1990). The maximum entropy method is a solution which seeks the configuration with the greatest entropy

(Skilling and Bryan, 1984). It is most useful in cases where there is little to no correlation between neighboring points, and can be formulated as a double integral over the stellar surface,

$$R_{\mathrm{ME}}(X) = \iint X(M) \log X(M) dS(M). \tag{6.5}$$

However, in cases where neighboring points correlate strongly, the Tikhonov regularization is useful. The Tikhonov regularization has the form

$$R_{\mathrm{T}}(X) = \iint ||\nabla X(M)||^2 dS(M). \tag{6.6}$$

This regularization function is better suited to mapping temperatures of late-type stars as it converges to a smooth solution that is more easily adjustable to the S/N, spectral resolution, and phase coverage.

The penalty function $\mathcal{F}_p(X)$ is useful to limit the temperature range to reasonable values, as the local line profile tables used for r_{calc} have limited temperature ranges. A temperature range is selected, $[T_{\mathrm{min}}, T_{\mathrm{max}}]$, and

$$\mathcal{F}_p(X) = \sum_i f_p(x_i) \tag{6.7}$$

where x_i is the temperature of a surface element, and $f_p = 0$ when $x \in [T_{\mathrm{min}}, T_{\mathrm{max}}]$ and f_p increases linearly when $x \notin [T_{\mathrm{min}}, T_{\mathrm{max}}]$.

6.1.1 Candidates for Doppler Imaging

In order for the Doppler imaging method to work, there are certain restrictions in stellar parameters, spectral parameters, and the spatial and temporal resolution of the observations.

With regards to the observations, the spectrometer should preferably have a resolution of 40000 or greater, so that spectral lines are well-enough resolved to detect bumps within the the rotationally broadened spectral line. Ideally, there should be about 10 observations at evenly spaced phases within a few weeks so that the entire surface can be mapped without being affected by drastic changes of the spot structure. The signal to noise S/N of individual observations should be high enough so that the often small changes in the spectral lines within the target wavelength region are not buried in the noise. An S/N of 200 or greater is usually the limit, but exceptions can be made for lower S/N $\sim$ 100 if enough spectral lines are used in the inversion. Doppler imaging is possible for even lower S/N by using

a least squares deconvolution or other similar methods to combine the signal from a large amount of lines. However tests show that this technique is not unproblematic, as additional artifacts and loss of information will occur (Rosén et al., 2016).

With regards to the stellar object, the method is limited by the Doppler effect itself. If a star is rotating too slowly, the spectral line's full width at half maximum is too small to resolve any Doppler shifts of the spots, and if the rotational velocity is too fast, the lines become too blended. This imposes a lower limit for $v \sin i$ of about 20-30 km/s and an upper limit of about 200 km/s. The inclination angle i should preferably also lie within certain limits. If the angle is too high, mirroring effects occur when the inversion process cannot distinguish between the two hemispheres, and if the angle is too low, the projected rotational velocity will be too low. This translates to roughly $20^\circ \lesssim i \lesssim 70^\circ$, but these limits are not clear and it is possible to perform the DI method on stars with an i outside these limits. Other stellar properties must be fairly well-known, such as metallicity and gravity as these are used to choose the right stellar models for calculating the spectral line tables.

6.1.2 Errors and Artifacts

Incorrect input parameters, errors in the observations, and incorrect calculated local line profiles can lead to artifacts in the final image. Systemic errors thus have a larger impact than observational noise, and largely depends on minimizing the former errors.

The spectral resolution in combination with the rotation velocity effectively creates a lower limit to the size of spot that can be resolved, as the inverse method cannot reconstruct spots below the resolution limit. If again the inclination angle is small, spots at the same longitude but different latitudes become difficult to distinguish and some smearing in the latitudinal direction may occur. Some contrast and resolution is lost when the S/N is low, however, a S/N as low as 100 does not introduce spurious spots (Vogt et al., 1987). Longitudinal stripes may appear as an artifact on the recovered surface map as a result of low S/N. If the iterations are carried below the S/N level and not enough spectral lines are used, the final result may have many smaller, high-contrast features as a result of the inversion interpreting the noise as spots. Phase gaps are often a reality due to the limitations in obtaining enough observations at enough phases within a short period of time. Some information regarding spot shape, size, and location is lost, however, some useful conclusions can still be drawn from the resulting maps. Insufficient phase coverage has the biggest impact on the latitude of spots, and so some caution must be used when interpreting results.

The stellar parameters chosen may also introduce some artifacts. Inclination angles are somewhat difficult to determine for non-binary stars, however, an inaccurate inclination angle that is more than $\pm 10^{\circ}$ off from the actual value will change the spot latitudes and the contrast between high and low temperature regions of the recovered surface, but otherwise the results are somewhat insensitive to i. The results are more sensitive to the chosen rotation velocity. If the selected $v \sin i$ is too low or too high, a low latitude dark or light band respectively appears in the recovered surface map. However, the $v \sin i$ can be fine-tuned by minimizing the wavelength dependence of the discrepancy. If the assumption of a low differential rotation is incorrect, the final results may also show a spurious equatorial band or polar spot, based on whether the real differential rotation is of solar or anti-solar type (Bruning, 1981; Hackman et al., 2001). If there is a difference between the actual rotational broadening profile and calculated rotational broadening of the spectral lines, more axisymmetric artifacts such as a latitudinal band of spots or polar spot will appear in the recovered temperature map. If some errors are present in some observed phases but not others, then spurious arches or ovals may appear in the retrieved image.

As stated before, the local lines profiles calculations for r^{calc} are important because inaccurate line profiles will introduce systemic errors into the inversion. The calculations are an approximation, and certain assumptions such as local thermodynamic equilibrium are made that may not be true for the upper photosphere of the star. Additionally, the local line profiles do not take into account the presence of strong magnetic fields. The evolutionary stage of the stellar object may also have some impact on the actual local line profiles.

7 Results

7.1 Numerical Simulations

7.1.1 Turbulent Convection in Spherical Wedges

In Paper I, the effect of stratification on dynamo solutions in turbulent convection simulations is explored. These models are largely based on those by Käpylä et al. (2012), where equatorward migration was found in models with solar-like differential rotation. Furthermore, when physical units are used, a careful study by Warnecke et al. (2014) finds that the dynamo cycle is close to 5 years. In Paper I, we seek to understand further the regime of dynamos with equatorward migration in terms of density stratification as well as examine the impact of the azimuthal wedge size on the dynamo.

Table 7.1 contains the input parameters of the runs. Groups A–D explore the density stratification. Group E uses the density stratification where equatorward propagation is found, and explores the impact of the azimuthal wedge size, increasing the domain size in the ϕ-direction only. The sub-grid scale Prandtl number, $\mathrm{Pr}_{\mathrm{SGS}} = \nu/\chi_{\mathrm{SGS}}$ is related to the SGS flux; for the discussion of χ_{SGS} see Section 4.2.2. Runs B1, C1, and D1 are the magnetic analogs of hydrodynamic Runs A4, B4, and C4 by Käpylä et al. (2011a). Angular velocity values were selected such that they were high enough for large-scale magnetic fields to grow (e.g., Brown et al., 2010; Käpylä et al., 2012). In order to compare the models to the Sun, the models are assumed to have the solar luminosity and the Ω values are calculated accordingly (see Käpylä et al., 2014). The fastest rotator, C2, has a rotation period between 3–4 days, and the slowest, A1, has a rotation period of 12–13 days.

The growth of the magnetic field is exponential during the kinematic stage, and can be expressed as

$$\lambda = \langle d \ln B_{\mathrm{rms}}/dt \rangle_t. \tag{7.1}$$

Our results show that smaller stratification results in larger growth rates. During this kinematic stage, a dynamo at low latitudes with poleward migration and

Table 7.1: Input parameters of runs in Paper I.

Run	Pr	$\mathrm{Pr_{SGS}}$	Pm	Ta $[10^{10}]$	ξ	$\Gamma_\rho^{(0)}$	$\tilde{\nu}$ $[10^{-5}]$	$\mathcal{L}$ $[10^{-5}]$	$\tilde{\sigma}$ $[10^3]$	$\tilde{\Omega}$ $\tilde{\Omega}_\odot$
A1	71	1.5	1.0	1.0	0.29	2.0	1.7	3.8	.001	2
A2	71	1.5	1.0	1.8	0.29	2.0	1.7	3.8	.001	3
B1	82	2.5	1.0	0.64	0.09	5.0	2.9	3.8	0.011	3
B2	82	2.5	1.0	1.4	0.09	5.0	2.9	3.8	0.011	4.4
C1	56	2.5	1.0	1.4	0.02	30	2.9	3.8	1.4	4.4
C2	56	2.5	1.0	4.0	0.02	30	2.9	3.8	1.4	7
D1	503	7.5	3.0	0.16	0.01	100	4.7	0.63	39	4.3
D2	269	4.0	2.0	1.0	0.01	100	2.5	0.63	39	6
E1	56	2.5	1.0	1.4	0.02	30	2.9	3.8	1.4	4.4
E2	56	2.5	1.0	1.4	0.02	30	2.9	3.8	1.4	4.4
E3	56	2.5	1.0	1.4	0.02	30	2.9	3.8	1.4	4.4
E4	67	3.0	1.0	1.0	0.02	30	3.5	3.8	1.4	4.4

Notes. Modified from Paper I, Table 1.

a short period is excited. As the dynamo saturates in the more rapidly rotating runs, quasi-stationary or slower oscillatory dynamo modes take over. The threshold for equatorward migration of the magnetic field occurs when the initial density stratification is increased to $\Gamma_\rho^{(0)} = 30$ and the angular velocity is increased so that $\mathrm{Co} = 7.8$ (Run C1). Poleward migration, previously a common feature of similar simulations (e.g., Gilman, 1983; Glatzmaier, 1985; Käpylä et al., 2010; Brown et al., 2011), becomes subdominant to the equatorward dynamo wave.

Figure 7.1 shows the normalized azimuthal magnetic field of Runs C1 (*left*) and E4 (*right*). For Run E4, the kinematic stage can be seen from the small, short-period cycles at $tu_{\mathrm{rms}}k_{\mathrm{f}} < 1000$, where $tu_{\mathrm{rms}}k_{\mathrm{f}}$ is the convective turnover time. After Run E4 saturates, equatorward propagation of longer period operates until $\sim 2000tu_{\mathrm{rms}}k_{\mathrm{f}}$, with antisymmetry about the equator. This equatorward propagation starts around the latitudes $\pm 40°$, and higher latitudes have a weaker, poleward oscillatory dynamo wave. In Run E4, after $tu_{\mathrm{rms}}k_{\mathrm{f}} \sim 2000$, a quasi-stationary axisymmetric mode appears and a non-axisymmetric $m = 1$ dynamo mode takes over. In Run C1, the oscillatory dynamo continues to dominate for the duration of the simulation. Whenever the dynamo oscillates with equatorward migration, the magnetic field also appears strongly near the latitudinal boundary, and thus it might be possible that these oscillations are an artifact. Jennings et al. (1990) found that using wedges

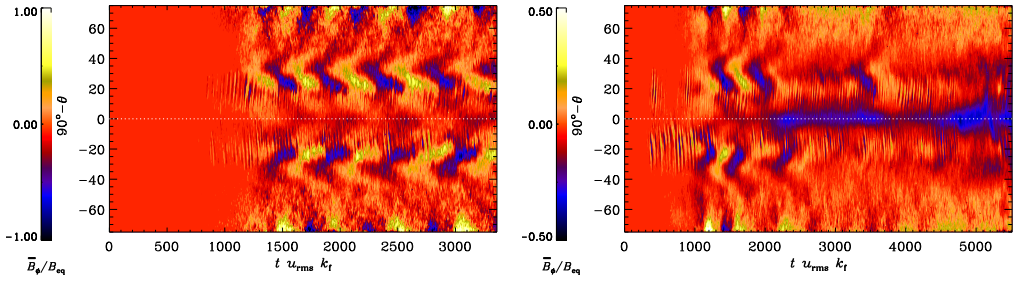

Figure 7.1: Azimuthal magnetic field at $r = 0.98R$ over time. Runs C1 (*left*) and E4 (*right*) from Paper I.

that do not extend to the poles gives a good approximation of a fully spherical model, but this assumption was for $\alpha\Omega$ dynamos. The impact of the boundary condition is explored in Paper III.

Table 7.2 lists some of the output diagnostics from the runs. The radial differential rotation is defined as

$$\Delta_\Omega^{(r)} = \frac{\overline{\Omega}_{\rm eq} - \overline{\Omega}_{\rm bot}}{\overline{\Omega}_{\rm eq}}, \tag{7.2}$$

and the latitudinal differential rotation is

$$\Delta_\Omega^{(\theta)} = \frac{\overline{\Omega}_{\rm eq} - \overline{\Omega}_{\rm pole}}{\overline{\Omega}_{\rm eq}}. \tag{7.3}$$

Here, $\overline{\Omega}_{\rm eq} = \overline{\Omega}(R, \pi/2)$ is the rotation rate averaged over ϕ at the equator and the top of the convection zone, $\overline{\Omega}_{\rm bot} = \overline{\Omega}(r_0, \pi/2)$ is the rotation rate averaged at the equator and the bottom of the convection zone, and $\overline{\Omega}_{\rm pole} = [\overline{\Omega}(R, \theta_0) + \overline{\Omega}(R, \pi - \theta_0)]/2$ is the average rotation at the north and south latitudinal boundaries at the top of the convection zone. The radial gradients for all runs are positive. The latitudinal gradients of rotation are also positive for all runs except D2, but in some runs, for example, C1 and C2, it is not monotonic. Instead, around mid-latitudes, a local minima appears which is approximately the same location at which the equatorward propagation of the magnetic field originates. In all cases, differential rotation is smaller than that of the Sun, which is in accordance with observations that more rapid rotation results in decreased differential rotation in stars (e.g., Henry et al., 1995; Donahue et al., 1996; Messina and Guinan, 2003; Barnes et al., 2005) and in numerical simulations (e.g., Kitchatinov and Rüdiger, 1995; Käpylä et al., 2011a).

Table 7.2: Summary of runs in Paper I, selected output parameters.

Run	$\tilde{\lambda}$	Γ_ρ	$\mathrm{Ra_t}$ $[10^6]$	Re	Rm	Co	$U_{\rm rms}$	$E_{\rm mag}/E_{\rm kin}$	$\Delta_\Omega^{(r)}$	$\Delta_\Omega^{(\theta)}$
A1	0.084	2.1	0.83	26	26	8.6	0.010	0.418	0.013	0.089
A2	0.095	2.1	0.11	24	24	12.8	0.009	0.553	0.009	0.050
B1	0.028	5.3	1.1	22	22	8.1	0.013	0.345	0.034	0.142
B2	0.098	5.2	1.1	20	20	13.7	0.012	0.222	0.023	0.072
C1	0.006	22	2.1	35	35	7.8	0.021	0.346	0.047	0.068
C2	0.105	21	2.7	31	31	14.8	0.019	0.706	0.016	0.030
D1	0.003	85	1.2	11	34	8.0	0.011	0.472	0.011	-0.00
D2	0.003	74	2.4	25	50	9.1	0.013	0.222	0.045	0.058
E1	0.007	22	2.1	34	34	7.9	0.021	0.393	0.048	0.069
E2	0.006	22	2.1	35	34	7.8	0.012	0.346	0.047	0.068
E3	0.005	22	2.4	35	35	7.9	0.021	0.380	0.037	0.055
E4	0.024	23	2.2	28	28	8.1	0.020	0.477	0.028	0.054

Notes. $E_{\rm mag} = \frac{1}{2}\langle \boldsymbol{B}^2 \rangle$ is volume-averaged magnetic energy and $E_{\rm kin} = \frac{1}{2}\langle \rho \boldsymbol{U}^2 \rangle$ is volume-averaged kinetic energy. The normalized growth rate is $\tilde{\lambda} = \lambda/(U_{\rm rms} k_f)$. Ra_t is Ra for the thermally relaxed state. Modified from Paper I, Tables 1 and 2.

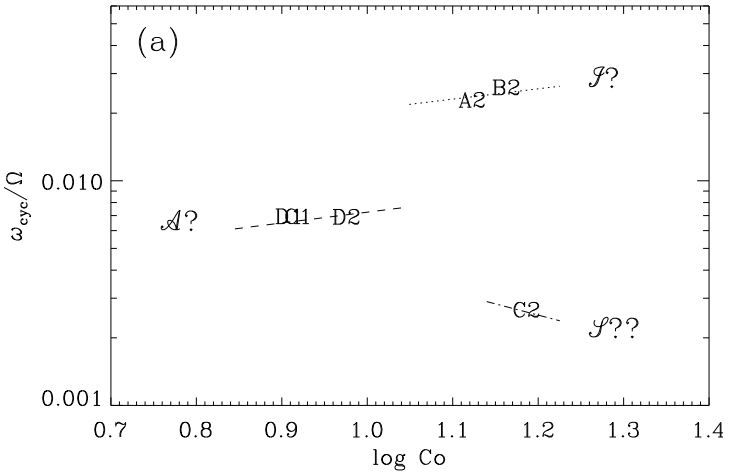

Figure 7.2: Cycle frequency and Coriolis number relation for runs in Paper I.

However, the the strength of differential rotation of the models in both Papers I and II is higher than differential rotation rates deduced from stars (Henry et al., 1995; Marsden et al., 2005; Siwak et al., 2010; Lehtinen et al., 2016).

In order to make a comparison to active stars, runs with oscillatory modes A2, B2, C1, C2, D1, and D2 are compared in terms of their respective Co and cycle frequency, shown in Figure 7.2. Dynamo cycle length is calculated from the oscillations of the magnetic field, to see if the models lie along activity branches analogous to the branches found from observations by Brandenburg et al. (1998) and Saar and Brandenburg (1999). It is possible that Run C2 is suggestive of a superactive branch ($\mathscr{S}$), Runs C1, D1, and D2 possibly correspond to the active branch ($\mathscr{A}$), and Runs A2 and B2 are possibly on the inactive branch ($\mathscr{I}$). However, there are too few models to truly make an accurate comparison, and it is possible that the time series of our models is too short. And while $\omega_{\rm cyc}/\Omega$ appears to be an important parameter for the models in Paper I, Run A2 was classified as inactive even though its magnetic energy is higher than C1, D1, B2, and D2, (see Figure 8, Paper I).

While the initial goal of Paper I was to explore the stratification regime where equatorward dynamo modes appeared, later work by Käpylä et al. (2016b) studied the impact of viscous, thermal, and magnetic diffusivity and found that $\mathrm{Pr}_{\rm SGS}$ is responsible for the equatorward migration. In Paper I, the cases where $\mathrm{Pr}_{\rm SGS} \gtrsim 2.5$ have equatorward migratory belts, except at high Rm, at which point the dynamos

become irregular. As this parameter increases beyond unity, the sign of the radial shear changes near mid-latitudes, and the dynamo mode switches from poleward to equatorward. When thermal diffusivity is high, and correspondingly $\mathrm{Pr}_{\mathrm{SGS}} < 1$, the rotation profile changes almost monotonically as a function of latitude. Käpylä et al. (2016b) also found that as the magnetic diffusivity is decreased, and Rm increased, the dynamo switches from oscillatory to irregular or quasi-stationary, something also observed in the runs of Paper I. Other numerical simulations with similarly higher Prandtl numbers have also resulted in equatorward dynamo waves (e.g., Käpylä et al., 2012; Warnecke et al., 2013; Augustson et al., 2015). The Parker-Yoshimura sign rule (Eq. 3.44) only allows for equatorward migration when the sign of α is opposite that of $\partial\Omega/\partial r$. Thus, a positive α in the northern hemisphere requires a negative radial gradient in order for a dynamo wave to propagate equatorward. The models of Paper I produce a region with negative radial shear at mid-latitudes when the Prandtl number connected to the unresolved turbulent flux is sufficiently high. This is also what is found in the models by Käpylä et al. (2012) and Augustson et al. (2015). The only other possible way to have an equatorward dynamo wave is to invert the sign of α in the bulk of the convection zone (Duarte et al., 2016).

The dynamo type can be estimated using dynamo numbers $C_\alpha = \alpha\Delta r/\eta_{\mathrm{t}0}$ and $C_\Omega = \partial\overline{\Omega}\partial r(\Delta r)^3/\eta_{\mathrm{t}0}$. Because the simulation is nonlinear, the estimate of the α effect includes both kinetic and current helicity, in other words, $\alpha = -1/3\tau(\overline{\boldsymbol{\omega}\cdot\boldsymbol{u}} - \overline{\boldsymbol{j}\cdot\boldsymbol{b}}/\overline{\rho})$, where $\tau = \alpha_{\mathrm{MLT}}H_{\mathrm{P}}/U_{\mathrm{rms}}(r,\theta)$ and $\alpha_{\mathrm{MLT}} = 5/3$. For the oscillatory Runs C1, C2, D1, and D2, C_Ω is comparable to C_α, but the Ω effect is strongest around mid-latitudes. So an $\alpha^2\Omega$ dynamo seems possible, at least from the local dynamo numbers. However, the phase relation between $\overline{B}_r$ and $\overline{B}_\phi$ can be used to determine the sign of radial differential rotation for $\alpha^2\Omega$ dynamos (e.g., Yoshimura, 1976). If the shear is negative, $\overline{B}_\phi$ should precede $\overline{B}_r$ by about $3\pi/4$, and if the shear is positive, $\overline{B}_\phi$ should lag behind $\overline{B}_r$ by about $\pi/4$. Run C1 actually shows $\overline{B}_\phi$ lagging behind $\overline{B}_r$ by approximately $\pi/2$, which is a relation found for α^2 dynamos in Cartesian coordinates by Brandenburg et al. (2009). Thus it would seem that the dynamos here are the α^2 type, and not $\alpha^2\Omega$. However, Warnecke et al. (2014) found a standard $\alpha\Omega$ operating in deeper layers that may be instead responsible for generating the observed behavior, and the values for B_ϕ and B_r taken near the surface may instead be indicative of a thin shell of an α^2 dynamo operating near the surface.

The effect of increasing the longitudinal extent of the simulations is also addressed in Paper I. Of particular interest is the effect when the longitudinal extent is increased to 2π. Smaller wedges are less computationally demanding, but it is important to examine what effects are lost when running simulations that have a reduced azimuthal extent. Runs E1–E4 examine the impact of ϕ_0 on the resulting dynamo. A so-called

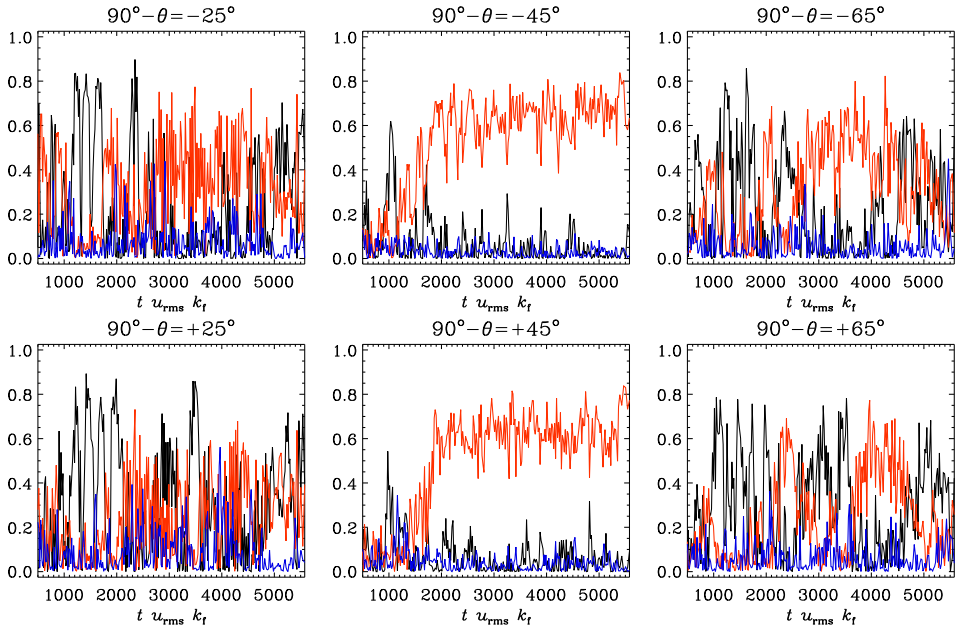

Figure 7.3: Amplitudes of the low order Fourier modes of the magnetic field with time for Run E4. Black corresponds to $m = 0$, red to $m = 1$, and blue to $m = 2$. From Paper I, Figure 18.

"azimuthal dynamo wave" is observed, where the $m = 1$ mode is found at certain latitudes and propagates in the azimuthal direction with a slower rotation than the mean rotation. This is further explored in Paper II. This mode is as easily excited in α^2 dynamos as the $m = 0$ mode, and the growth of the $m = 1$ mode can be seen in Figure 7.3, for run E4 in Paper I. The $m = 1$ mode (red line) persists at mid-latitudes and dominates over shorter time periods at other latitudes. The $m = 2$ mode indicated in blue has a smaller growth rate in α^2 dynamos, which is consistent with the results of the simulation (Rädler, 1986).

7.1.2 The Azimuthal Dynamo Wave

Paper II is a continuation of the themes of Run E4 from Paper I. It is evident from visual inspection of the azimuthal field near the surface (Fig. 7.4) that there is a large-scale structure corresponding to the $m = 1$ mode that rotates with a different

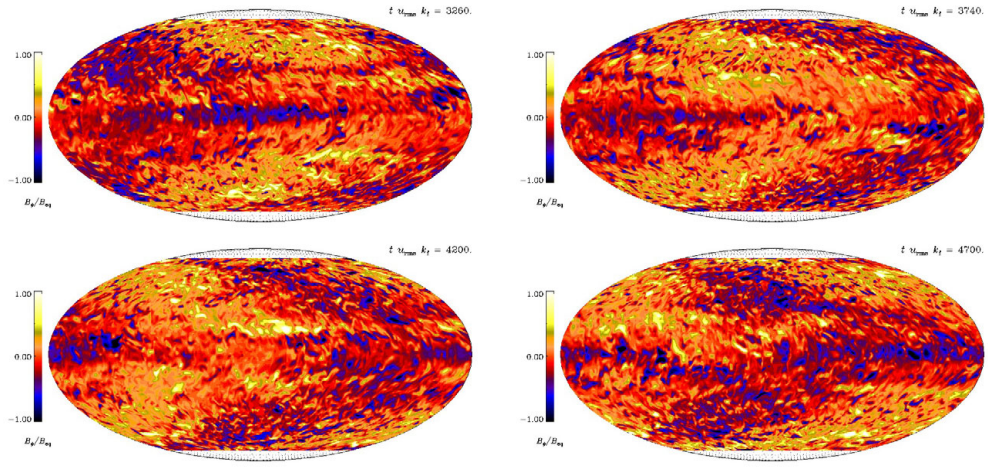

Figure 7.4: The azimuthal magnetic field at $r = 0.98R$ normalized by the equipartition magnetic field, in the co-rotating frame, at four different times. From Paper II, Figure 1.

speed than would be expected if pure advection carried the structure. The structure rotates slower than the mean rotation rate of the model. Both slower and faster rotation of the azimuthal dynamo wave relative to the mean rotation is theorized to be possible in the nonlinear regime (Rädler et al., 1990), and spot structures rotating either faster or slow than the mean rotation have been observed in stars (Berdyugina and Tuominen, 1998, e.g.,). Such a wave could be used to explain the observed faster rotation of spot structures relative to the mean rotation of stars such as II Peg (Hackman et al., 2012) as compared to mechanisms such as differential rotation that is sometimes used to explain spot drift in other stars such as FK Com (Korhonen et al., 2007). Furthermore, disruptions and switches between faster and slower rotation rates have been observed in some stars as well (Hackman et al., 2013). The observed $m = 1$ mode in latitudinal bands of strong magnetic fields in Run E4 are similar to the more axisymmetric ($m = 0$) wreaths in simulations by, for example, Brown et al. (2010) and Nelson et al. (2013). More rapid rotation should also lead to parities approaching +1 about the equator (e.g., Rädler et al., 1990; Moss et al., 1995).

Some diagnostic and input parameters of Paper II are shown in Table 7.3. Run B is the same as Run E4, and other corresponding input parameters not shown

Table 7.3: Summary of runs from Paper II, selected input parameters and diagnostics.

Run	$\mathrm{Pr_{SGS}}$	$\tilde{\nu}[10^{-5}]$	$\mathrm{Ra_t}[10^6]$	Re	Rm	Co	$\tilde{\Omega}/\tilde{\Omega}_\odot$
A	3.5	4.1	1.7	26	26	5.0	2.7
B	3.0	3.5	2.2	28	28	8.1	4.0
C	3.0	3.5	2.6	24	24	15.5	6.7

Notes. Run B is Run E4 from Paper I. All other input parameters are identical to those of Run E4. $\tilde{\Omega}/\tilde{\Omega}_\odot$ is the average rotation rate of the Run relative to the average solar rotation rate. Modified from Table 1, Paper II.

Table 7.4: Summary of runs from Paper II, selected output diagnostics.

Run	$\tilde{E}_{\mathrm{mag}}$	$\tilde{E}^{(0)}$	$\tilde{E}^{(1)}$	M	P
A	0.312	0.166	0.047	0.834	-0.333
B	0.618	0.109	0.071	0.891	0.318
C	0.937	0.056	0.091	0.944	0.347

Notes. Here, the normalized magnetic energy is $\tilde{E}_{\mathrm{mag}} = E_{\mathrm{mag}}/E_{\mathrm{kin}}$, and $\tilde{E}^{(0)} = E^{(0)}/E_{\mathrm{mag}}$ and $\tilde{E}^{(1)} = E^{(1)}/E_{\mathrm{mag}}$ are the energies in the $m = 0$ and $m = 1$ magnetic field modes, respectively.

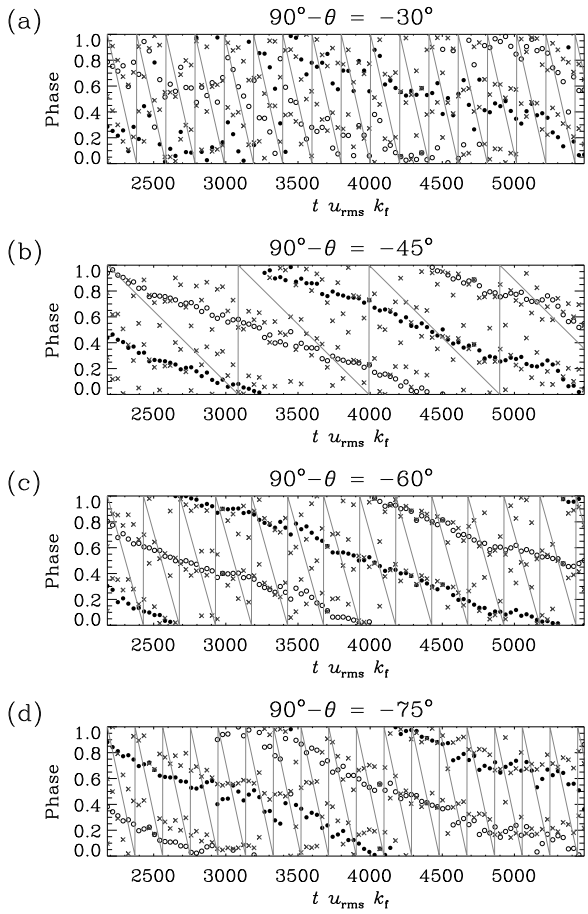

Figure 7.5: Phase of the $m = 1$ mode of radial magnetic field at the surface over time (open and filled circles) at various latitudes. The maxima of the $m = 2$ mode for temperature is plotted with crosses. Solid lines indicate the speed if the structure was carried by pure advection. From Paper II.

in this table are identical to the ones in Table 7.1. Runs A and C explore the azimuthal dynamo wave found in Run B with slightly lower and higher rotation rates, respectively. The large-scale magnetic field is initially axisymmetric, but as it grows, a stable non-axisymmetric mode takes over and propagates in the ϕ-direction.

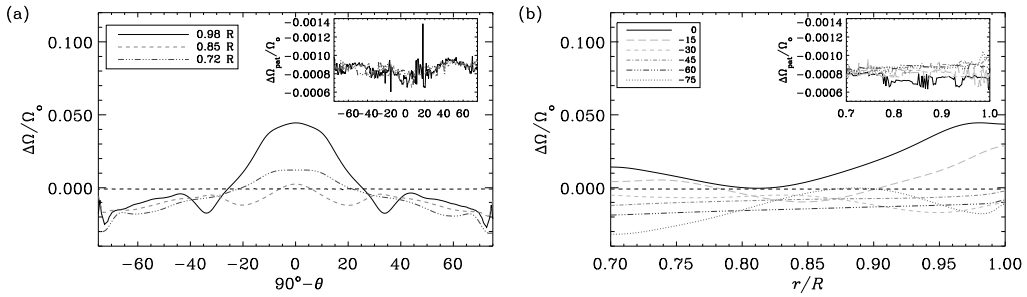

Figure 7.6: Differential rotation averaged over time at various latitudes (a) and depths (b). The inset is the zoom up of the almost-flat dashed line near 0. From Paper II, Figure 4.

Table 7.4 has some of the select output diagnostics from the Runs. $\mathcal{M}$ is nearly 1 as the high m modes dominate the total energy. The parity $\mathcal{P}$ increases as the rotation rate increases.

The structure's phase speed was calculated by determining the azimuth ϕ of the magnetic extrema of the $m = 1$ mode at each snapshot in time. The initial angular velocity is uniform, but the simulation develops differential rotation and the final rotation profile is averaged from the azimuthal component of the velocity and the uniform rotation of the frame, Ω_0. By comparing the phase speed and advection due to differential rotation (Fig. 7.5), it can be seen that the pattern speed is slower than the local flow at various latitudes, although the local flow itself varies in latitude due to differential rotation.

Areas with strong magnetic flux are expected to inhibite convection and lower the temperature. Therefore one would expect to find an $m = 2$ mode for the temperature with the same phase as the the dynamo wave. This is shown in Figure 7.5, where the temperature maxima is plotted with the radial magnetic flux extrema. This relationship is particularly clear at the mid-latitudes. Although one would expect the minima to correspond if the magnetic field inhibited convection, for whatever reason, the maxima of the temperature structure were closer in phase to the extrema of the $m = 1$ mode of the magnetic field.

The phase speed of the $m = 1$ mode is largely independent of both latitude and depth, unlike the azimuthal velocity component of the flow. Figure 7.6 shows the azimuthal velocity component, with the black dashed line showing the relative phase speed of the pattern. The inset enlarges this, as the pattern speed is very small

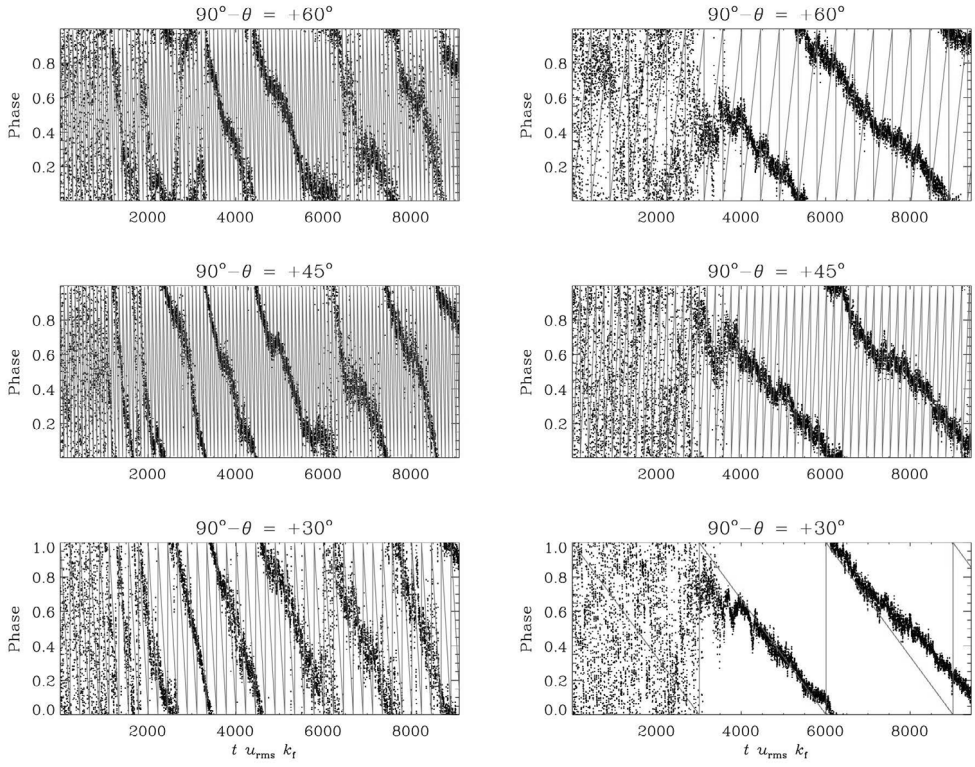

Figure 7.7: The phase speed of the azimuthal dynamo wave for Runs A (*left*) and C (*right*) from Paper II. The points denote the maxima of the magnetic field and stolid lines are the speed of the local fluid.

relative to the speed of the advection. This slower rotation of the pattern relative to the mean rotation provides a potential explanation for observed tendency for active longitudes to rotate with a different period than the star itself. The azimuthal dynamo wave rotates as a rigid body, independent of depth or latitude.

It was also found that the parity changed with an increasing Co from solutions that tended towards being consistently antisymmetric to more symmetric about the equator, although all runs at all times had mixed equatorial symmetry. For models with a higher Co, the pattern also changed speed over time, albeit very slowly, and so it is possible that solutions exist where the azimuthal dynamo wave rotates faster

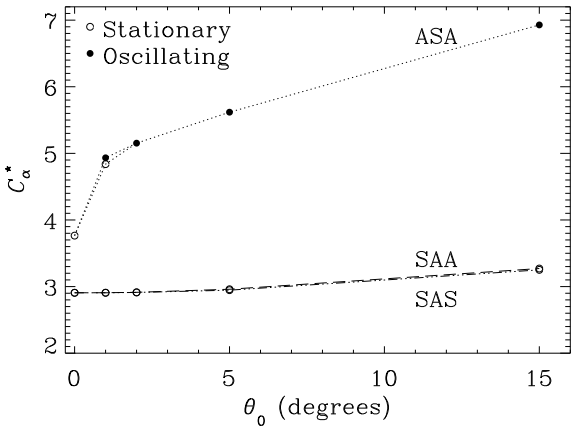

Figure 7.8: Dependence on $C_\alpha^\star$ for marginally excited dynamos on the latitudinal extent and boundary condition. From Paper III, Figure 1.

than the surrounding fluid. Figure 7.7 shows the result of slower rotation on the left, corresponding to Run A, and faster rotation on the right, corresponding to Run C.

In stars such as II Peg (Lindborg et al., 2013), for example, a persistent active longitude is observed for a period over ten years, rotating slightly faster than the mean rotation period. A systematic study of photometry of rapidly rotating active solar analogs over long periods by Lehtinen et al. (2016) finds similar cases where rotation periods of spot structures are shorter than the rotation period of the star, suggesting the presence of azimuthal dynamo waves. From Figure 7.7, it can also be seen at least in the early stages that some faster rotation is also possible for short times in the rotation regime covered in Paper II.

7.1.3 α^2 Dynamos in 1D Mean-field Models

In Papers I and II, one significant problem with the simulations is the imposed latitudinal boundary condition. Because the phase relation of B_r and B_ϕ near the surface matched that of α^2 dynamos and not $\alpha\Omega$, it cannot be assumed that the findings of Jennings et al. (1990) hold true. The boundary is at co-latitudes of $\theta_0 = \pm 15^\circ$ to avoid the singularity at the axis where the time step would approach zero, but cross-polar effects are lost. Additionally, it can be seen in Figure 7.1 that the magnetic field is strong near the latitudinal boundary and in Figure 7.5 (d) that

Table 7.5: $C_\alpha^\star$ for α^2 dynamos with varied η_t and α profiles.

		$\boldsymbol{a}$		
		(1,0,0)	(0,1,0)	(0,0,1)
e_i	e_0	$C_\alpha^\star$	$C_\alpha^\star$	$C_\alpha^\star$
e_2	0.01	0.236*	4.063	9.532
e_2	0.05	0.558*	5.308	11.39
e_4	0.01	0.096	1.045	4.144
e_4	0.05	0.326*	2.587	7.039
e_6	0.01	0.070	0.541	2.175
e_6	0.05	0.265*	1.733	4.857
e_8	0.01	0.059	0.403	1.463
e_8	0.05	0.238*	1.384	3.727

Notes. An asterisk (*) indicates stationary dynamos. All other runs are oscillatory. $\theta_0 = 0°$ and the latitudinal boundary condition is SAA for all runs. Modified from Paper III, Table 1.

the structure is also fairly distinct at the boundary. This leads to the possibility that the structures at higher latitudes and oscillations there are merely artifacts created by the latitudinal boundary condition.

Paper III concentrates mainly on the two possible boundary conditions, the perfect conductor ASA and the normal field SAA (Section 4.2.1, Table 4.1). Figure 7.8 demonstrates the discontinuity when a simple 1D α^2 dynamo is extended to the poles with the ASA boundary condition. $C_\alpha^\star$ is the critical dynamo number such that the solution is neither decaying nor growing, from Equation 4.8. Even changing the latitudinal boundary from $\theta_0 = 2°$ to $\theta_0 = 1°$ for the ASA boundary condition creates inconsistent results where both an oscillatory and stationary dynamo are possible. No boundary condition creates oscillations at $\theta_0 = 0°$. Thus the limit is a singularity, in the sense that as $\theta_0 \to 0°$, the resulting dynamo changes from oscillatory to stationary. It is possible that the isotropic α effect with the perfect conductor boundary condition cannot represent a full sphere as the solution is dependent on θ_0. The SAA and SAS boundary conditions had a similar value for $C_\alpha^\star$ for all θ_0 in Figure 7.8, but all dynamo solutions were found to be stationary.

One possible method to obtain oscillatory solutions for α^2 dynamos is to alter the α effect and magnetic diffusivity η_t. The α and η_t profiles can be varied as a function of latitude, motivated by previous convection simulations (Käpylä et al., 2009, Figure 8), as well as earlier results by Ossendrijver et al. (2002) and Käpylä

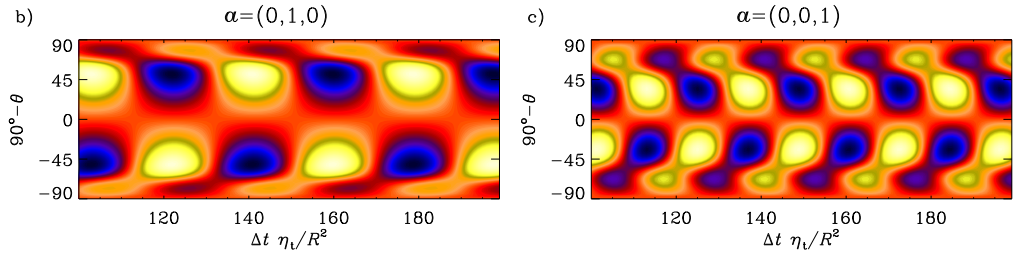

Figure 7.9: Azimuthal magnetic field with varied α and turbulent diffusivity profiles. From Paper III, Figures 4b and c.

et al. (2006). Table 7.5 shows the values selected in terms of Equations 4.10 and 4.11. Vector notation is used for the coefficients of the equation of the α profile, where $\boldsymbol{a} = (a_0, a_2, a_4, \ldots, a_n)$. The perfect conductor boundary condition is then mimicked by a normal field condition imposed at the pole and profiles that concentrate η_t and α at lower latitudes. Figure 7.9 shows the resulting azimuthal magnetic flux when $\eta_\mathrm{t} = e_4$ and $\boldsymbol{a} = (0, 1, 0)$ (left) and $(0, 0, 1)$ (right). The solutions both oscillate and exhibit equatorward migration of the magnetic flux. The magnetic field is largely confined to middle or lower latitudes. Thus it seems possible to obtain oscillatory solutions with equatorward migration instead of the stationary solutions shown in Figure 7.8 with models where α and η_t are concentrated at lower latitudes. These results agree with the DNS simulations by Käpylä et al. (2012) as well as Papers I and II, and the LES simulations by Augustson et al. (2015) and Duarte et al. (2016).

Shear is also introduced so that the resulting dynamo is of the $\alpha^2\Omega$ type. Figure 7.10 shows two different set-ups with varying C_Ω and $C_\alpha^\star$ and the damping term $\tilde{\mu} = \mu R^2/\eta_{\mathrm{t}0}$. A bifurcation exists in the $\tilde{\mu} = 1$ branch, where the dynamo is marginally exited for two values of $C_\alpha^\star$. There is an oscillatory branch at higher values for $C_\alpha^\star$ when $C_\Omega \gtrsim 33.6$, and a stationary branch at all C_Ω. This bifurcation exists for both $\theta_0 = 1°$ and ASA boundary condition and $\theta_0 = 0°$ and SAA boundary condition. The upper branch of oscillatory solutions for $\tilde{\mu} = 1$ has a small increase in the $C_\alpha^\star$ around $C_\Omega \approx 70$. This corresponds to an increase in the frequency of the oscillations as well as a change from antisymmetric solutions about the equator to symmetric ones (see Figs. 8, 9, and 10 in Paper III). The plots of the azimuthal magnetic fields are similar for both cases of $\theta_0 = 1°$ and $0°$, with the exception that the magnetic field is strongest near the latitudinal boundaries with the ASA boundary condition, whereas the magnetic field is concentrated at lower latitudes

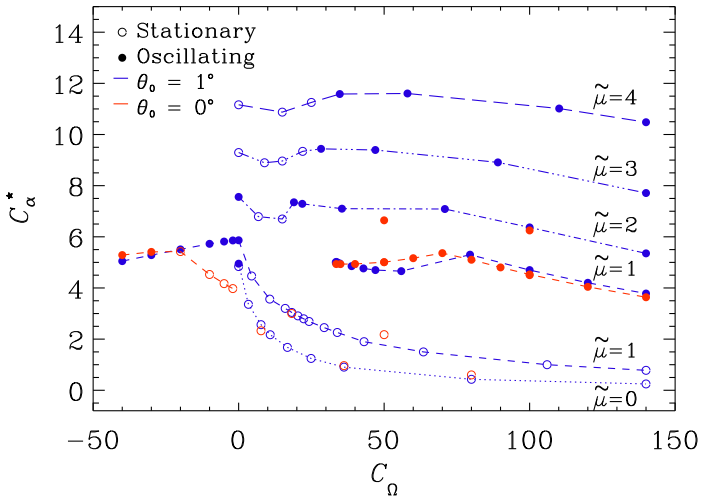

Figure 7.10: Critical values for α as a function shear. Oscillatory (filled circles) and stationary (open circles) solutions for both $\theta_0 = 1°$ (blue) and $\theta_0 = 1°$ (red). From Paper III, Figure 7.

with the SAS boundary condition. The dynamo propagates poleward when shear is positive, in accordance with the Parker-Yoshimura rule. When negative shear is added, the latitudinal dynamo wave propagates towards the equator. Thus it would seem that with the exception of a region of negative shear where $-20 < C_\Omega < 0$, the ASA and SAA boundary conditions produce almost identical results in terms of oscillatory fields. However, with the change in the boundary condition from ASA and $\theta_0 = 1°$ to SAA and $\theta_0 = 0°$, the field becomes concentrated at lower latitudes, but still oscillates. And so the wedge is found to be a good approximation of a full sphere under certain conditions.

7.2 Observations

7.2.1 Photometry of V352 CMa

In Paper IV the CPS method is used to evaluate the usefulness of the method for stars with low-amplitude changes in the light curve. The CPS method proves to

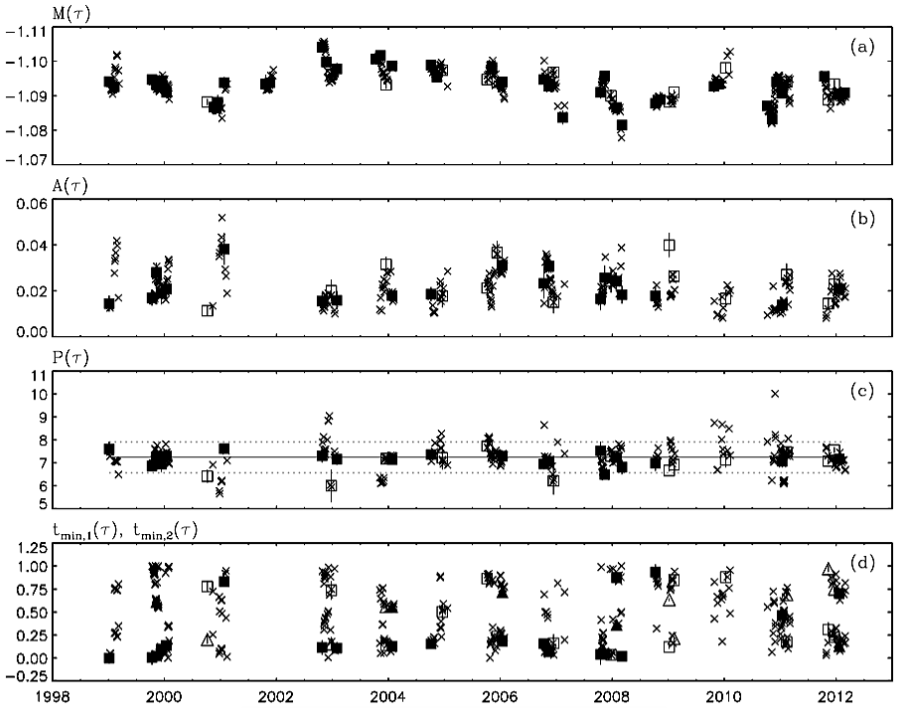

Figure 7.11: The calculated mean (a), amplitude (b), period (c), and phases (d) of the primary and secondary minima of V352 CMa. Filled triangles and squares indicate reliable and independent datasets, open triangles and squares are independent and unreliable datasets, and crosses indicate non-independent datasets. The dotted lines for the period indicate the $3\Delta P_W$ period range. From Paper IV, Figure 3.

be robust, and the calculated mean period is $P_0 = 7\overset{\mathrm{d}}{.}24 \pm 0\overset{\mathrm{d}}{.}22$, while an active longitude persisting between 1998 and 2009 with $P = 7\overset{\mathrm{d}}{.}158 \pm 0\overset{\mathrm{d}}{.}002$ is found via the Kuiper test (Jetsu and Pelt, 1996). The possible active longitude disappears when the light curve amplitude variation reaches its minimum in 2010. An activity cycle of 11.7 ± 0.5 years was calculated from the mean brightness M of the light curve.

Figure 7.11 shows the parameter solutions for data subsets for the mean of the light curve, $M(t)$, amplitude $A(t)$, period $P(t)$, and primary and secondary minima $t_{\mathrm{min},1}$ and $t_{\mathrm{min},2}$, respectively, folded by the period $P = 7\overset{\mathrm{d}}{.}158$. The fluctuations of the weighted period mean, $P_W \pm \Delta P_W$, can be used to estimate differential rotation

assuming the differences in period are due to spots at different latitudes and the star has a solar-like differential rotation profile. From the maximum range of change, we find $Z = 6\Delta P_W/P_W = 0.19$. If the estimation of spurious fluctuations of the period is $Z_{\rm spur} \geq 0.15$ due to the low amplitude to noise ratio, the physical fluctuation is estimated as $Z_{\rm phys} = 1/(Z^2 - Z_{\rm spur}^2)^2 \approx 0.12$. The differential rotation $|k| > Z_{\rm phys}$ is a lower limit, as it is unknown at which latitudes the spots form. If they are restricted to narrow latitudinal bands, the real value for $|k|$ would be greater.

This star was revisited in Lehtinen et al. (2016), with the addition of two more years of photometry. No statistically significant cycle could be found in M using the CPS method and including additional observations. However, an 8.1 year cycle was found using the amplitude data, but this result had a false alarm probability rating of "poor" following the rating scheme of Baliunas et al. (1995). It would seem that the cycle found in Paper IV was stable only within the time period of observations. Lehtinen et al. (2016) also found a stable active longitude rotating with a period of $7\overset{\rm d}{.}132$. The value for the period fluctuation range was similarly close, with $Z = 0.22$. Thus it would seem that the activity cycle itself is chaotic or the length of observations is too short. However, V352 CMa still shows a spot structure that consistently rotates faster than the mean photometric rotation period with the newer data. If the differential rotation is the cause of these period fluctuations, then it is comparable to that of the Sun ($Z \sim 0.2$). Lehtinen et al. (2016) classified this star as being on the active branch, with a $\log R'_{\rm HK} \approx -4.43$.

Based on the observational parameters (Table 2.1), V352 CMa is a young solar analog, with a rotation rate over three times faster than the Sun. Using Equation 4 in Noyes et al. (1984) with a $B-V$ of 0.71 yields a convective turnover time $\tau_c = 15.3$ days. Then the calculated Co = 26.6, which is higher than the Co of Run C but still reasonably close. With respect to the rotation rate, this star most closely matches the rotation rate of Run B of Paper II. In both Runs B and C, the azimuthal dynamo wave was fairly constant over time. This makes it an interesting object to compare with the numerical simulations in Papers I and II, as the rotation rates for some of those simulations are quite similar, and this star should have a convection zone depth similar to the setup of the numerical models. It seems possible that the observed light curve variation for this star might be due to an azimuthal dynamo wave, described in Paper II, or some competition between a dynamo wave and differential rotation.

7.2.2 Photometry of LQ Hya

The CF method is used in Paper V to determine the carrier period and its modulations from the photometry of the variable star LQ Hya. The accurate determination

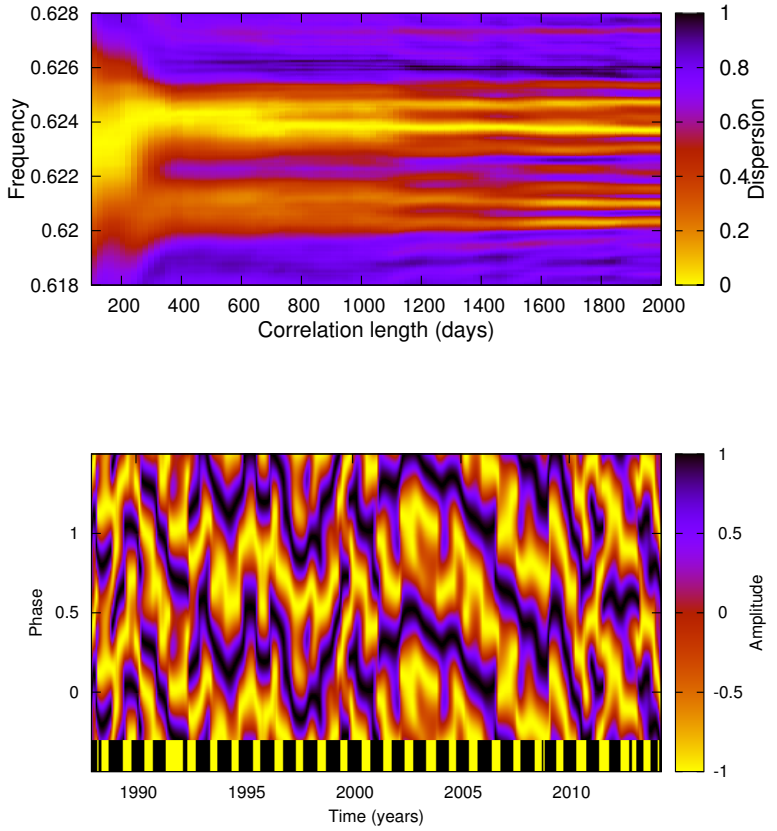

Figure 7.12: *Top*: Phase dispersion relation plotted against various correlation lengths. *Bottom*: Phase diagram with carrier period $P_0 = 1\overset{\text{d}}{.}60514$. From Paper V, Figures 6 and 8.

of the most plausible carrier period allows the tracking of flip-flops and possible azimuthal dynamo waves. 27 time segments in total are used, ranging from December 1982 to May 2014. The overlap and individual datasets are shown in Figure 1 of Paper V. The periodicity analysis and optimal carrier period analysis used this full dataset. Only the data from Lehtinen et al. (2012) and Paper V was used in the CF

analysis as these subsets of observations all used the same instrument with the same comparison star, thus making a homogeneous dataset.

Figure 7.12 (left) shows the $D^2(P)$ statistic (Eq. 5.11), and demonstrates the dispersion of the various detected frequencies. The correlation time in days corresponds to how long a frequency persists. For a correlation length less than 200 days, a single minima exists. However, for longer correlation lengths the dispersion relation splits into two main peaks and the frequency spectrum further distorts at even longer correlation lengths. Thus active longitudes do not persist for more than a year. The optimal correlation time Δt is found by fitting a Gaussian to the D^2 statistic. The longest correlation length for which the statistic remains singular and mostly symmetric is 100 days. This results in a $P_0^{D2} = 1\overset{\mathrm{d}}{.}60514$, with a deviation of $\Delta P_0^{D2} \approx 0\overset{\mathrm{d}}{.}9984$. This is similar to the mean rotation period $P_W = 1\overset{\mathrm{d}}{.}6043$ of Lehtinen et al. (2012). The selected P_0^{D2} is the most statistically significant rotation period of the dispersion function for the carrier fit over the entire time span. The other values from, for example, the peaks at longer correlation times, are most likely due to some locally active period over a shorter time span than the entire dataset, and therefore are not optimal to use to analyze the entire time span.

Figure 7.12 (right) shows a fit of normalized amplitudes with a calculated period of $P_0 = 1\overset{\mathrm{d}}{.}60514$, with the harmonic order limit $K = 2$ (Eq. 5.10) and $L = 30$ (Eqns. 5.12 and 5.13). Visually, the slopes of the lines correspond to deviations from the carrier period. Downward trends indicate a spot structure that rotates faster than the rotation period of the star, and an upward trend indicates a slower rotation period of the spots. Unbroken trends may be indicative of azimuthal dynamo waves (Paper II). The downward trend from 1990–1994 corresponds to a period of $1\overset{\mathrm{d}}{.}6033$, and the downward trend from 2003–2009 corresponds to a period of $1\overset{\mathrm{d}}{.}6037$. With the exception of these two epochs, the phase behavior appears to change rapidly, and even these two trends show fluctuations. This can be compared to, for example, the binary star II Peg (Lindborg et al., 2013, Figs. 2 and 4), where the rotation period of the spots could instead be well-constrained for a decade and appeared as a steady downward trend.

A flip-flop is defined in two ways: either the region of main activity (primary minimum) switches by about 180° and then remains there for some time, or a primary and secondary minima separated by approximately 180° switch and the secondary, which has now become the primary minimum, remains for some time. Four flip-flop events were detected in the dataset, and three additional possible events occurred in data gaps between observations. The CPS method from Lehtinen et al. (2012), the CF method from Paper V, and DI method from Paper VI are combined in Figure 7.13. Possible flip-flop events are marked by vertical green lines. It is apparent that

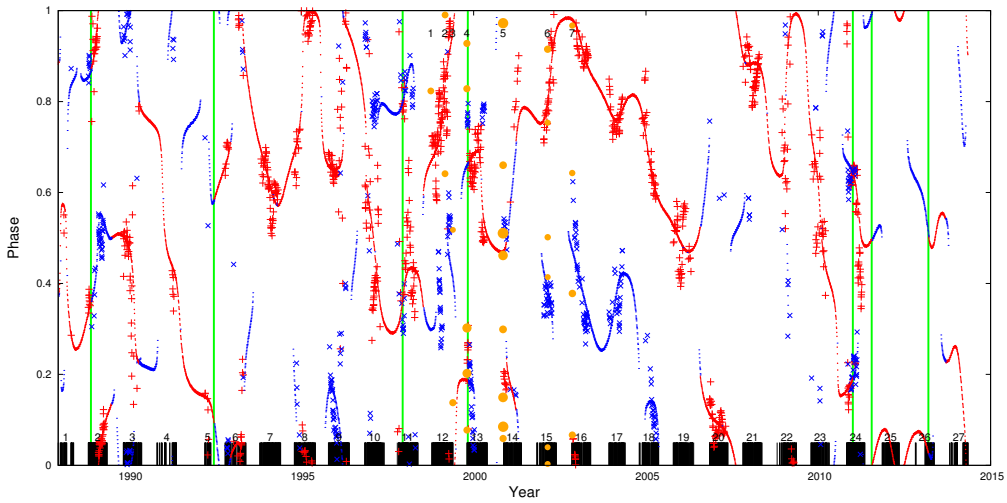

Figure 7.13: Phases of minima and cool spots from Lehtinen et al. (2012) (crosses and pluses), Paper V (small dots), and Paper VI (larger filled circles). The vertical green lines indicate possible times of flip-flops. The black bars along the x-axis show the times of photometric observations. (Paper V, Fig. 10).

even with a time span of 22 years, no regular cycle can be observed. This is too few events to calculate a flip-flop cycle, and the CF method does not recover the 5.2 year flip-flop cycle reported by Berdyugina et al. (2002).

The differential rotation coefficient k was found to be quite small, $k \approx 0.032$. Estimates for differential rotation from Doppler imaging are even smaller, of the order of 0.006 (e.g., Kovári et al., 2004). These seem well in agreement with previous estimates using photometry (Jetsu, 1993; You, 2007; Lehtinen et al., 2012, 2016). The period fluctuations could be due to differential rotation, if spots were drifting from high latitudes to low latitudes. The maximum spot range in one hemisphere versus the mean latitude is of the order of 45°, implying that the drift of the spot structures is roughly half the differential rotation parameter, so that $k_{\rm dr} \approx 0.5k$. If one calculates $k_{\rm dr}$ from the period difference of the coherent structure $P_{\rm coh}$ from the mean period, then $k_{\rm dr} = (P_0 - P_{\rm coh})/P_0 \approx 0.0011$. Thus it is somewhat possible that spot drift and differential rotation are responsible for the observed period fluctuations, although an

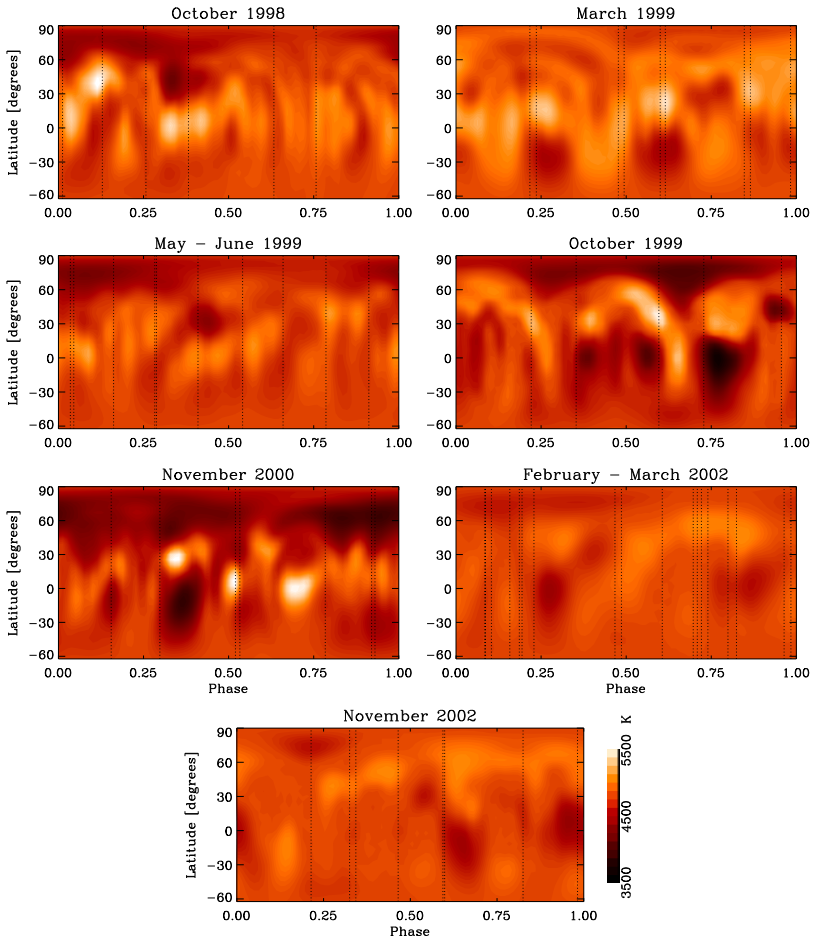

Figure 7.14: Temperature maps of seven seasons for LQ Hya. From Paper VI, Figures 1-7.

azimuthal dynamo wave may certainly also explain this.

7.2.3 Doppler Imaging of LQ Hya

Figure 7.14 shows the temperature maps of the seven observing seasons, spanning over four years. The summary of the observations is listed in Table 1 in Paper VI.

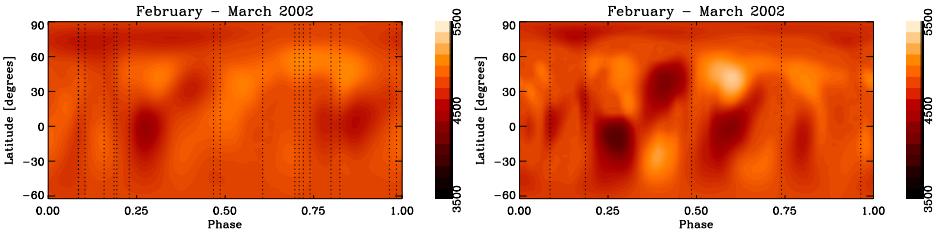

Figure 7.15: *Left:* Temperature map with all 18 observations. *Right:* Temperature map with only five selected observations.

October 1998 and March 1999 both show a low activity level. There are few spots, and some artifacts are present, likely due to the low S/N. Some spot activity becomes evident during May–June 1999. A higher level of activity is seen during October 1999 and November 2000, however, these maps also had poorer phase coverages of about 50%. Vogt et al. (1987) found that poor phase coverage does not create spurious spots, but may increase temperature contrast and reduce the spot shape resolution. Some artifacts are also apparent in the recovered images in the form of arches and bright spots near dark spots.

One thing that can be immediately seen from the observation summary (Paper VI, Table 1) is that at least three seasons had very poor phase coverage (March 1999, October 1999, and November 2000). While S/N was mitigated by using several spectral lines in the analysis to cancel the noise, not much can be done to minimize the effects of poor phase coverage. Instead, it is more useful to examine the impact that poor phase coverage has on the inversion. Other seasons have much better coverage. February–March 2002, with a good coverage and over 18 observations, was used to examine the effect of removing 13 observations from the inversion, leaving five approximately evenly spaced observations with which to perform the inversion. From Figure 7.15, it can be seen that reducing the phase coverage does not introduce spurious spots, in agreement with Vogt et al. (1987) and Rice and Strassmeier (2000). A similar analysis had been done with observations of the star DI Piscium by Lindborg et al. (2014). The authors used a season with the good coverage and removed all but five observations so that the phase coverage was 50%. Similarly to our February–March 2002 season, their July–August 2004 observations originally found a slightly cool spot at some phase that appeared much cooler when the phase coverage was poorer. This is similar to the behavior of the spot at the phase 0.6 in Figure 7.15 (left), which appears as a cooler spot with a hot spot at the same phase (right) with

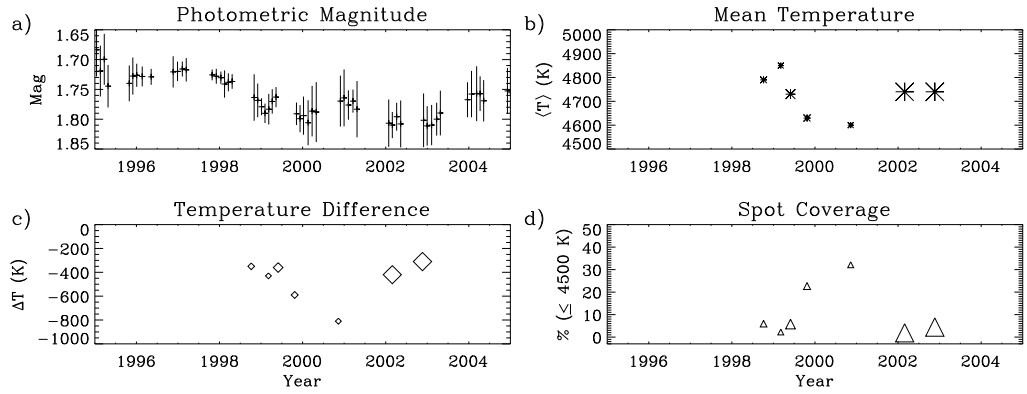

Figure 7.16: Mean photometric magnitudes from Lehtinen et al. (2012) (a), mean temperatures of maps calculated from each observing season (b), temperature differences (c), and spot coverage (d). Symbol size is proportional to the S/N and phase coverage (Paper VI, Fig. 8).

poorer phase coverage. The temperature contrast increases while the mean temperature remains approximately the same, and spot coverage correspondingly increases from 1.9% to 9.3%. It would seem that poor phase coverage mainly affects the spot temperature, and to a lesser degree affects the shape due to lack of observations at certain phases. However, some information such as spot latitudes for spots near in phase to the observations is still useful.

Figure 7.16 shows the general trends over all observing seasons. The first panel displays photometric magnitudes with error bars, showing a general decrease in magnitude during the time period of the DI observations. According to the theory of stellar activity, a decrease in magnitude should correspond to an increase in activity level due to the large spots covering the surface. However, it appears that the process on LQ Hya is more complex as the photometric brightness shows a slight increase during the time when the average temperature shows a consistent low point. This could be partially due to the limited time-span of the observations.

Activity cycle estimates range from 3.2 years (Messina and Guinan, 2003), to as high as 18 years (Lehtinen et al., 2016), with the most agreement in the 6–7 year range (Jetsu, 1993; Strassmeier et al., 1997; Cutispoto, 1998; Oláh et al., 2000; Alekseev, 2003). Thus only four years of observations cannot give insight into any possible activity cycle, and the only thing that can be concluded is that the spots

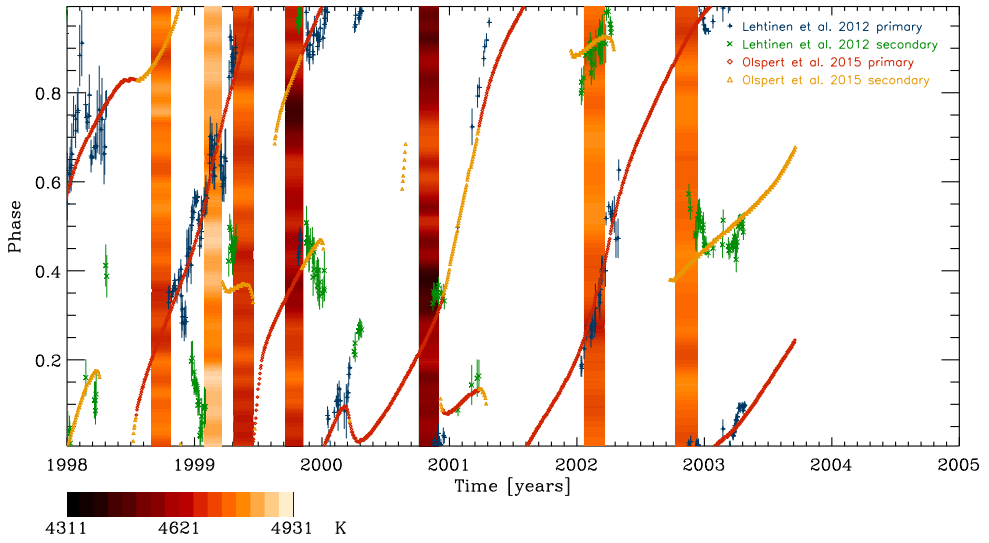

Figure 7.17: Latitudinally averaged temperature maps for seven observing seasons along with primary and secondary minima from Lehtinen et al. (2012) and Paper V (Paper VI, Fig. 9).

evolve quickly over a short time.

Figure 7.17 is similar to Figure 7.13, but uses a different phase corresponding to the rotation period found by Jetsu (1993), $P_{\mathrm{CPS}} = 1\overset{\mathrm{d}}{.}6001136$, compared to the period found through CF analysis, $P_{\mathrm{CF}} = 1\overset{\mathrm{d}}{.}60514$. The spot phases from DI coincide fairly well with the photometric minima, even for seasons with poor phase coverage. From both Paper V and Paper VI, it is evident that LQ Hya has a rather chaotic spot evolution, and no evidence for persistent active regions following a single rotation period could be found during the time span of the observations. This fits with the result of a correlation time for a rotation period of 100 days or less. The higher activity season October 1999 coincides with a flip-flop found via the CF method, but some caution must be used when viewing the temperature map, as October 1999 had the poorest phase coverage, which as demonstrated earlier, leads to an overestimated temperature contrast. Given though that the spot latitude results are somewhat reliable, it can be seen that spots have some bimodal nature in which they appear both at high and low latitudes, but not so much at mid-latitudes. This is in

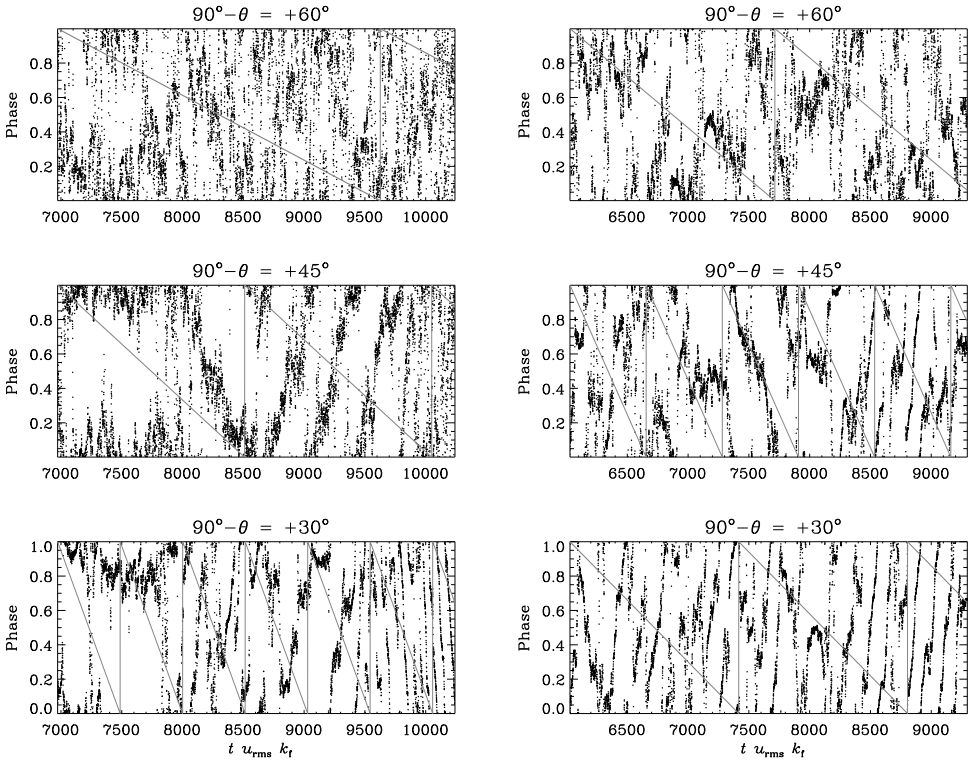

Figure 7.18: Numerical simulations of spherical wedges, the same as Figure 7.7, but with rotation rates 15 (*left*) and 29 (*right*) times the solar rotation rate.

agreement with other DI and ZDI results for LQ Hya (e.g., Strassmeier et al., 1993; Rice and Strassmeier, 1998; Donati, 1999; Donati et al., 2003b; Kovári et al., 2004).

LQ Hya is considered a super-active star, with an $R'_{\rm HK} > -4.20$, but was also noted as being anomalous by Saar and Brandenburg (1999) as it exists in the transition region between the active and super-active branches. This could partly be due to its status as a single star, where magnetic cycles potentially do not evolve at the same rate as they do in binary systems (Saar and Brandenburg, 1999). This makes it a very interesting object. The star has a rapid rotation period of 1.6 days, low differential rotation, and estimated convective turnover time of $\tau_c \approx 21$ days, corresponding to a Co ≈ 160, using the definition for the Coriolis number from Noyes

et al. (1984). Thus the Coriolis force dominates (Saar and Brandenburg, 1999, Table 2). The rapid evolution of spots may be due to differential rotation, but since this differential rotation is very weak, complex azimuthal dynamo waves affecting the spot-generating mechanisms provides a possible alternative. The simulations of Paper II have a slower rotation rate than LQ Hya. While the azimuthal dynamo wave of the models presented in Paper II are relatively well-behaved for the three selected rotation rates, simulations with similar parameters but much faster rotation show much more chaotic behavior for the azimuthal dynamo wave, as shown in Figure 7.18. The rotation rate of Figure 7.18 (left) is approximately the same as that of LQ Hya. LQ Hya would lie within this very rapidly rotating regime, and it can be seen that any active longitudes connected to an azimuthal dynamo wave at this rotation rate would not create steady trends for the CF method nor long-term persistent drift in the Doppler images.

8 Summary of the publications

The thesis consists of six peer-reviewed journal publications. These are grouped by topic instead of chronological order. Papers I–III focus on numerical results and theory, while Papers IV–VI focus on observational results.

- **Paper I:** Käpylä, P. J., Käpylä, M. J., **Cole, E.**, Warnecke, J., and Brandenburg, A., 2013, "Effects of Enhanced Stratifcation on Equatorward Dynamo Wave Propagation." The Astrophysical Journal, 778, 41
- **Paper II: Cole, E.**, Käpylä, P. J., Käpylä, M. J., and Brandenburg, A., 2014, "An Azimuthal Dynamo Wave in Spherical Shell Convection." The Astrophysical Journal Letters, 780, L22
- **Paper III: Cole, E.**, Brandenburg, A., Käpylä, P. J., and Käpylä, M. J., 2016, "Robustness of oscillatory α^2 dynamos in spherical wedges." Astronomy & Astrophysics, 593, A134
- **Paper IV:** Kajatkari, P., Jetsu, L., **Cole, E.**, Hackman, T., Henry, G. W., Joutsiniemi, S.L., Lehtinen, J., Mäkelä, V., Porceddu, S., Ryynänen, K., and Şolea, V., 2015, "Periodicity in some light curves of the solar analogue V352 Canis Majoris." Astronomy & Astrophysics, 577, A84
- **Paper V:** Olspert, N., Käpylä, M. J., Pelt, J., **Cole, E. M.**, Hackman, T., Lehtinen, J., and Henry, G. W., 2015, "Multiperiodicity, modulations, and flip-flops in variable star light curves. III. Carrier fit analysis of LQ Hydrae photometry for 1982-2014." Astronomy & Astrophysics, 577, A120
- **Paper VI: Cole, E. M.**, Hackman, T., Käpylä, M. J., Ilyin, I., Kochukhov, O., and Piskunov, N., 2015, "Doppler imaging of LQ Hydrae for 1998-2002." Astronomy & Astrophysics, 581, A69

The papers are summarized in the following sections. The author's contribution to the papers is described at the end of each section.

8.1 Paper I

This paper explores the dependence of 3D dynamo simulations on density stratification and rotation rates in spherical wedges. This paper also explores the use of a sub-grid scale turbulent heat conductivity to numerically stabilize the model and a modified blackbody boundary condition so that the flux near the upper boundary is comparable to that needed to carry the total luminosity through the surface of the model. This also allows the temperature at the surface to vary and therefore serve as a possible measure for irradience with time. The Taylor number, and by extension Coriolis and Reynolds numbers are varied to explore the different activity regimes of the resultant dynamos.

Almost all simulations initially develop a higher-frequency oscillatory magnetic field with poleward migration that is eventually dominated by other lower-frequency or quasi-stationary dynamo modes. When the initial density stratification is low, the resulting dynamo at the saturated state is irregular and the dynamo propagates poleward. However, as density stratification and the Prandtl number increase to approximately 30 and 2.5 respectively, an equatorward oscillatory dynamo dominates. The cyclic activity of all oscillatory solutions is roughly categorized as inactive, active, and super-active to compare to parameters such as rotation rates, cycle frequencies, and the ratio of magnetic to kinetic energies. However, the models provide too few data points to plot an analog to the activity branches observed for active stars. Temperature fluctuations for Run C1 were found to be around 15–20%. The rotation rates of the runs are around 2-7 times the solar rotation rate, and the resulting dynamo type appears to be α^2 based on the phase relation between the radial and azimuthal magnetic field near the surface.

Run C1, which had oscillatory equatorward dynamo migration is extended to the full 2π in the longitudinal direction, resulting in a transition from axi- to non-axisymmetric solutions as predicted by mean-field theory. The resulting azimuthal magnetic field near the surface at low and high latitudes has a strong non-axisymmetric component of the mode $m = 1$ in terms of spherical harmonics. This non-axisymmetry is similar to the observations of field configurations of rapidly rotating late-type stars.

The author was responsible for the analysis of the runs extending over full azimuthal direction, and the writing of the results concerning them. During the data analysis of Paper I, for the first time, the behavior consistent with an azimuthal dynamo wave was observed, which the author further explored in Paper II. The parameters and setup for Paper II were developed based on the knowledge gained during writing Paper I.

8.2 Paper II

Paper II takes the model for Run E4 from Paper I and studies the resulting azimuthal dynamo wave for similar cases where the model rotates slightly slower or faster, covering a range of about 2–5 times the solar rotation rate. Run B in this Paper corresponds to Run E4 in Paper I. Initially, a large-scale axisymmetric oscillatory magnetic field grows, followed by the non-axisymmetric dynamo mode which dominates as the axisymmetric portion ceases to oscillate. Parity is found to increase as rotation is increased, corresponding to increased symmetry at the equator, as predicted by theory. A dynamo wave for the $m = 1$ mode is found for all 3 models. The azimuthal dynamo wave was found to rotate slower than the mean rotation in all cases, with a nearly constant rotation rate independent of latitude or depth. The rotation speed of this pattern decreased monotonically as a function of fluid rotation rate. The extrema for the $m = 1$ mode of the magnetic field could also be mapped to an $m = 2$ mode for temperature. Temperature fluctuations were around 2–5%. Results are used to explain a possible cause of the observed discrepancy between active longitudes and mean stellar rotation rates on rapidly rotating late-type stars such as II Pegasi.

The author had the main responsibility of producing the simulation runs, performing the data analysis, and the writing of the manuscript.

8.3 Paper III

Paper III examines the impact of the latitudinal boundary condition on spherical and wedge geometry. The model used in Paper III is 1D with only latitudinal extent and solves the mean-field dynamo equations. Because the models of Paper I and II have artificial boundary conditions in latitude due to computational limitations, the latitudinal boundary condition may have some effect on the final results of such simulations by producing artifacts. Both α^2 and $\alpha^2\Omega$ dynamos are considered.

To examine the difference between using a wedge versus the full sphere, the angle between the pole and latitudinal boundary θ_0 was varied with various boundary conditions for an α^2 dynamo. The boundary conditions tested are the perfect conductor, regular field, and normal field at the boundary. θ_0 is varied between 0°–15° and a discontinuity is found with the perfect conductor boundary condition where oscillatory solutions changes to a stationary solutions as θ_0 approaches 0°. Both the normal field and regular field boundary conditions can only produce stationary solutions. Oscillatory solutions are possible when the magnetic diffusivity η_t and α profiles are modified to be concentrated towards the equator. These profiles remove

the artificial θ_0 dependence, and resemble the dependence of η_t and α on latitude found in numerical simulations.

Radial shear and a damping term is then added to the mean-field equation. Oscillatory solutions are only possible when the damping term is not zero. Models with $\theta_0 = 1^\circ$ and the perfect conductor boundary condition, and θ_0 and the normal field boundary condition are examined with both positive and negative shear. Oscillatory solutions were found within certain shear regimes for both cases. For certain values of the damping term, both oscillatory and stationary solutions were possible, depending on the critical α number. The Parker-Yoshimura rule was obeyed in all instances of oscillatory dynamo waves. Thus it would seem that wedges are a good approximation for the full spherical domain under certain conditions for α^2 and $\alpha^2\Omega$ dynamos.

The author was responsible for running the numerical models, determining critical dynamo numbers, analyzing the results, and creating the figures. The work in this paper is the result of a visit to Nordita in Stockholm, Sweden. While revising the manuscript for Paper II during this visit, a question regarding the impact of the latitudinal boundary on oscillatory solutions was raised, inspiring this paper. The author was also responsible for writing the manuscript.

8.4 Paper IV

Paper IV is an introduction into observing methods for solar analogues. The target star V352 Canis Majoris is selected due to its lack of prior modeling attributed to the low amplitude of the light curve. The CPS method is used to search for evidence of a longer cycle and results are compared to results obtained via the power spectrum method. The mean rotation period of the star is found to be 7.24 ± 0.22 days. A lower limit for the differential rotation coefficient $|k| > 0.12$ is found assuming a solar rotation law. A cycle of 11.7 ± 0.5 years is found in the mean brightness. Possible stable active longtitudes were found during years 1998–2009, rotating with a period of 7.157 ± 0.002 days. The CPS method proved robust for this star. The light curve data was published online.

The author contributed to some of the collection of parameters in the literature for the target star. The author also performed most of the CPS and power spectrum method calculations to refine the rotation period and estimate a possible activity cycle. This paper was part of the course "Variable Stars" at Helsinki University. The author also contributed to writing the manuscript.

8.5 Paper V

Paper V uses the CF method on photometry data spanning over 22 years to find the phases of photometric minima, possible activity cycles, and active longitudes of the rapidly rotating late-type star LQ Hydrae. Candidate carrier periods are found using the least-squares fit of harmonics and phase dispersion statistics. The selected carrier period is then used to calculate the phases of local minima.

The most statistically significant period was found to be 1.60514 days. The coherence time only gives a clear symmetric minimum for values around 100 days or less. The period distribution was found to be bimodal, interpreted as spots appearing at either high or low latitudes, but not between. From 2003–2009, coherent structure rotating with a period of 1.6037 days was found to be a possible active longitude. During all other times of observations, the spot phases appeared to be more randomly distributed. Possible epochs for flip-flop events are calculated using the primary and secondary minima. Four flip-flop events are detected within the data, and three more possible events appear during the data gaps. A local fit was used to detect a seventh possible event. The phases of the calculated primary and secondary minima are compared to previous results and newer results from the DI analysis from Paper VI.

This paper was written in conjunction with Paper VI below. The author provided phases and temperatures of spots obtained via DI for comparison purposes with observed primary and secondary minima in the photometry. The author was also responsible for providing insight into the DI technique including earlier results and providing temperature maps to help interpret the CF results. The author participated in writing the manuscript.

8.6 Paper VI

Paper VI uses the Doppler Imaging method to retrieve surface temperature maps of the rapidly rotating late-type star LQ Hya for the years 1998–2002. Some of the observing seasons have poor phase coverage, and so one of the seasons with better phase coverage is selected to test the impact of insufficient phase coverage. From the temperature maps, the spot filling factors, the mean temperatures, and the maximum temperature deviations are calculated for each observing season.

A value of $v \sin i = 26.5\,\mathrm{km\,s^{-1}}$ for the star is determined by selecting the best fit to an unspotted model. The season with the best phase coverage was recalculated using fewer observations, and it was found that no spurious spots were introduced, however, the difference between the temperature of the cool spots and the mean

temperature was found to increase, as well as the spot filling factor. No active longitudes were found with these seven observing seasons. A slight decrease and then increase in mean temperature may be indicative of a possible cycle, but at least two of the seasons with the highest spot coverage had poor phase coverage and the time span of the observations was too short. Averaging over latitudes for each map allowed a comparison to the primary and secondary minima obtained using the continuous period search method and the carrier fit method from Paper V. Cool spots were found to correspond with these minima obtained from photometry.

Reduced spectra were provided to the author, who was then responsible for performing the inversion, including selecting spectral lines, calculating the continuum, adjusting individual spectral line parameters to achieve the best fit, interpreting the resulting temperature maps, and finally comparing results with the photometry from Paper V. The author had the main responsibility of writing the paper.

9 Concluding Remarks

This thesis addresses both the theory of stellar dynamos as realized in numerical simulations and the interpretation of observations with respect to theory. Observations of stellar magnetic fields, spot structures, activity cycles, active longitudes, and flip-flop events motivate numerical simulations to explain the various mechanisms that may operate in a stellar dynamo. In turn, results from numerical simulations can motivate longer-term monitoring of solar analogs as well as providing tools for interpreting observations.

The numerical simulations of this thesis were of the α^2 or $\alpha^2\Omega$ type. This is believed to be the dynamo type operating in stellar convection zones. The models of Paper I were able to produce equatorward dynamo waves with cycles roughly the same order as the solar cycle. This occurred when the Prandtl number (the ratio of the kinematic viscosity to the thermal diffusivity) reaches some threshold value. The models were estimated to be α^2 near the surface due to the phase relation between the radial magnetic field and the azimuthal field near the surface, but further inspection reveals an $\alpha\Omega$ dynamo operating in the deeper layers. By extending to the full azimuthal extent, non-axisymmetric fields form, and structure of the spherical harmonic mode $m = 1$ was observed.

This $m = 1$ structure required a deeper look, motivating Paper II. This mode was predicted by dynamo theory to rotate as a rigid body at a different rate than the fluid, and could provide an alternative explanation to differential rotation for observations of stars. For example, II Pegasi was observed to have an active longitude rotating at a different rate than the mean rotation. Because this star is a rapid rotator with a well-defined period, there is only weak differential rotation which is inadequate to account for the drift of the active longitude. The azimuthal dynamo wave provides a possible alternative. This wave as observed in simulations rotates as a rigid body, independent of depth or latitude. The $m = 2$ mode of the temperature maxima were found to coincide fairly well with the extrema of the $m = 1$ mode of the magnetic field, which is to be expected if the magnetic field directly influences the temperature.

The models of Papers I and II are both spherical wedges, and do not extend to

the polar regions for computational reasons. Instead, a perfect conductor boundary condition is imposed at the latitudinal boundaries and it becomes important to know if observed oscillations of dynamos solutions are real or an artifact of the imposed boundary condition. Previously such a study had been done for $\alpha\Omega$ dynamos, but stellar models tend to be either α^2 or $\alpha^2\Omega$ dynamos. Paper III examines this problem, and finds that solutions in wedge geometry are comparable to spherical geometry under certain conditions; oscillations are possible when the α effect and magnetic diffusivity are concentrated at lower latitudes or when the shear is sufficiently strong. The mean-field models provide a computationally efficient method of verifying the validity of results in larger, more complex numerical simulations.

Suitable targets to test the simulated results were chosen. Both of these young solar analogs, V352 CMa and LQ Hya, are classified as active and super-active stars respectively, based on their rotation period, estimated convective turnover times, and dynamo cycle periods. The CPS method is applied to V352 Canis Majoris, a star estimated to have a Coriolis number of about 27. LQ Hya is analyzed using the CF and DI methods, and estimated to have a Co ≈ 160. In agreement with both the numerical simulations and surveys of stars, the estimated differential rotation coefficient decreases with more rapid rotation, where V352 CMa with a rotation period of 7.2 days has a $|k| \approx 0.12$, while LQ Hya with a rotation period of 1.6 days has a $|k| \approx 0.033$.

Based on classification of the $R'_{\rm HK}$ (an indicator of activity level of a star), V352 CMa lies right near the cut-off between axisymmetric and non-axisymmetric spot structure, but the observed stable active longitude would favor the latter. No Doppler images of this object exist, as its $v \sin i$ make it a less than ideal candidate at this time, and so the spot structure can only be inferred from the photometry. The active longitude found has a faster rotation period than the mean rotation of the star, which is the opposite of the numerical simulations of Paper II, but the Coriolis number of those simulations is also smaller. Preliminary results of numerical simulations with faster rotation periods than those presented in Paper II do not have an azimuthal dynamo wave consistently slower than the rotation period of the model, and this faster regime is worth exploring further. The differential coefficient is high enough for this star that it may be in competition with the azimuthal dynamo wave.

LQ Hya's $R'_{\rm HK}$ places it securely within the non-axisymmetric regime. However, while classified as super-active, it was found to be in the transition region between the super-active and active branches, making it an anomalous star. The non-axisymmetric spot structure can be verified using the DI method, and this is confirmed by observations, both within this thesis and with previous results. No stable active longitude is found for this star using the CF method, but there are pe-

riods with active longitudes with fluctuating periods for times spanning a few years. These active longitudes do not have a rotation period that varies greatly from the star itself. Flip-flops are found using the CF method but do not occur with any regularity, which is in disagreement with some previous results. The chaotic nature of this star is in agreement with the fastest numerical simulations of Paper II where the azimuthal dynamo wave switches between faster and slower rotation periods without any clear cycle. Differential rotation is small enough that it likely has no effect on the spot structure of the star. The observed chaotic nature of this star make it a very interesting object for future observations.

The numerical simulations motivate further work on the parameter regimes where equatorward dynamo waves are found. The nonlinear nature of the models makes it difficult to predict results. The azimuthal dynamo wave should be further explored, as the results here show magnetic structure that rotates slower than the mean rotation, whereas observations of stars also show spot structure with faster rotation than the mean rotation of the star, as well as phase jumps and reversals. Such behavior may be observed in numerical simulations with, for example, different convection zone depths or higher rotation rates. Furthermore, Paper III shows the necessity of revisiting assumptions to verify whether results in numerical simulations are artifacts or real.

The success of the CPS method applied to a star with a low-amplitude light curve motivates the need for further observation and analysis of stars even if they are less than ideal for observing. The CPS method itself is one tool that can be combined with other methods such as the CF method and DI to provide better insight into stellar activity. When dealing with magnetic activity cycles, there is a need for decades of continuous monitoring in order to gain a better understanding of how spot structures, stellar temperatures, and active longitudes change over a cycle. These observations must be continued to be linked to numerical simulations so that the driving mechanisms behind the variable behavior of magnetically active stars can be better understood.

Bibliography

Alekseev, I. Y. (2003). Broad-band Multicolor Photometry and Polarimetry of Spotted Stars. *Astronomy Reports*, 47:430–442.

Augustson, K., Brun, A. S., Miesch, M., and Toomre, J. (2015). Grand Minima and Equatorward Propagation in a Cycling Stellar Convective Dynamo. *The Astrophysical Journal*, 809:149.

Ayyar, P. R. C. (1932). Two Longitudinal Zones of Apparent Inhibition of Sunspots on the Solar Disc. *Kodaikanal Observatory Bulletins*, 4:299–304.

Babcock, H. W. (1947). Zeeman Effect in Stellar Spectra. *The Astrophysical Journal*, 105:105.

Babcock, H. W. (1961). The Topology of the Sun's Magnetic Field and the 22-YEAR Cycle. *The Astrophysical Journal*, 133:572.

Babcock, H. W. and Babcock, H. D. (1955). The Sun's Magnetic Field, 1952-1954. *The Astrophysical Journal*, 121:349.

Baliunas, S. L., Donahue, R. A., Soon, W. H., Horne, J. H., Frazer, J., Woodard-Eklund, L., Bradford, M., Rao, L. M., Wilson, O. C., Zhang, Q., Bennett, W., Briggs, J., Carroll, S. M., Duncan, D. K., Figueroa, D., Lanning, H. H., Misch, T., Mueller, J., Noyes, R. W., Poppe, D., Porter, A. C., Robinson, C. R., Russell, J., Shelton, J. C., Soyumer, T., Vaughan, A. H., and Whitney, J. H. (1995). Chromospheric variations in main-sequence stars. *The Astrophysical Journal*, 438:269–287.

Balthasar, H. and Schuessler, M. (1983). Preferred longitudes of sunspot groups and high-speed solar wind streams - Evidence for a 'solar memory'. *Solar Physics*, 87:23–36.

Barekat, A., Schou, J., and Gizon, L. (2014). The radial gradient of the near-surface shear layer of the Sun. *Astronomy & Astrophysics*, 570:L12.

Barekat, A., Schou, J., and Gizon, L. (2016). Solar-cycle variation of the rotational shear near the solar surface. *Astronomy & Astrophysics*, 595:A8.

Barnes, J. R., Collier Cameron, A., Donati, J.-F., James, D. J., Marsden, S. C., and Petit, P. (2005). The dependence of differential rotation on temperature and rotation. *Monthly Notices of the Royal Astronomical Society*, 357:L1–L5.

Baryshnikova, I. and Shukurov, A. (1987). Oscillatory alpha-squared dynamo - Numerical investigation. *Astronomische Nachrichten*, 308:89–100.

Berdyugina, S. V. (2005). Starspots: A Key to the Stellar Dynamo. *Living Reviews in Solar Physics*, 2.

Berdyugina, S. V., Pelt, J., and Tuominen, I. (2002). Magnetic activity in the young solar analog LQ Hydrae. I. Active longitudes and cycles. *Astronomy & Astrophysics*, 394:505–515.

Berdyugina, S. V. and Tuominen, I. (1998). Permanent active longitudes and activity cycles on RS CVn stars. *Astronomy & Astrophysics*, 336:L25–L28.

Berdyugina, S. V. and Usoskin, I. G. (2003). Active longitudes in sunspot activity: Century scale persistence. *Astronomy & Astrophysics*, 405:1121–1128.

Bopp, B. W. and Evans, D. S. (1973). The spotted flare stars BY Dra and CC Eri: a model for the spots and some astrophysical implications. *Monthly Notices of the Royal Astronomical Society*, 164:343–356.

Bopp, B. W. and Stencel, R. E. (1981). The FK Comae stars. *The Astrophysical Journal Letters*, 247:L131–L134.

Boyd, T. J. M. and Sanderson, J. J. (2003). *The Physics of Plasmas*.

Brandenburg, A., Candelaresi, S., and Chatterjee, P. (2009). Small-scale magnetic helicity losses from a mean-field dynamo. *Monthly Notices of the Royal Astronomical Society*, 398:1414–1422.

Brandenburg, A., Krause, F., Meinel, R., Moss, D., and Tuominen, I. (1989). The stability of nonlinear dynamos and the limited role of kinematic growth rates. *Astronomy & Astrophysics*, 213:411–422.

Brandenburg, A., Moss, D., and Tuominen, I. (1992). Stratification and thermodynamics in mean-field dynamos. *Astronomy & Astrophysics*, 265:328–344.

Brandenburg, A., Saar, S. H., and Turpin, C. R. (1998). Time Evolution of the Magnetic Activity Cycle Period. *The Astrophysical Journal Letters*, 498:L51–L54.

Brandenburg, A. and Subramanian, K. (2005). Astrophysical magnetic fields and nonlinear dynamo theory. *Physics Reports*, 417:1–209.

Brown, B. P., Browning, M. K., Brun, A. S., Miesch, M. S., and Toomre, J. (2010). Persistent Magnetic Wreaths in a Rapidly Rotating Sun. *The Astrophysical Journal*, 711:424–438.

Brown, B. P., Miesch, M. S., Browning, M. K., Brun, A. S., and Toomre, J. (2011). Magnetic Cycles in a Convective Dynamo Simulation of a Young Solar-type Star. *The Astrophysical Journal*, 731:69.

Brown, T. M. and Gilliland, R. L. (1994). Asteroseismology. *Annual Review of Astronomy & Astrophysics*, 32:37–82.

Bruls, J. H. M. J., Solanki, S. K., and Schuessler, M. (1998). Doppler imaging: the polar SPOT controversy. *Astronomy & Astrophysics*, 336:231–241.

Bruning, D. H. (1981). Fourier analysis of differential rotation in late-type stars. *The Astrophysical Journal*, 248:274–278.

Candelaresi, S., Hubbard, A., Brandenburg, A., and Mitra, D. (2011). Magnetic helicity transport in the advective gauge family. *Physics of Plasmas*, 18(1):012903–012903.

Cantiello, M., Fuller, J., and Bildsten, L. (2016). Asteroseismic Signatures of Evolving Internal Stellar Magnetic Fields. *The Astrophysical Journal*, 824:14.

Carrington, R. C. (1858). On the Distribution of the Solar Spots in Latitudes since the Beginning of the Year 1854, with a Map. *Monthly Notices of the Royal Astronomical Society*, 19:1–3.

Cayrel de Strobel, G. (1996). Stars resembling the Sun. *Astronomy and Astrophysics Review*, 7:243–288.

Chandrasekhar, S. (1961). *Hydrodynamic and hydromagnetic stability.*

Chen, W.-C., Li, X.-D., and Qian, S.-B. (2006). Orbital Evolution of Algol Binaries with a Circumbinary Disk. *The Astrophysical Journal*, 649:973–978.

Chugainov, P. F. (1966). On the Variability of HD 234677. *Information Bulletin on Variable Stars*, 122.

Cole, E., Brandenburg, A., Käpylä, P. J., and Käpylä, M. J. (2016). Robustness of oscillatory α^2 dynamos in spherical wedges. *Astronomy & Astrophysics*, 593:A134.

Cole, E., Käpylä, P. J., Mantere, M. J., and Brandenburg, A. (2014). An Azimuthal Dynamo Wave in Spherical Shell Convection. *The Astrophysical Journal Letters*, 780:L22.

Cowling, T. G. (1933). The magnetic field of sunspots. *Monthly Notices of the Royal Astronomical Society*, 94:39–48.

Cutispoto, G. (1991). UBVRI observations of southern hemisphere active stars. II - 1987 data. *Astronomy & Astrophysics Supplement Series*, 89:435–449.

Cutispoto, G. (1998). Long-term monitoring of active stars. VIII. UBV(RI)_(c) photometry collected in February 1992. *Astronomy & Astrophysics Supplement Series*, 131:321–344.

Cutispoto, G., Pastori, L., Tagliaferri, G., Messina, S., and Pallavicini, R. (1999). Classification of EUV stellar sources detected by the ROSAT WFC. I. Photometric and radial velocity studies. *Astronomy & Astrophysics Supplement Series*, 138:87–99.

Dikpati, M. and Gilman, P. A. (2001a). Flux-Transport Dynamos with α-Effect from Global Instability of Tachocline Differential Rotation: A Solution for Magnetic Parity Selection in the Sun. *The Astrophysical Journal*, 559:428–442.

Dikpati, M. and Gilman, P. A. (2001b). Symmetry Selection in Solar Cycle Dynamo Models. In Mathys, G., Solanki, S. K., and Wickramasinghe, D. T., editors, *Magnetic Fields Across the Hertzsprung-Russell Diagram*, volume 248 of *Astronomical Society of the Pacific Conference Series*, page 125.

Domiciano de Souza, A., Zorec, J., Jankov, S., Vakili, F., Abe, L., and Janot-Pacheco, E. (2004). Stellar differential rotation and inclination angle from spectro-interferometry. *Astronomy & Astrophysics*, 418:781–794.

Donahue, R. A., Saar, S. H., and Baliunas, S. L. (1996). A Relationship between Mean Rotation Period in Lower Main-Sequence Stars and Its Observed Range. *The Astrophysical Journal*, 466:384.

Donati, J.-F. (1999). Magnetic cycles of HR 1099 and LQ Hydrae. *Monthly Notices of the Royal Astronomical Society*, 302:457–481.

Donati, J.-F. (2011). Large-scale magnetic fields of low-mass dwarfs: the many faces of dynamo. In Brummell, N. H., Brun, A. S., Miesch, M. S., and Ponty, Y., editors, *Astrophysical Dynamics: From Stars to Galaxies*, volume 271 of *IAU Symposium*, pages 23–31.

Donati, J.-F. and Collier Cameron, A. (1997). Differential rotation and magnetic polarity patterns on AB Doradus. *Monthly Notices of the Royal Astronomical Society*, 291:1–19.

Donati, J.-F., Collier Cameron, A., and Petit, P. (2003a). Temporal fluctuations in the differential rotation of cool active stars. *Monthly Notices of the Royal Astronomical Society*, 345:1187–1199.

Donati, J.-F., Collier Cameron, A., Semel, M., Hussain, G. A. J., Petit, P., Carter, B. D., Marsden, S. C., Mengel, M., López Ariste, A., Jeffers, S. V., and Rees, D. E. (2003b). Dynamo processes and activity cycles of the active stars AB Doradus, LQ Hydrae and HR 1099. *Monthly Notices of the Royal Astronomical Society*, 345:1145–1186.

Duarte, L. D. V., Wicht, J., Browning, M. K., and Gastine, T. (2016). Helicity inversion in spherical convection as a means for equatorward dynamo wave propagation. *Monthly Notices of the Royal Astronomical Society*, 456:1708–1722.

Faye, M. (1883). Academie des Sciences. Sur les mouvements du sol de l'Observatoire de Neuchatel. *L'Astronomie*, 2:297–301.

Fekel, F. C., Bopp, B. W., Africano, J. L., Goodrich, B. D., Palmer, L. H., Quingley, R., and Simon, T. (1986). Chromospherically active stars. II - HD 82558, a young single BY Draconis variable. *The Astronomical Journal*, 92:1150–1154.

Fröhlich, C. (2012). Total Solar Irradiance Observations. *Surveys in Geophysics*, 33:453–473.

Gaidos, E. J., Henry, G. W., and Henry, S. M. (2000). Spectroscopy and Photometry of Nearby Young Solar Analogs. *The Astronomical Journal*, 120:1006–1013.

Galilei, G. (1613). *Istoria e Dimostrazioni Intorno Alle Macchie Solari e Loro Accidenti Rome (History and Demonstrations Concerning Sunspots and their Properties).*

Gilman, P. A. (1983). Dynamically consistent nonlinear dynamos driven by convection in a rotating spherical shell. II - Dynamos with cycles and strong feedbacks. *The Astrophysical Journal Supplement Series*, 53:243–268.

Gizon, L. and Solanki, S. K. (2004). Measuring Stellar Differential rotation with asteroseismology. *Solar Physics*, 220:169–184.

Glatzmaier, G. A. (1985). Numerical simulations of stellar convective dynamos. II - Field propagation in the convection zone. *The Astrophysical Journal*, 291:300–307.

Gray, R. O., Corbally, C. J., Garrison, R. F., McFadden, M. T., Bubar, E. J., McGahee, C. E., O'Donoghue, A. A., and Knox, E. R. (2006). Contributions to the Nearby Stars (NStars) Project: Spectroscopy of Stars Earlier than M0 within 40 pc-The Southern Sample. *The Astronomical Journal*, 132:161–170.

Guerrero, G. and de Gouveia Dal Pino, E. M. (2009). Flux transport solar dynamo models, current problems and possible solutions. In *Revista Mexicana de Astronomia y Astrofisica Conference Series*, volume 36 of *Revista Mexicana de Astronomia y Astrofisica, vol. 27*, pages CD252–CD261.

Hackman, T., Jetsu, L., and Tuominen, I. (2001). Surface imaging of HD 199178 (V1794 Cygni). *Astronomy & Astrophysics*, 374:171–181.

Hackman, T., Lehtinen, J., Rosén, L., Kochukhov, O., and Käpylä, M. J. (2016). Zeeman-Doppler imaging of active young solar-type stars. *Astronomy & Astrophysics*, 587:A28.

Hackman, T., Mantere, M. J., Jetsu, L., Ilyin, I., Kajatkari, P., Kochukhov, O., Lehtinen, J., Lindborg, M., Piskunov, N., and Tuominen, I. (2011). Spot activity of II Peg. *Astronomische Nachrichten*, 332:859.

Hackman, T., Mantere, M. J., Lindborg, M., Ilyin, I., Kochukhov, O., Piskunov, N., and Tuominen, I. (2012). Doppler images of II Pegasi for 2004-2010. *Astronomy & Astrophysics*, 538:A126.

Hackman, T., Pelt, J., Mantere, M. J., Jetsu, L., Korhonen, H., Granzer, T., Kajatkari, P., Lehtinen, J., and Strassmeier, K. G. (2013). Flip-flops of FK Comae Berenices. *Astronomy & Astrophysics*, 553:A40.

Hale, G. E. (1908). On the Probable Existence of a Magnetic Field in Sun-Spots. *The Astrophysical Journal*, 28:315.

Hale, G. E. (1913). Preliminary Results of an Attempt to Detect the General Magnetic Field of the Sun. *The Astrophysical Journal*, 38:27.

Hale, G. E., Ellerman, F., Nicholson, S. B., and Joy, A. H. (1919). The Magnetic Polarity of Sun-Spots. *The Astrophysical Journal*, 49:153.

Hale, G. E. and Nicholson, S. B. (1925). The Law of Sun-Spot Polarity. *The Astrophysical Journal*, 62:270.

Hall, D. S. (1972). A T Tauri-Like Star in the Eclipsing Binary RS Canum Venaticorum. *Publications of the Astronomical Society of the Pacific*, 84:323.

Hall, D. S. (1976). The RS CVn Binaries and Binaries with Similar PROPERTIÉS. In Fitch, W. S., editor, *IAU Colloq. 29: Multiple Periodic Variable Stars*, volume 60 of *Astrophysics and Space Science Library*, page 287.

Hathaway, D. H. (2010). The Solar Cycle. *Living Reviews in Solar Physics*, 7.

Haywood, M. (2001). A revision of the solar neighbourhood metallicity distribution. *Monthly Notices of the Royal Astronomical Society*, 325:1365–1382.

Henry, G. W., Eaton, J. A., Hamer, J., and Hall, D. S. (1995). Starspot evolution, differential rotation, and magnetic cycles in the chromospherically active binaries lambda andromedae, sigma Geminorum, II Pegasi, and V711 Tauri. *The Astrophysical Journal Supplement Series*, 97:513–549.

Howe, R. (2009). Solar Interior Rotation and its Variation. *Living Reviews in Solar Physics*, 6.

Hundt, E. (1973). Microturbulence in Stellar Spectroscopy. *Astronomy & Astrophysics*, 29:17.

Jennings, R., Brandenburg, A., Tuominen, I., and Moss, D. (1990). Can stellar dynamos be modelled in less than three dimensions? *Astronomy & Astrophysics*, 230:463–473.

Jetsu, L. (1993). A Decade of Photometry of Lq-Hydrae. *Astronomy & Astrophysics*, 276:345.

Jetsu, L. and Pelt, J. (1996). Searching for periodicity in weighted time point series. *Astronomy & Astrophysics Supplement Series*, 118:587–594.

Jetsu, L. and Pelt, J. (1999). Three stage period analysis and complementary methods. *Astronomy & Astrophysics Supplement Series*, 139:629–643.

Joy, A. H. (1945). T Tauri Variable Stars. *The Astrophysical Journal*, 102:168.

Kajatkari, P., Jetsu, L., Cole, E., Hackman, T., Henry, G. W., Joutsiniemi, S.-L., Lehtinen, J., Mäkelä, V., Porceddu, S., Ryynänen, K., and Solea, V. (2015). Periodicity in some light curves of the solar analogue V352 Canis Majoris. *Astronomy & Astrophysics*, 577:A84.

Käpylä, M. J., Käpylä, P. J., Olspert, N., Brandenburg, A., Warnecke, J., Karak, B. B., and Pelt, J. (2016a). Multiple dynamo modes as a mechanism for long-term solar activity variations. *Astronomy & Astrophysics*, 589:A56.

Käpylä, P. J., Käpylä, M. J., and Brandenburg, A. (2014). Confirmation of bistable stellar differential rotation profiles. *Astronomy & Astrophysics*, 570:A43.

Käpylä, P. J., Käpylä, M. J., Olspert, N., Warnecke, J., and Brandenburg, A. (2016b). Convection-driven spherical shell dynamos at varying Prandtl numbers. *ArXiv e-prints*.

Käpylä, P. J., Korpi, M. J., and Brandenburg, A. (2009). Alpha effect and turbulent diffusion from convection. *Astronomy & Astrophysics*, 500:633–646.

Käpylä, P. J., Korpi, M. J., Brandenburg, A., Mitra, D., and Tavakol, R. (2010). Convective dynamos in spherical wedge geometry. *Astronomische Nachrichten*, 331:73.

Käpylä, P. J., Korpi, M. J., Ossendrijver, M., and Stix, M. (2006). Magnetoconvection and dynamo coefficients. III. α-effect and magnetic pumping in the rapid rotation regime. *Astronomy & Astrophysics*, 455:401–412.

Käpylä, P. J., Mantere, M. J., and Brandenburg, A. (2011a). Effects of stratification in spherical shell convection. *Astronomische Nachrichten*, 332:883.

Käpylä, P. J., Mantere, M. J., and Brandenburg, A. (2012). Cyclic Magnetic Activity due to Turbulent Convection in Spherical Wedge Geometry. *The Astrophysical Journal Letters*, 755:L22.

Käpylä, P. J., Mantere, M. J., and Brandenburg, A. (2013a). Oscillatory large-scale dynamos from Cartesian convection simulations. *Geophysical and Astrophysical Fluid Dynamics*, 107:244–257.

Käpylä, P. J., Mantere, M. J., Cole, E., Warnecke, J., and Brandenburg, A. (2013b). Effects of Enhanced Stratification on Equatorward Dynamo Wave Propagation. *The Astrophysical Journal*, 778:41.

Käpylä, P. J., Mantere, M. J., Guerrero, G., Brandenburg, A., and Chatterjee, P. (2011b). Reynolds stress and heat flux in spherical shell convection. *Astronomy & Astrophysics*, 531:A162.

Kitchatinov, L. L., Pipin, V. V., and Rüdiger, G. (1994). Turbulent viscosity, magnetic diffusivity, and heat conductivity under the influence of rotation and magnetic field. *Astronomische Nachrichten*, 315:157–170.

Kitchatinov, L. L. and Rüdiger, G. (1995). Differential rotation in solar-type stars: revisiting the Taylor-number puzzle. *Astronomy & Astrophysics*, 299:446.

Kochukhov, O., Mantere, M. J., Hackman, T., and Ilyin, I. (2013). Magnetic field topology of the RS CVn star II Pegasi. *Astronomy & Astrophysics*, 550:A84.

Kolmogorov, A. (1941a). The Local Structure of Turbulence in Incompressible Viscous Fluid for Very Large Reynolds' Numbers. *Akademiia Nauk SSSR Doklady*, 30:301–305.

Kolmogorov, A. N. (1941b). Dissipation of Energy in Locally Isotropic Turbulence. *Akademiia Nauk SSSR Doklady*, 32:16.

Korhonen, H., Berdyugina, S. V., Hackman, T., Ilyin, I. V., Strassmeier, K. G., and Tuominen, I. (2007). Study of FK Comae Berenices. V. Spot evolution and detection of surface differential rotation. *Astronomy & Astrophysics*, 476:881–891.

Korhonen, H., Berdyugina, S. V., and Tuominen, I. (2002). Study of FK Comae Berenices. IV. Active longitudes and the "flip-flop" phenomenon. *Astronomy & Astrophysics*, 390:179–185.

Korhonen, H., Wittkowski, M., Kovári, Z., Granzer, T., Hackman, T., and Strassmeier, K. G. (2010). Ellipsoidal primary of the RS CVn binary ζ Andromedae . Investigation using high-resolution spectroscopy and optical interferometry. *Astronomy & Astrophysics*, 515:A14.

Kóspál, Á., Ardila, D. R., Moór, A., and Ábrahám, P. (2009). On the Relationship Between Debris Disks and Planets. *The Astrophysical Journal Letters*, 700:L73–L77.

Kovári, Z., Strassmeier, K. G., Granzer, T., Weber, M., Oláh, K., and Rice, J. B. (2004). Doppler imaging of stellar surface structure. XXII. Time-series mapping of the young rapid rotator LQ Hydrae. *Astronomy & Astrophysics*, 417:1047–1054.

Krause, F. and Rädler, K.-H. (1980). *Mean-field magnetohydrodynamics and dynamo theory.*

Krivova, N. A., Balmaceda, L., and Solanki, S. K. (2007). Reconstruction of solar total irradiance since 1700 from the surface magnetic flux. *Astronomy & Astrophysics*, 467:335–346.

Kron, G. E. (1947). The Probable Detecting of Surface Spots on AR Lacertae B. *Publications of the Astronomical Society of the Pacific*, 59:261.

Küker, M. and Rüdiger, G. (1999). Magnetic field generation in weak-line T Tauri stars: an alpha (2) -dynamo. *Astronomy & Astrophysics*, 346:922–928.

Kuzanyan, K. M., Pipin, V. V., and Seehafer, N. (2006). The Alpha Effect and the Observed Twist and Current Helicity of Solar Magnetic Fields. *Solar Physics*, 233:185–204.

Lanza, A. F., Rodono, M., and Zappala, R. A. (1993). Fourier analysis of spotted star light curves as a tool to detect stellar differential rotation. *Astronomy & Astrophysics*, 269:351–354.

Lehtinen, J., Jetsu, L., Hackman, T., Kajatkari, P., and Henry, G. W. (2011). The continuous period search method and its application to the young solar analogue HD 116956. *Astronomy & Astrophysics*, 527:A136.

Lehtinen, J., Jetsu, L., Hackman, T., Kajatkari, P., and Henry, G. W. (2012). Spot activity of LQ Hydra from photometry between 1988 and 2011. *Astronomy & Astrophysics*, 542:A38.

Lehtinen, J., Jetsu, L., Hackman, T., Kajatkari, P., and Henry, G. W. (2016). Activity trends in young solar-type stars. *Astronomy & Astrophysics*, 588:A38.

Leighton, R. B. (1969). A Magneto-Kinematic Model of the Solar Cycle. *The Astrophysical Journal*, 156:1.

Lindborg, M., Hackman, T., Mantere, M. J., Korhonen, H., Ilyin, I., Kochukhov, O., and Piskunov, N. (2014). Doppler images of DI Piscium during 2004-2006. *Astronomy & Astrophysics*, 562:A139.

Lindborg, M., Mantere, M. J., Olspert, N., Pelt, J., Hackman, T., Henry, G. W., Jetsu, L., and Strassmeier, K. G. (2013). Multiperiodicity, modulations and flip-flops in variable star light curves. II. Analysis of II Pegasus photometry during 1979-2010. *Astronomy & Astrophysics*, 559:A97.

Losh, H. M. (1939). Distribution of sun-spots in longitude. *Publications of Michigan Observatory*, 7:127–145.

Lund, M. N., Miesch, M. S., and Christensen-Dalsgaard, J. (2014). Differential Rotation in Main-sequence Solar-like Stars: Qualitative Inference from Asteroseismic Data. *The Astrophysical Journal*, 790:121.

Marsden, S. C., Carter, B. D., and Donati, J.-F. (2005). Doppler imaging and differential rotation of young open cluster stars. In Favata, F., Hussain, G. A. J., and Battrick, B., editors, *13th Cambridge Workshop on Cool Stars, Stellar Systems and the Sun*, volume 560 of *ESA Special Publication*, page 799.

Mason, B. D., Wycoff, G. L., Hartkopf, W. I., Douglass, G. G., and Worley, C. E. (2001). The 2001 US Naval Observatory Double Star CD-ROM. I. The Washington Double Star Catalog. *The Astronomical Journal*, 122:3466–3471.

Maunder, E. W. (1904). Note on the distribution of sun-spots in heliographic latitude, 1874-1902. *Monthly Notices of the Royal Astronomical Society*, 64:747–761.

Messina, S. and Guinan, E. F. (2003). Magnetic activity of six young solar analogues II. Surface Differential Rotation from long-term photometry. *Astronomy & Astrophysics*, 409:1017–1030.

Mitra, D., Tavakol, R., Brandenburg, A., and Moss, D. (2009). Turbulent Dynamos in Spherical Shell Segments of Varying Geometrical Extent. *The Astrophysical Journal*, 697:923–933.

Moffatt, H. K. (1978). *Magnetic field generation in electrically conducting fluids.*

Moss, D., Barker, D. M., Brandenburg, A., and Tuominen, I. (1995). Nonaxisymmetric dynamo solutions and extended starspots on late-type stars. *Astronomy & Astrophysics*, 294:155–164.

Moss, D., Sokoloff, D., Kuzanyan, K., and Petrov, A. (2004). Stellar Dynamo Waves: Asymptotic Configurations. *Geophysical and Astrophysical Fluid Dynamics*, 98:257–272.

Moss, D., Tuominen, I., and Brandenburg, A. (1991). Nonlinear nonaxisymmetric dynamo models for cool stars. *Astronomy & Astrophysics*, 245:129–135.

Nelson, N. J., Brown, B. P., Brun, A. S., Miesch, M. S., and Toomre, J. (2013). Magnetic Wreaths and Cycles in Convective Dynamos. *The Astrophysical Journal*, 762:73.

Noyes, R. W., Hartmann, L. W., Baliunas, S. L., Duncan, D. K., and Vaughan, A. H. (1984). Rotation, convection, and magnetic activity in lower main-sequence stars. *The Astrophysical Journal*, 279:763–777.

Oláh, K., Kolláth, Z., Granzer, T., Strassmeier, K. G., Lanza, A. F., Järvinen, S., Korhonen, H., Baliunas, S. L., Soon, W., Messina, S., and Cutispoto, G. (2009). Multiple and changing cycles of active stars. II. Results. *Astronomy & Astrophysics*, 501:703–713.

Oláh, K., Kolláth, Z., and Strassmeier, K. G. (2000). Multiperiodic light variations of active stars. *Astronomy & Astrophysics*, 356:643–653.

Olspert, N., Käpylä, M. J., Pelt, J., Cole, E. M., Hackman, T., Lehtinen, J., and Henry, G. W. (2015). Multiperiodicity, modulations, and flip-flops in variable star light curves. III. Carrier fit analysis of LQ Hydrae photometry for 1982-2014. *Astronomy & Astrophysics*, 577:A120.

Ossendrijver, M., Stix, M., Brandenburg, A., and Rüdiger, G. (2002). Magnetoconvection and dynamo coefficients. II. Field-direction dependent pumping of magnetic field. *Astronomy & Astrophysics*, 394:735–745.

Parker, E. N. (1955). Hydromagnetic Dynamo Models. *The Astrophysical Journal*, 122:293.

Parker, E. N. (1987). The dynamo dilemma. *Solar Physics*, 110:11–21.

Pelt, J. (1983). Phase dispersion minimization methods for estimation of periods from unequally spaced sequences of data. In Rolfe, E. J., editor, *Statistical Methods in Astronomy*, volume 201 of *ESA Special Publication*.

Pelt, J., Brooke, J. M., Korpi, M. J., and Tuominen, I. (2006). Kinematic frames and "active longitudes": does the Sun have a face? *Astronomy & Astrophysics*, 460:875–885.

Pelt, J., Korpi, M. J., and Tuominen, I. (2010). Solar active regions: a nonparametric statistical analysis. *Astronomy & Astrophysics*, 513:A48.

Pelt, J., Olspert, N., Mantere, M. J., and Tuominen, I. (2011). Multiperiodicity, modulations and flip-flops in variable star light curves. I. Carrier fit method. *Astronomy & Astrophysics*, 535:A23.

Petit, P., Donati, J.-F., and Collier Cameron, A. (2002). Differential rotation of cool active stars: the case of intermediate rotators. *Monthly Notices of the Royal Astronomical Society*, 334:374–382.

Piomelli, U. (2014). Large eddy simulations in 2030 and beyond. *Philosophical Transactions of the Royal Society of London Series A*, 372:20130320–20130320.

Piskunov, N. E., Kupka, F., Ryabchikova, T. A., Weiss, W. W., and Jeffery, C. S. (1995). VALD: The Vienna Atomic Line Data Base. *Astronomy & Astrophysics Supplement Series*, 112:525.

Piskunov, N. E., Tuominen, I., and Vilhu, O. (1990). Surface imaging of late-type stars. *Astronomy & Astrophysics*, 230:363–370.

Pope, S. B. (2004). Ten questions concerning the large-eddy simulation of turbulent flows. *New Journal of Physics*, 6:35.

Popper, D. M. (1953). A Possible New Flare Star. *Publications of the Astronomical Society of the Pacific*, 65:278.

Pouquet, A., Frisch, U., and Leorat, J. (1976). Strong MHD helical turbulence and the nonlinear dynamo effect. *Journal of Fluid Mechanics*, 77:321–354.

Rädler, K.-H. (1969). On some electromagnetic phenomena in electrically conducting turbulently moving matter, especially in the presence of Coriolis forces. *Veroeffentlichungen der Geod. Geophys*, 13:131–135.

Rädler, K.-H. (1980). Mean-field approach to spherical dynamo models. *Astronomische Nachrichten*, 301:101–129.

Rädler, K.-H. (1986). Investigations of spherical kinematic mean-field dynamo models. *Astronomische Nachrichten*, 307:89–113.

Rädler, K.-H. and Braeuer, H.-J. (1987). On the oscillatory behaviour of kinematic mean-field dynamos. *Astronomische Nachrichten*, 308:101–109.

Rädler, K.-H., Kleeorin, N., and Rogachevskii, I. (2003). The Mean Electromotive Force for MHD Turbulence: The Case of a Weak Mean Magnetic Field and Slow Rotation. *Geophysical and Astrophysical Fluid Dynamics*, 97:249–274.

Rädler, K.-H., Wiedemann, E., Brandenburg, A., Meinel, R., and Tuominen, I. (1990). Nonlinear mean-field dynamo models - Stability and evolution of three-dimensional magnetic field configurations. *Astronomy & Astrophysics*, 239:413–423.

Reiners, A. and Schmitt, J. H. M. M. (2002). On the feasibility of the detection of differential rotation in stellar absorption profiles. *Astronomy & Astrophysics*, 384:155–162.

Reinhold, T. and Arlt, R. (2015). Discriminating solar and antisolar differential rotation in high-precision light curves. *Astronomy & Astrophysics*, 576:A15.

Reinhold, T. and Reiners, A. (2013). Fast and reliable method for measuring stellar differential rotation from photometric data. *Astronomy & Astrophysics*, 557:A11.

Rheinhardt, M. and Brandenburg, A. (2010). Test-field method for mean-field coefficients with MHD background. *Astronomy & Astrophysics*, 520:A28.

Rice, J. B. and Strassmeier, K. G. (1998). Doppler imaging of stellar surface structure. VII. The very young, single K2-dwarf LQ Hydrae. *Astronomy & Astrophysics*, 336:972–979.

Rice, J. B. and Strassmeier, K. G. (2000). Doppler imaging from artificial data. Testing the temperature inversion from spectral-line profiles. *Astronomy & Astrophysics Supplement Series*, 147:151–168.

Rogachevskii, I. and Kleeorin, N. (2006). Small-scale magnetic buoyancy and magnetic pumping effects in a turbulent convection. *Geophysical and Astrophysical Fluid Dynamics*, 100:243–263.

Rosén, L., Kochukhov, O., Hackman, T., and Lehtinen, J. (2016). Magnetic fields of young solar twins. *Astronomy & Astrophysics*, 593:A35.

Rüdiger, G., Elstner, D., and Ossendrijver, M. (2003). Do spherical α^2-dynamos oscillate? *Astronomy & Astrophysics*, 406:15–21.

Rüdiger, G., von Rekowski, B., Donahue, R. A., and Baliunas, S. L. (1998). Differential Rotation and Meridional Flow for Fast-rotating Solar-Type Stars. *The Astrophysical Journal*, 494:691–699.

Saar, S. H. and Baliunas, S. L. (1992). Recent Advances in Stellar Cycle Research. In Harvey, K. L., editor, *The Solar Cycle*, volume 27 of *Astronomical Society of the Pacific Conference Series*, pages 150–167.

Saar, S. H. and Brandenburg, A. (1999). Time Evolution of the Magnetic Activity Cycle Period. II. Results for an Expanded Stellar Sample. *The Astrophysical Journal*, 524:295–310.

Santos, N. C., Israelian, G., García López, R. J., Mayor, M., Rebolo, R., Randich, S., Ecuvillon, A., and Domínguez Cerdeña, C. (2004). Are beryllium abundances anomalous in stars with giant planets? *Astronomy & Astrophysics*, 427:1085–1096.

Scherrer, P. H., Schou, J., Bush, R. I., Kosovichev, A. G., Bogart, R. S., Hoeksema, J. T., Liu, Y., Duvall, T. L., Zhao, J., Title, A. M., Schrijver, C. J., Tarbell, T. D., and Tomczyk, S. (2012). The Helioseismic and Magnetic Imager (HMI) Investigation for the Solar Dynamics Observatory (SDO). *Solar Physics*, 275:207–227.

Schrinner, M., Rädler, K.-H., Schmitt, D., Rheinhardt, M., and Christensen, U. (2005). Mean-field view on rotating magnetoconvection and a geodynamo model. *Astronomische Nachrichten*, 326:245–249.

Schwabe, M. (1843). Die Sonne. Von Herrn Hofrath Schwabe. *Astronomische Nachrichten*, 20:283.

Selam, S. O. (2004). Key parameters of W UMa-type contact binaries discovered by HIPPARCOS. *Astronomy & Astrophysics*, 416:1097–1105.

Semel, M. (1989). Zeeman-Doppler imaging of active stars. I - Basic principles. *Astronomy & Astrophysics*, 225:456–466.

Siwak, M., Rucinski, S. M., Matthews, J. M., Kuschnig, R., Guenther, D. B., Moffat, A. F. J., Sasselov, D., and Weiss, W. W. (2010). Analysis of the MOST light curve of the heavily spotted K2IV component of the single-line spectroscopic binary II Pegasi. *Monthly Notices of the Royal Astronomical Society*, 408:314–321.

Skelly, M. B., Donati, J.-F., Bouvier, J., Grankin, K. N., Unruh, Y. C., Artemenko, S. A., and Petrov, P. (2010). Dynamo processes in the T Tauri star V410 Tau. *Monthly Notices of the Royal Astronomical Society*, 403:159–169.

Skilling, J. and Bryan, R. K. (1984). Maximum Entropy Image Reconstruction - General Algorithm. *Monthly Notices of the Royal Astronomical Society*, 211:111.

Smagorinsky, J. (1963). General Circulation Experiments with the Primitive Equations. *Monthly Weather Review*, 91:99.

Snodgrass, H. B. and Ulrich, R. K. (1990). Rotation of Doppler features in the solar photosphere. *The Astrophysical Journal*, 351:309–316.

Spörer, F. W. G. (1890). Prof. Spoerer's researches on Sun-spots. *Monthly Notices of the Royal Astronomical Society*, 50:251.

Steenbeck, M., Krause, F., and Rädler, K.-H. (1966). Berechnung der mittleren Lorentz-Feldstärke $\overline{\mathfrak{u} \times \mathfrak{B}}$ für ein elektrisch leitendes Medium in turbulenter, durch Coriolis-Kräfte beeinflußter Bewegung. *Zeitschrift Naturforschung Teil A*, 21:369.

Strassmeier, K. G. (1988). A multiple SPOT model for simultaneous solution of light curves and distorted line profiles of spotted stars. *Astrophysics and Space Science*, 140:223–235.

Strassmeier, K. G. (2002). Doppler images of starspots. *Astronomische Nachrichten*, 323:309–316.

Strassmeier, K. G., Bartus, J., Cutispoto, G., and Rodono, M. (1997). Starspot photometry with robotic telescopes: Continuous UBV and V(RI)_C photometry of 23 stars in 1991-1996. *Astronomy & Astrophysics Supplement Series*, 125.

Strassmeier, K. G., Rice, J. B., Wehlau, W. H., Hill, G. M., and Matthews, J. M. (1993). Surface features of the lower atmosphere of HD 82558(= LQ Hydrae). *Astronomy & Astrophysics*, 268:671–684.

Tetzlaff, N., Neuhäuser, R., and Hohle, M. M. (2011). A catalogue of young runaway Hipparcos stars within 3 kpc from the Sun. *Monthly Notices of the Royal Astronomical Society*, 410:190–200.

Tuominen, I., Berdyugina, S. V., and Korpi, M. J. (2002). Starspot cycles from Doppler imaging and photometric time series as nonlinear dynamo. *Astronomische Nachrichten*, 323:367–370.

Vaquero, J. M. and Vázquez, M. (2009). *The Sun Recorded Through History*.

Vaughan, A. H. and Preston, G. W. (1980). A survey of chromospheric CA II H and K emission in field stars of the solar neighborhood. *Publications of the Astronomical Society of the Pacific*, 92:385–391.

Vitinskij, J. I. (1969). On the Problem of Active Longitudes of Sunspots and Flares. *Solar Physics*, 7:210–216.

Vogt, S. S. (1979). A spectroscopic and photometric study of the star spot on HD 224085. *Publications of the Astronomical Society of the Pacific*, 91:616.

Vogt, S. S. (1981). A method for unambiguous determination of starspot temperatures and areas - Application to II Pegasi, BY Draconis, and HD 209813. *The Astrophysical Journal*, 250:327–340.

Vogt, S. S., Penrod, G. D., and Hatzes, A. P. (1987). Doppler images of rotating stars using maximum entropy image reconstruction. *The Astrophysical Journal*, 321:496–515.

Warnecke, J., Käpylä, P. J., Käpylä, M. J., and Brandenburg, A. (2014). On The Cause of Solar-like Equatorward Migration in Global Convective Dynamo Simulations. *The Astrophysical Journal Letters*, 796:L12.

Warnecke, J., Käpylä, P. J., Mantere, M. J., and Brandenburg, A. (2013). Spoke-like Differential Rotation in a Convective Dynamo with a Coronal Envelope. *The Astrophysical Journal*, 778:141.

Weiss, N. O. and Tobias, S. M. (2016). Supermodulation of the Sun's magnetic activity: the effects of symmetry changes. *Monthly Notices of the Royal Astronomical Society*, 456:2654–2661.

Willson, R. C. and Hudson, H. S. (1991). The sun's luminosity over a complete solar cycle. *Nature*, 351:42–44.

Wilson, O. C. (1963). A Probable Correlation Between Chromospheric Activity and Age in Main-Sequence Stars. *The Astrophysical Journal*, 138:832.

Wilson, O. C. and Vainu Bappu, M. K. (1957). H and K Emission in Late-Type Stars: Dependence of Line Width on Luminosity and Related Topics. *The Astrophysical Journal*, 125:661.

Wright, N. J., Drake, J. J., Mamajek, E. E., and Henry, G. W. (2011). The Stellar-activity-Rotation Relationship and the Evolution of Stellar Dynamos. *The Astrophysical Journal*, 743:48.

Yoshimura, H. (1975). Solar-cycle dynamo wave propagation. *The Astrophysical Journal*, 201:740–748.

Yoshimura, H. (1976). Phase relation between the poloidal and toroidal solar-cycle general magnetic fields and location of the origin of the surface magnetic fields. *Solar Physics*, 50:3–23.

You, J. (2007). Photometric periods of LQ Hydrae between 1992 and 2000. *Astronomy & Astrophysics*, 475:309–315.

Zakhozhaj, V. A. and Shaparenko, E. F. (1996). The catalogue of nearby stars metallicities. *Kinematika i Fizika Nebesnykh Tel*, 12.

Zeeman, P. (1897). On the Influence of Magnetism on the Nature of the Light Emitted by a Substance. *The Astrophysical Journal*, 5:332.

Zeilik, M., de Blasi, C., Rhodes, M., and Budding, E. (1988). A half-century of starspot activity on SV Camelopardalis. *The Astrophysical Journal*, 332:293–298.